July 2022

Elucidating the Sources Supplying Aerosol Iron, Zinc, and Cadmium to the Surface of the North Pacific Ocean with Stable Isotopes

Zach B. Bunnell
University of South Florida

Elucidating the Sources Supplying Aerosol Iron, Zinc, and Cadmium to the Surface of the North Pacific Ocean with Stable Isotopes

by

Zach B. Bunnell

A thesis submitted in partial fulfillment
of the requirements for the degree of
Master of Science
College of Marine Science
University of South Florida

Major Professor: Tim M. Conway, Ph.D.
Matthias Sieber, Ph.D.
Robert. H. Byrne, Ph.D.
Clifton S. Buck, Ph.D.

Date of Approval:
June 28, 2022

Keywords: stable isotopes, aerosols, atmosphere, dust trace metals, GEOTRACES, North Pacific

TABLE OF CONTENTS

LIST OF TABLES

LIST OF FIGURES

ABSTRACT

Transition metals, such as iron (Fe), zinc (Zn) and cadmium (Cd), are found at just trace amounts within the global oceans yet are vital for many biological functions of phytoplankton. As a result, these metals influence the ocean's efficacy for carbon sequestration. Atmospheric dust is the primary input of Fe to various surface waters and may also supply Zn and Cd to oligotrophic surface waters. Here, I present Fe, Zn, and Cd isotope data from the US North Pacific GEOTRACES Section GP15 (Alaska-Tahiti) from the low-dust season (Sept. – Nov. 2018). Using this data and aerosol enrichment factors, I show that aerosol Fe, Zn, and Cd are sourced primarily from Asian dust for northern deployments (52 to 32°N), while for southern deployments (20°N to 20°S) they are sourced from a mixture of Asian dust and natural, wildfire, and anthropogenic aerosols from North America. An important finding of this study is that both GP15 data and Fe deposition modelling from the CAM6-QFED model confirms an isotopically heavy aerosol Fe source to the North Pacific (which spans the full range of particle sizes), which I attribute to soil being entrained during wildfires and possibly Fe sourced from shipping. Soluble aerosol Fe is light (-1.28 to +0.02‰) in both Northern and Southern deployments, strongly indicative of anthropogenic combustion Fe. A two-component isotope mixing model calculates that 0.5-7% of bulk aerosol and 12-81% of soluble aerosol Fe in the North are anthropogenic, but the model breaks down in the South because at least three sources contribute to Southern deployments. For Zn and Cd, the whole GP15 section is dominated by non-crustal sources, reflected by light isotopic compositions (bulk Zn: -0.29 to +0.01‰; soluble Zn: -0.35 to +0.09‰; soluble Cd: -1.91 to -0.07‰) and enrichment factors (Zn: 32-693; Cd: 263-10775). Northern deployments indicate the presence of a large proportion of highly soluble, anthropogenic Zn, while southern deployments are lighter and more enriched in Zn, attributed to wildfires. In contrast, Cd exhibited no latitudinal trends, indicating a consistent source of anthropogenic Cd throughout the year. Although there

is potential evidence of Fe and Cd aerosol influence on surface waters, the influence of Zn aerosols is not seen. Overall, this work highlights the utility of transition metal isotope tracers as powerful emerging tools for teasing apart distinct sources contributing to atmospheric aerosols, as well as the need to include additional sources such as wildfire and shipping with distinct isotopic signatures into models.

CHAPTER ONE:

INTRODUCTION

1.1 Trace Metals and Oceanic Primary Productivity

In the oceans, primary productivity has traditionally been thought to be governed by light, nutrient availability, and the stoichiometric ratio between the major nutrients, carbon, nitrate, and phosphate, known as the Redfield Ratio (Redfield, 1934). However, many transition metals such as iron (Fe), manganese (Mn), zinc (Zn), copper (Cu), cobalt (Co), and nickel (Ni) are also vital to cellular processes of photosynthetic organisms, acting as centers for many enzymatic reactions (Morel and Saito, 2014). Some transition metals, such as Cd and Cu, can also be toxic to phytoplankton at high concentrations (Brand *et al.*, 1986). These transition 'trace' metals exist in extremely low dissolved concentrations in seawater, ranging from pico- (pmol kg^{-1}) to nanomolar (nmol kg^{-1}), meaning that these micronutrients can act to limit growth (Morel *et al.*, 2003; Arrigo, 2005; Saito *et al.*, 2008). For example, dissolved Fe concentrations are found at levels that are 100 times deficient for photosynthesis in some surface waters (Moore *et al.*, 2013). In fact, the availability of Fe, as well as other metals, limits primary productivity over much of the surface oceans in two main ways: 1) in some areas low Fe concentrations cause primary productivity (chlorophyll-*a* concentrations) to be lower than expected and thus macronutrients such as nitrate and phosphate to be underutilized (Martin and Fitzwater 1988; Boyd *et al.*, 2007). These Fe-deficient areas are designated as high-nutrient, low-chlorophyll (HNLC) regions, and generally result from a depleted supply of upwelled dissolved Fe relative to nitrate and phosphate, or a lack of any significant external Fe source (Moore *et al.*, 2002). In oligotrophic surface waters limited by nitrate, dissolved Fe may stimulate primary production via nitrogen uptake by diazotrophs (Graziano *et al.*, 1996; Moore *et al.*, 2008; Moore *et al.*, 2013). Overall, Fe availability is thought to limit primary production over ~30% of the surface oceans (Moore *et al.*, 2013).

As such, the distributions of Fe and other trace metals in the ocean are key to controlling patterns of productivity, ecosystem composition, and CO_2 sequestration within the oceans.

Due to the extremely low concentrations of trace metals in the oceans, accurate measurements are challenging to obtain, especially given the potential for contamination during collection and sampling. The first accurate trace metal measurements were made in the 1970s (Boyle, 1976; Bruland *et al.*, 1979), yet measurements remained sparse until the late 2000s (Anderson *et al.*, 2014). However, pioneering progress in trace metal and organic ligand exploration during that time laid the groundwork for many present-day investigations (e.g., Boyle *et al.,* 1977; Bruland *et al.*, 1978; Landing and Bruland, 1987; Martin *et al.*, 1990; Sedwick *et al.*, 1997; de Baar *et al.*, 1995; de Baar *et al.*, 2005). Since 2010, the ongoing international 'GEOTRACES' program has revolutionized the field in terms of data availability and breadth (Mawji *et al.*, 2015; Schlitzer *et al.*, 2018; Schlitzer *et al.*, 2021). GEOTRACES is an international program comprised of scientists from over 30 countries undertaking global measurements of oceanic trace elements and their isotopes (TEIs; Anderson *et al.*, 2014). GEOTRACES' primary goal is to recognize and quantify fluxes and processes influencing the distributions of TEIs (Fig. A1; Jeandel *et al.*, 2006; Anderson *et al.*, 2014).

1.2 Marine Fe and Fe Isotope Cycling

Dissolved Fe (<0.2 μm) is an essential micronutrient required for a variety of biochemical processes within marine autotrophs, such as photosynthesis and nitrogen fixation by diazotrophs (Geider and La Roche, 1994; Moore *et al.*, 2001; Moore *et al.*, 2013). In surface waters, dissolved Fe uptake stimulates photosynthesis and phytoplankton growth, and Fe is returned to the dissolved phase at depth as organic matter sinks and decomposes (Geider and La Roche 1994; Morel and Price 2003). Scavenging and ligand complexation are additional components to the oceanic Fe cycle, in which dissolved Fe adsorbs to sinking particles and chelates with organic complexes, respectively (Rue and Bruland, 1995; Wu *et al.*, 2001; Boyd and Ellwood, 2010; Tagliabue *et al.*, 2017). Dissolved Fe is found at vanishingly-low concentrations in the oceans due to the low solubility of $Fe(III)(OH)_3(s)$, the dominant inorganic Fe species (Fe') in seawater at pH 8 (Byrne and Kester 1976; Hudson *et al.*, 1991; Millero *et al.*, 1995). Thus, most free Fe (Fe^{2+} or Fe^{3+})

in the ocean precipitates upon addition to seawater, with Fe only maintained above ~0.01-0.1 nmol kg^{-1} by complexation to organic ligands (Sunda, 1989; Hudson *et al.*, 1991; Millero *et al.*, 1995). As a result, >99% of the 'dissolved' Fe pool is thought to exist as ligand-bound Fe (Gledhill and van den Berg, 1994; Rue and Bruland, 1995; van den Berg, 1995; Wu and Luther, 1995).

Dissolved Fe concentrations vary from <0.05 to ~3 nmol kg^{-1} in the open ocean but can be found at 10 to 100+ nmol kg^{-1} near Fe sources (e.g., Martin *et al.*, 1989; Achterberg *et al.*, 2001; Von Damm *et al.*, 1985; Schlitzer *et al.*, 2018). The primary oceanic Fe sources are atmospheric deposition, hydrothermal venting, and reduction of Fe(III) in marine sediments (Boyd and Ellwood, 2010; Tagliabue *et al.*, 2014). While hydrothermal vents and marine sediments are considered 'natural' sources of Fe to the ocean, atmospheric dust can include both natural and 'anthropogenic' or human-derived Fe (Sedwick *et al.*, 2007; Sholkovitz *et al.*, 2009; Ito and Shi, 2016). Natural Fe aerosols are produced from the weathering of Fe-bearing minerals, while anthropogenic Fe is sourced through a variety of processes including biofuel combustion, biomass burning, and fossil fuel combustion (Sedwick *et al.*, 2007; Sholkovitz *et al.*, 2009; Ito and Shi, 2016). Hydrothermal vent fluids supply large quantities of dissolved Fe to the ocean, but most of it is removed near the vent through oxide and sulfide precipitation (German, 1991; Field and Sherrell, 2000). However, recent work has shown that a small amount of dissolved Fe can persist over large distances, possibly in the form of microparticle FeS and organic complexes (Toner *et al.*, 2009; Yucel *et al.*, 2011; Fitzsimmons *et al.*, 2014; Resing *et al.*, 2015; Conway and John 2014; Saito *et al.*, 2013; Klunder *et al.*, 2012). Marine sediments can supply Fe through two different pathways: reductive dissolution (RD) and non-reductive dissolution (NRD; Froelich *et al.*, 1979; Homoky *et al.*, 2013; Radic *et al.*, 2011; Jeandel *et al.*, 2011; Elrod *et al.*, 2004; Severmann et al., 2010). Dissolved Fe can be found at high concentrations near sediment sources, but concentrations decrease away from the source as dissolved Fe is quickly scavenged or lost to precipitation (Fitzsimmons *et al.*, 2014; Resing *et al.*, 2015; Conway and John 2014; Saito *et al.*, 2013; Klunder *et al.*, 2012). Due to rapid scavenging, Fe from hydrothermal vents and deep ocean sediments is generally less likely to reach the upper ocean than aerosol Fe, and thus, is less likely to affect oceanic productivity.

Dissolved Fe stable isotope ratios (δ^{56}Fe), expressed relative to the international IRMM-014 standard, have been used to further investigate Fe sources to as well as internal cycling within the global ocean (e.g., Severmann *et al.*, 2004; Radic *et al.*, 2011; John *et al.*, 2012; Homoky *et al.*, 2013; Conway and John, 2014; Ellwood *et al.*, 2015). Provided sufficient information about the isotopic endmembers of the sources is available and that the source signatures are not overprinted by fractionation associated with internal cycling processes, a two-component isotope mixing equation can be used to place constraints on the relative abundance of two Fe sources to a sample (e.g., Conway and John, 2014, Equation 1). In fact, each of the three natural sources of Fe to the oceans now have a reasonably-well constrained range of isotopic signatures (Fig. 1), making dissolved δ^{56}Fe measurements a potentially powerful parameter to calculate the relative importance of distinct Fe sources, specifically aerosols, to the ocean (Conway and John, 2014).

Eq. 1 $$\delta^{56}Fe_{sample} = (f_{Source\,1} * \delta^{56}Fe_{Source\,1}) + (f_{Source\,2} * \delta^{56}Fe_{Source\,2})$$

$$where: f_{Source\,1} + f_{Source\,2} = 1$$

The 'lithogenic' δ^{56}Fe signature of continental crust, ocean crust and marine sediments is +0.1‰. (Beard *et al.*, 2003; Poitrasson *et al.*, 2006). For aerosols, natural dust produced from the weathering and erosion of continental crust has a crustal composition of +0.1‰, while the source materials of anthropogenic Fe aerosols (combustion of fossil fuel, biomass, or biofuels) have been characterized with a δ^{56}Fe range of -4.7 to +0.8‰ (Waeles *et al.*, 2007; Kurisu *et al.*, 2012; Mead *et al.*, 2013; Kurisu *et al.*, 2016a; Conway *et al.*, 2019; Kurisu *et al.*, 2019). Iron isotope analyses have shown that marine aerosols collected *in situ* over the ocean can exhibit a light δ^{56}Fe signature, which may be used to determine the presence of, or constrain the relative contribution of, anthropogenic Fe in marine aerosols (Mead *et al.*, 2013; Kurisu *et al.*, 2016b; Conway *et al.*, 2019). Most recently, the presence of isotopically light dissolved δ^{56}Fe in surface North Pacific waters has been attributed to delivery of light anthropogenic aerosol Fe (Pinedo-González *et al.*, 2020). Dissolved Fe inputs from marine sediments are now thought to have two different δ^{56}Fe signatures

because of the two distinct dissolution pathways, RD and NRD (summarized by Homoky *et al.* 2021). The $\delta^{56}Fe$ endmember signature of dissolved Fe^{2+} in sedimentary porewaters by RD has been determined to be -3.3 to -0.3‰, due to a strong Fe(II)-Fe(III) redox control on Fe isotope fractionation (Berquist and Boyle, 2006; Severmann *et al.*, 2006; Homoky *et al.*, 2009; Severmann *et al.*, 2010; Homoky *et al.*, 2013; Klar *et al.*, 2017; Henkel *et al.*, 2018). This form of sedimentary. Fe release dominates only under low-oxygen conditions such as shallow continental margins (Homoky *et al.*, 2021). The more-recently proposed NRD (Radic *et al.*, 2011) is thought to consist of a release of 'colloidal' dissolved Fe(III) with a lithogenic $\delta^{56}Fe$ signature (+0.1‰) that dominates Fe release in the ocean interior (Homoky *et al.*, 2013; Homoky *et al.*, 2021). Biological uptake by phytoplankton and/or complexation with organic ligands have been suggested to drive heavy Fe signatures found within surface waters, but this remains poorly understood (Radic *et al.*, 2011; Conway and John, 2014; Ellwood *et al*., 2015; Ellwood *et al.*, 2020; Sieber *et al*., 2021).

The $\delta^{56}Fe$ signature of hydrothermal vent fluids ranges from -0.7 to -0.1‰ (Sharma et al., 2001; Beard *et al.*, 2003; Severmann *et al.*, 2004; Rouxel *et al.*, 2008; Bennett *et al.*, 2009; Rouxel *et al.*, 2016; Lough *et al.*, 2017; Nasemann *et al.*, 2018; Rouxel *et al.*, 2018). However, this primary hydrothermal isotopic signature may be altered through oxide and sulfide precipitation, microparticulate FeS transport, dissolved-particulate exchange, and organic complexation as the plume is transported away from the vent, leading to distal hydrothermal $\delta^{56}Fe$ signatures of -2.4 to +1.5‰ (Bennett *et al.*, 2008; Toner *et al.*, 2009; Yucel *et al.*, 2011; Sander and Koschinsky, 2011; Ellwood *et al.*, 2015; Lough *et al.*, 2017; Fitzsimmons *et al.*, 2017).

1.3 Marine Zn and Zn Isotope Cycling

Zinc is used by marine autotrophs as a cofactor in a variety of cellular mechanisms such as carbonic anhydrase formation and phosphate acquisition (e.g., Morel *et al.*, 1994). Dissolved Zn concentrations vary over several orders of magnitude in the ocean ranging from ~0.01 to 10 nmol kg^{-1} (Schlitzer *et al.*, 2018). Dissolved Zn exhibits a nutrient-like distribution within the water column where uptake causes depleted concentrations at the surface, and regeneration leads to elevated concentrations at depth (Bruland, 1980;

Martin *et al.*, 1989). Concentration profiles of dissolved Zn have been shown to exhibit a close correlation with dissolved silicate concentration profiles (Bruland *et al.*, 1978; Bruland, 1980) leading to a near-linear global Zn-Si correlation (Vance *et al.*, 2017), but the exact processes for the close association between the two elements are still under debate. Recently, a three-dimensional approach, combining biological uptake, regeneration, and scavenging (a one-dimensional view) with water mass mixing shows that biological uptake of Zn in the Southern Ocean, coupled with global circulation dynamics are likely the primary control on the distribution of Zn throughout the global oceans (Zhao *et al.,* 2014; Vance *et al.*, 2017, Weber *et al.*, 2018; Sieber *et al.*, 2020). In this 3D view, the global Zn-Si correlation arises from processes assigning pre-formed signatures to water masses in the Southern Ocean Hub (Vance *et al.*, 2017; Sieber *et al.* 2020), that are then advected around the global oceans, and is perhaps combined with reversible scavenging of Zn to organic matter (Weber *et al.*, 2018).

Atmospheric deposition, hydrothermal vents, sediments, and rivers are external sources of Zn to the ocean (Fig. 2; Conway and John, 2014; Little *et al.*, 2014; Lemaitre *et al.*, 2020), and carbonate sediments, euxinic organic-rich sediments, and Fe-Mn crusts act as oceanic sinks for dissolved Zn (Little *et al.*, 2016; Vance *et al.*, 2016). Crustal 'lithogenic' δ^{66}Zn is +0.20 to +0.34‰, relative to the international JMC-Lyon isotope standard (Fig. 2; Maréchal *et al.*, 2000; Archer and Vance, 2004; Chapman *et al*., 2006; John *et al.*, 2007; Little *et al.*, 2014). In the deep ocean, however, dissolved Zn is both isotopically homogenous and heavier than the crust, with a dissolved δ^{66}Zn signature of ~+0.5‰ (Bermin *et al.*, 2006; Andersen *et al.*, 2011; Boyle *et al.*, 2012; Conway *et al.*, 2013; Zhao *et al.*, 2014; Conway and John, 2014; Samanta *et al.*, 2017; John et al., 2018; Wang *et al.*, 2019). Set against this homogenous background, Zn sources and biogeochemical cycling mechanisms may impart distinctive isotopic signatures that may be used to trace these sources and processes within the water column.

Lighter dissolved δ^{66}Zn signatures can be observed in the deep ocean when waters are influenced by the input of dissolved Zn from sources such as marine sediments (e.g., Conway and John, 2014; John et al. 2018; Lemaitre *et al.*, 2020). While Zn supplied from hydrothermal vents has a δ^{66}Zn signature close +0.24‰ (Fig. 2; Conway and John, 2014; Lemaitre *et al.*, 2020), Zn released from sediments has a distinctly

light δ^{66}Zn range of -0.5 to -0.8‰ (Fig. 2; Conway and John 2014; Homoky *et al.*, 2013; Little *et al.*, 2014). Surface waters exhibit variable δ^{66}Zn signatures, from -1.0 to +1.0‰, and this has been attributed to competing processes of biological uptake, regeneration, and scavenging (Conway and John, 2014; John and Conway, 2014; Samanta *et al.*, 2018), with regeneration thought to release light Zn (Vance *et al.*, 2019). Most recently, deposition of aerosol Zn or release of sedimentary Zn has been invoked to explain light Zn in surface waters (Figure 3; Liao *et al.*, 2020; Lemaitre *et al.*, 2020), although surface sources need to be further constrained; aerosol Zn over the Atlantic Ocean has been observed to have a δ^{66}Zn composition of +0.1 to +0.5‰, while riverine Zn ranges from -0.1 to +1.0‰ (Fig. 2; Little *et al.*, 2014).

1.4 Marine Cd and Cd Isotope Cycling

In the ocean, dissolved Cd is found at concentrations from <1 pmol kg^{-1} to 1.1 nmol kg^{-1} (Bruland 1980; Schlitzer *et al.*, 2018). Perhaps surprisingly, since it is toxic for organisms at high concentrations, Cd is found within the cells of a variety of phytoplankton (Boyle *et al.*, 1976; Bruland *et al.*, 1978; Brand *et al.*, 1986; Sunda and Huntsman, 1996; Horner *et al.*, 2013). While a biological function for Cd in phytoplankton remains unclear, research has shown that Cd can substitute for Zn in carbonic anhydrase under certain conditions (Price and Morel, 1990; Lane and Morel, 2000). Other studies have suggested that Cd may be accidentally taken up into phytoplankton cells (Horner *et al.*, 2013). In either case, dissolved Cd concentrations exhibit a nutrient-like one-dimensional profile in the ocean, and a global correlation with phosphate (Bruland, 1983), although there is some complexity known as 'the kink' (de Baar *et al.*, 1994; Cullen *et al.*, 2006). Classically, the 'the kink' is where the slope of the Cd:PO_4 breaks and loses linearity. Like Zn, this pattern of dissolved Cd has traditionally been interpreted in a largely one-dimensional view. However, recent work has highlighted the role of biological and physical processes in the Southern Ocean, together with ocean circulation and mixing of water masses with different preformed Cd:PO_4 ratios, in setting the global distribution of Cd and its correlation with PO_4 in the oceans (Abouchami *et al.*, 2014; Middag *et al.*, 2018; Sieber *et al.*, 2019a; Sieber *et al.*, 2019b).

Dissolved Cd isotope ratios, denoted as δ^{114}Cd and expressed relative to the NIST SRM-3108 isotope standard, exhibit a homogenous isotope signature of +0.2 to +0.3‰ in all deep waters of the global oceans besides North Atlantic Deep Water (+0.4 to +0.5‰; e.g., Ripperger and Rehkämper, 2007; Ripperger *et al.*, 2007; Xue *et al.*, 2013; Abouchami *et al.*, 2014; Janssen *et al.*, 2014; Conway and John, 2015; Conway and John, 2015; John *et al.*, 2018; Sieber et al. 2019a). Like δ^{66}Zn, this deep ocean δ^{114}Cd signature is heavier than the lithogenic δ^{114}Cd signature, (-0.04‰; Fig. 3; e.g., Schmitt *et al.*, 2009; Abouchami *et al.*, 2013). Cadmium isotope values in the surface oceans are generally elevated (up to +2‰), due to the preferential uptake of light Cd by phytoplankton (Lacan *et al.*, 2006; Ripperger *et al.*, 2007; Wombacher *et al.*, 2008; Schmitt *et al.*, 2009). In contrast to dissolved δ^{66}Zn, δ^{114}Cd are less homogenous at intermediate depths throughout different basins, varying from +0.3 up to +0.5‰ (Bruland, 1980; Xue *et al.*, 2013; Yang *et al.*, 2014; Janssen *et al.*, 2014; Conway and John, 2015; Sieber 2019a). As with dissolved Cd concentrations, the three-dimensional view also postulates that Southern Ocean processes and subsequent ocean mixing causes the homogenous Cd isotope signatures found at depth, and the elevated and non-uniform Cd isotope values at intermediate depths (Xue *et al.*, 2013; Abouchami *et al.*, 2014; Sieber *et al.*, 2019a, b). Differences in intermediate waters Cd signatures are caused by preferential biological uptake of light Cd isotopes in the Southern Ocean that leave the water heavy are incorporated into Subantarctic Mode Water (SAMW) and Antarctic Intermediate Water (AAIW) and are subsequently advected to lower latitudes (Abouchami *et al.*, 2014; Sieber *et al.*, 2019b). Cd aerosol concentrations are much lower than the intermediate and deep-water sources supplying surface waters, as such, Cd aerosol deposition typically has little influence on isotopic signature of surface waters.

Cd is sourced naturally to the ocean by rivers and atmospheric aerosols (Morel and Malcolm, 2004), and is removed from the ocean when it is buried beneath the sediment-water interface in porewaters with low oxygen and sulfidic conditions (Rosenthal *et al.*, 1995; Van Geen *et al.*, 1995). Cadmium may also be removed from the water column during sulfide precipitation when sinking organic matter respires in oxygen minimum zones though this has remained controversial (Al-Farawati and van den Berg, 1999; Janssen et al., 2014). The role of hydrothermal systems in the Cd cycle remains poorly constrained, but they may also

act as a sink (Janssen *et al.*, 2014; Conway *et al.*, 2015). Natural input fluxes of Cd to the ocean from rivers and aerosols have been found to be similar in magnitude but are not very well constrained (Morel and Malcolm, 2004). Anthropogenic sources such as Pb-Zn ore smelting, Zn mining, waste incineration, and coal combustion, produce Cd aerosols that may also supply Cd to the surface of the ocean (Nriagu and Pacyna, 1988; Pacyna and Pacyna, 2001; Pacyna *et al.*, 2009; Cheng *et al.*, 2014; Bridgestock *et al.*, 2017). While naturally sourced Cd aerosols have an isotopic range from -0.08‰ to +0.05‰, anthropogenic Cd aerosols occupy a range of -1.6‰ to +0.8‰ (Fig. 3; Schmitt et al., 2009; Rehkämper et al., 2012; Bridgestock *et al.*, 2017). On a first approximation, the long residence time of Cd in seawater (Hayes *et al.*, 2019) and the relatively small input of Cd from sources means that, in contrast to δ^{56}Fe or δ^{66}Zn, Cd addition is unlikely to strongly influence dissolved δ^{114}Cd profiles. However, Cd concentrations are lowest in surface waters (<1 pmol kg^{-1}), so Cd addition by aerosols could influence surface δ^{114}Cd in some areas such as oligotrophic gyres. Further, aerosol δ^{114}Cd is significantly lighter than surface water dissolved δ^{114}Cd compositions, and thus could prove valuable for tracking Cd aerosol contributions to surface waters (George *et al.*, 2019). In fact, this addition of Cd from dust and aerosols has been invoked to explain light surface Cd compositions in both the North and South Pacific (George *et al.*, 2019; Sieber, in review).

1.5 Tracing Anthropogenic and Lithogenic Trace Metals in Aerosols

Anthropogenic trace metal aerosols were initially thought to be an insignificant source of nutrients for oceanic primary productivity compared to their natural counterpart, but recent work has shown they can be an important source of Fe and other trace metals to the ocean (e.g., Sedwick *et al.*, 2007; Sholkovitz *et al.*, 2009; Ito and Shi, 2016; Conway *et al.*, 2019). Anthropogenically-sourced trace metals were first identified in aerosol samples by using enrichment factors or aerosol solubilities (e.g., Sedwick *et al.*, 2007; Sholkovitz *et al.*, 2009; Shelley *et al.*, 2015; Buck *et al.*, 2019). Enrichment factors (EF) compare the ratio of a trace metal (TM) to a naturally-sourced element such as aluminum (Al) or titanium (Ti; Marsay *et al.*, 2021) in an aerosol sample to the TM:Al or (TM:Ti) ratio of Upper Continental Crust (UCC) to determine if a trace metal is influenced by an anthropogenic component (Equation 2). An EF greater than one signifies

that the sample contains anthropogenic trace metals (e.g., Shelley *et al.*, 2015). The natural endmember of elements like Fe, Mn, Nd, and Sn typically overwhelms the bulk phase and so these elements on average have EFs near 1 while elements such as Cd, Co, Ni, Pb, V, and Zn are more susceptible to anthropogenic influence and often display much larger EFs.

Eq. 2
$$EF = \left[\frac{\left(TM/Al\right)_{Sample}}{\left(TM/Al\right)_{UCC}}\right]$$

Trace metal 'solubility' in aerosols is operationally defined, usually as the ratio between the 'soluble' or dissolvable trace metals from an aerosol sample and the trace metals in a "bulk" aerosol sample (Equation 3). 'Bulk' samples represent the total mass of trace metals in each aerosol sample following total digestion with HF and HNO_3, while 'soluble' trace metals are obtained following one of a number of leaching procedures designed to simulate aerosol deposition and solubilization.

Eq. 3
$$Solubility = \left(\frac{TM_{soluble}}{TM_{bulk}}\right) \times 100$$

Natural desert dust contains relatively insoluble Fe oxyhydroxides, while Fe from anthropogenic aerosols is much more soluble (e.g., Guieu *et al.*, 2005; Chuang *et al.*, 2005; Sedwick *et al.*, 2007; Luo *et al.*, 2008; Sholkovitz *et al.*, 2009; Ito and Shi, 2016). As such, it has been suggested that the presence of anthropogenic aerosol Fe may be shown by solubility measurements (e.g., Sedwick *et al.*, 2005). For example, solubility measurements on dust collected in Bermuda showed that solubility was low (~1%) during the Saharan summer dust season but increased up to 16% during the winter (Sedwick *et al.*, 2007; Sholkovitz *et al.*, 2012). These high Fe solubilities during winter were attributed to the influence of fossil fuel combustion from the east coast of North America during the low Saharan dust season (Sedwick *et al.*, 2007; Sholkovitz *et al.*, 2012). In this way, dust arriving from Bermuda can be thought of as a two-

component binary mixing of high-loading low-solubility Saharan dust, and low-loading high-solubility anthropogenic aerosols (Sedwick *et al.*, 2005; Sedwick *et al.*, 2007; Sholkovitz *et al.*, 2012).

Another tool to assess aerosol sources are HYSPLIT model back trajectories; these are provided by the National Oceanic and Atmospheric Administration (NOAA) to backtrack the transport of air masses at various altitudes to a location over a set time interval (https://www.ready.noaa.gov/HYSPLIT.php). By generating back trajectories of air masses based on latitude, longitude, and time of sample collection, HYSPLIT models have been used previously to establish where air masses carrying TM aerosols originated to assess if a sample has been influenced by anthropogenic inputs (e.g., Buck *et al.*, 2006; Shelley *et al.*, 2015; Marsay *et al.*, 2021).

However, while back-trajectories, EF, and solubility have all proven useful in highlighting the importance of anthropogenic components of aerosols, these approaches have limitations. For example, enrichment factors are less suited for tracing anthropogenic Fe when most of the bulk phase is natural dust (e.g., Chester *et al.*, 1993; Shelley *et al.*, 2015). Additionally, the presence of high EFs for anthropogenic elements such as Pb, V, or Ni does not provide direct information about the co-presence or amount of anthropogenic Fe. For solubility, factors other than the presence of anthropogenically sourced metals can be influential (Glaccum and Prospero, 1980; Baker and Jickells, 2006; Sedwick *et al.*, 2007; Journet *et al.*, 2008; Buck 2010; Trapp *et al.*, 2010). For example, aerosol Fe solubility can significantly vary as aerosols are transported from their source (Trapp *et al.*, 2010, Jickells *et al.*, 2016), likely related to differences in mineralogy, grain size, or loading (Baker and Jickells, 2006; Journet *et al.*, 2008; Trapp *et al.*, 2010; Conway *et al.*, 2015). Additionally, cloud-particle interactions due to pH changes, deposition type (wet or dry), photochemistry, and organic complexation have also been suggested to affect solubility (Duce and Tindale, 1991; Duce *et al.*, 1991; Jickells and Spokes, 2001; Ussher *et al.*, 2004; Jickells *et al.*, 2005; Mahowald *et al.*, 2008; Baker and Croot, 2010; Breitbarth *et al.*, 2010). Lastly, high solubilities (~40%) have been measured in last glacial maximum (LGM) aerosols, showing that high Fe 'solubility' is not always indicative of anthropogenic Fe (Conway *et al.*, 2015).

As described in Section 1.2, recent work has shown that stable isotopes can be a useful tool to distinguish natural and anthropogenic Fe contributions in atmospheric aerosols. Distinct isotopic end members have been used to fingerprint the relative contributions of natural dust and anthropogenically-sourced North Atlantic aerosols using a simple two-component mixing model shown in Equation 1 (e.g., Conway *et al.*, 2019). The fractions $f_{Source\ 1}$ and $f_{Source\ 2}$ can be solved for in Equation 1 by assigning isotopic endmembers for natural and anthropogenic trace metal aerosols ($\delta^{56}Fe_{Source\ 1}$ as natural and $\delta^{56}Fe_{Source\ 2}$ as anthropogenic, respectively) and measuring the $\delta^{56}Fe$ composition of a sample. While natural Saharan dust has a well-established $\delta^{56}Fe$ crustal signature (+0.1‰), the $\delta^{56}Fe$ signature of anthropogenic aerosols has only been constrained recently (Beard *et al.*, 2003; Waeles *et al.*, 2007; Conway *et al.*, 2019). Initial measurements showed that combustion products likely carry slightly heavy isotopic signatures, seemingly excluding anthropogenic processes as the source of light Fe in aerosols (Mead *et al.*, 2013). However, further research by Kurisu *et al.* (2016a, b) showed that products of fossil fuel combustion can have $\delta^{56}Fe$ signatures ranging from -3 to +0.3‰, with the $\delta^{56}Fe$ signature of the aerosols dependent on the size of the emitted particles; large particles (>1.1 μm) exhibited isotope values from 0 to +0.3‰ and small particles (<1.1 μm) had values between -3 and 0‰. Kurisu *et al.* (2016a) hypothesized that the overwhelming abundance of coarse particles near sources causes the overall $\delta^{56}Fe$ signatures of combustion aerosols to be equivalent to the $\delta^{56}Fe$ of gasoline (+0.3‰). However, many large combustion particles likely fall near their source, and thus, do not contribute to the Fe load deposited to the open oceans as much as their smaller counterparts. The smaller particles that persist further are isotopically lighter, leading to a distal light $\delta^{56}Fe$ signature for combustion aerosols over the open ocean (as observed by Conway *et al.*, 2019). Consistent with this idea, and based on observations in the North Atlantic, Conway *et al.* (2019) carried out source apportionment using a $\delta^{56}Fe$ endmember of -1.6‰ for anthropogenic aerosol Fe and an endmember of +0.1‰ for natural dust aerosol.

Like Fe, aerosol Zn and Cd can be sourced naturally in the form of lithogenic dust or from anthropogenic processes such as fossil fuel combustion and biomass burning, with EFs as a useful indicator of their presence (Chester *et al.*, 1993; Shelley *et al.*, 2015). Natural and anthropogenic Zn and Cd aerosols

may also have distinct isotope signatures, although Cd and Zn aerosol isotopic signatures remain poorly constrained. Potential anthropogenic Zn aerosol sources such as steel production, mining, and vehicle exhaust have signatures of -1.1 to -0.1‰ (Gioia *et al.*, 2008). Marine Zn aerosols influenced by Saharan dust from the North Atlantic have a δ^{66}Zn signature of +0.2 to +0.5‰ (Little *et al.*, 2014). Gioia *et al.* (2008) found urban aerosols collected near industrial hotspots in Brazil had a δ^{66}Zn range of -1.1 to -0.1‰. For Cd, although anthropogenic aerosols have been estimated to account for ~85% of the total Cd aerosol deposition to the oceans (Morel and Malcolm, 2004), knowledge of aerosol Cd isotopic signatures remains limited to a single study (Bridgestock *et al.*, 2017). However, this study does point to the utility of this parameter – with natural Cd produced from volcanoes, lithogenic dust, and rivers having a δ^{114}Cd signature of -0.08 to +0.05‰, and anthropogenic sources of aerosol Cd with a lighter δ^{114}Cd signature of -1.6 to -0.1‰ (Bridgestock *et al.*, 2017). Thus, both δ^{66}Zn and δ^{114}Cd may be useful tracers for anthropogenic aerosols given more data.

1.6 Global Dust Deposition Models and Modelling Aerosol Iron Isotopes

Numerous global dust deposition models, forced by observations, have been developed to forecast and hindcast atmospheric Fe deposition to the oceans (e.g., Fung *et al.*, 2000; Hand *et al.*, 2004; Moore *et al.*, 2004; Parekh *et al.*, 2004; Luo *et al.*, 2005; Jickells *et al.*, 2005; Luo *et al.*, 2008; Mahowald *et al.*, 2008; Tagliabue *et al.*, 2009; Okin *et al.*, 2011; Hamilton *et al.*, 2019). However, to constrain outputs, these models require knowledge of the form, solubility, and magnitude of natural and anthropogenic dust sources, as well as atmospheric processes to constrain outputs. Recently, the isotopic composition of aerosol Fe was used together with dust deposition modeling to refine source and process parametrization in dust models; Conway *et al.* (2019) compared δ^{56}Fe data from GEOTRACES aerosols in the North Atlantic and output from the Community Atmosphere Model (CAM4; Scanza *et al.*, 2018). The isotope-informed comparison showed that refinements of the CAM4 model simulation were needed to reproduce the North Atlantic observations, namely reduction of dust source solubilization and an overall increase in anthropogenic Fe source emissions by 5x. This example highlights the utility of Fe isotopes as a direct tracer for

anthropogenic Fe, but also for better parameterizing model outputs. Most recently, Kurisu *et al.* (2021) carried out a similar data-model informed exercise in the North Pacific using the IMPACT model.

1.7 North Pacific Setting and Atmospheric Circulation

Deposition fluxes of Fe in the North Pacific Ocean have been previously calculated and estimated from field observations and global deposition models attempting to constrain global Fe fluxes to the surface ocean from dust (e.g., Ginoux *et al.*, 2001; Zender *et al.*, 2003; Jickells *et al.*, 2005; Buck *et al.*, 2006; Buck *et al.*, 2013; Matsui *et al.*, 2018; Conway *et al.*, 2019; Ito *et al.*, 2019). Dust supplied to the Eastern North Pacific Ocean can be simplified as a combination of Asian and Alaskan dust. Natural Asian dust Fe originates primarily from the Chinese Loess Plateau, and anthropogenic Asian Fe aerosols result from anthropogenic processes occurring in countries on the eastern flank of Asia (Buck *et al.*, 2006; Buck *et al.*, 2013; Kurisu *et al.*, 2016a: Kurisu *et al.*, 2016b). Alaskan Dust is primarily composed of natural ferric oxides and glacial flour sourced from the Alaska Range and may be influenced by down-wind anthropogenic processes such as fossil fuel and biomass combustion (Schroth *et al.*, 2009: Crusius *et al.*, 2011). Over the North Pacific, air masses come from the western coast of Asia and travel eastward across the North Pacific before contacting North America (Fig. 4; Martin *et al.*, 2002). Two major features exist in the atmospheric circulation (Asian Outflow) of the North Pacific Ocean (Fig. 4). The first major feature of the Asian Outflow air masses originates at ~40^{o}N on the eastern coast of Asia and moves eastward across the North Pacific Ocean and across North America. The other carries air masses from East Asia (~15^{o}N) northeast to ~35^{o}N before traveling south along the west coast of North America. The air masses are then deflected at the equator and travel southwest (Martin et al., 2002). Additionally, there are two minor air mass features: 1) runs along the coast of Baja California and is deflected west at the equator and 2) originates in northwestern South America and travels west (Martin *et al.*, 2002; Fig. 4).

Prior work on North Pacific aerosols shows dust deposition to surface waters is highly variable throughout the year with peak dust fluxes from March to May when climatic conditions favor dust events, and considerably lower the rest of the year (June to February) as indicated by field observations and aerosol

optical depth (AOD) imagery from MODIS (Fig 5; Parrington *et al.*, 1983; Buck *et al.*, 2006; Fischer *et al.*, 2009; Buck *et al.*, 2013; Pinedo-Gonzalez *et al.*, 2020). Model results often disagree with each other during attempts to constrain total dust fluxes to the oceans, especially in the North Pacific where model estimations range from 8 Tg yr^{-1} to 28 Tg yr^{-1} due to the spatial and seasonal variability of dust fluxes (Ginoux *et al.*, 2001; Zender *et al.*, 2003; Jickells *et al.*, 2005). In addition to modelled uncertainty of total Fe deposition, the large range of Fe solubility observed in aerosols in the North Pacific (<1% to >50%) compounds Fe flux uncertainty, meaning that models struggle to produce agreeable outcomes of the amount of soluble Fe supplied to North Pacific surface waters when compared to observations (Buck *et al.,* 2006; Buck *et al.*, 2013).

The presence of anthropogenically derived Fe in aerosols presents another mode of uncertainty in global climate models simulating dust fluxes. Recent studies have aimed to constrain the presence of anthropogenic Fe (e.g., Ito *et al.*, 2013; Matsui *et al.*, 2018; Ito, 2019; Conway *et al.*, 2019; Pinedo-Gonzalez *et al.*, 2020; Rathod *et al.*, 2020) and have led to an increase in the modeled amount of soluble Fe deposition to the surface oceans. Conway *et al.* (2019) informed the global CAM4 Fe deposition model with $\delta^{56}Fe$ data from aerosols collected over the North Atlantic Ocean and estimated that more than 40% of the Fe supplied to the surface of the North Pacific Ocean is anthropogenically derived compared to the ~0-10% abundance the base simulation exhibited (Fig. 6; Conway *et al.*, 2019). Additionally, the overall amount of soluble anthropogenic Fe deposition increased from ~0-150 μg m^{-2} yr^{-1} to 500 μg m^{-2} yr^{-1} to various regions of the North Pacific (Conway *et al.*, 2019). However, the model results from Conway *et al.* (2019) are forced only with isotope observations from North Atlantic aerosols, and so, data are needed from other regions to test both this approach and their findings. Recently, Kurisu et al. (2021) measured $\delta^{56}Fe$ in size-fractionated (coarse: >2.5 μm; fine: <2.5 μm) open ocean North Pacific aerosols and found that the coarse particles were dominantly natural Fe ($\delta^{56}Fe$ ranging from 0.0 to +0.4‰), and fine particles were all isotopically light ($\delta^{56}Fe$ -2.2 to -0.5‰). By correlating the light $\delta^{56}Fe$ with elevated V and Pb EFs, they showed the light Fe found in fine fraction samples was due to the presence of combustion Fe (Kurisu *et al.*, 2021). Additionally, by pairing North Pacific size-fractionated aerosol contributions and $\delta^{56}Fe$ data with

predicted aerosol δ^{56}Fe output from the IMPACT atmospheric transport model. Kurisu *et al.* (2021) recently found δ^{56}Fe values measured in aerosol particles in agreement with model δ^{56}Fe output (informed by size-fractionated data) for fine particles near East Asia; however, the model had trouble producing coarse (>2.5 μm) combustion aerosol δ^{56}Fe over the open ocean (Kurisu *et al.*, 2021).

1.8 Thesis Overview

In this thesis, I present concentration and isotope data of bulk and soluble Fe, Zn, and Cd in atmospheric aerosols, as well as Fe concentrations and isotopic compositions in size-fractionated atmospheric aerosols collected during the US GEOTRACES Pacific Meridional Transect (GP15) from Alaska-Tahiti in the North Pacific. First, I compare these data with other aerosol parameters such as EFs in order to assess the source (and variability in source and composition) of North Pacific aerosols. Using literature constrained endmembers, a two-component model is then attempted to calculate the proportionality of natural and anthropogenic Fe. Second, binned size-fractionated aerosol Fe concentrations and δ^{56}Fe, in conjunction with bulk aerosol δ^{56}Fe, are used to assess how the δ^{56}Fe of aerosols changes between size classes and to provide further insight into aerosol Fe sources. Then, by combining GP15 size-fractionated aerosol δ^{56}Fe data with published data in the region, I investigate the variability in Fe sources to the whole North Pacific. Third, GP15 bulk and soluble Fe concentrations and δ^{56}Fe are compared to atmospheric deposition modelling (QFED output from the CAM6 model) to assess if the model is capturing Fe deposition during the low dust season of the North Pacific, and to test ideas about different atmospheric Fe sources to the GP15 section. Last, soluble aerosol signatures are compared with GP15 surface water concentrations and isotope compositions to evaluate if Fe, Zn, or Cd aerosols impart their signature in the surface ocean in this region during the low-dust season.

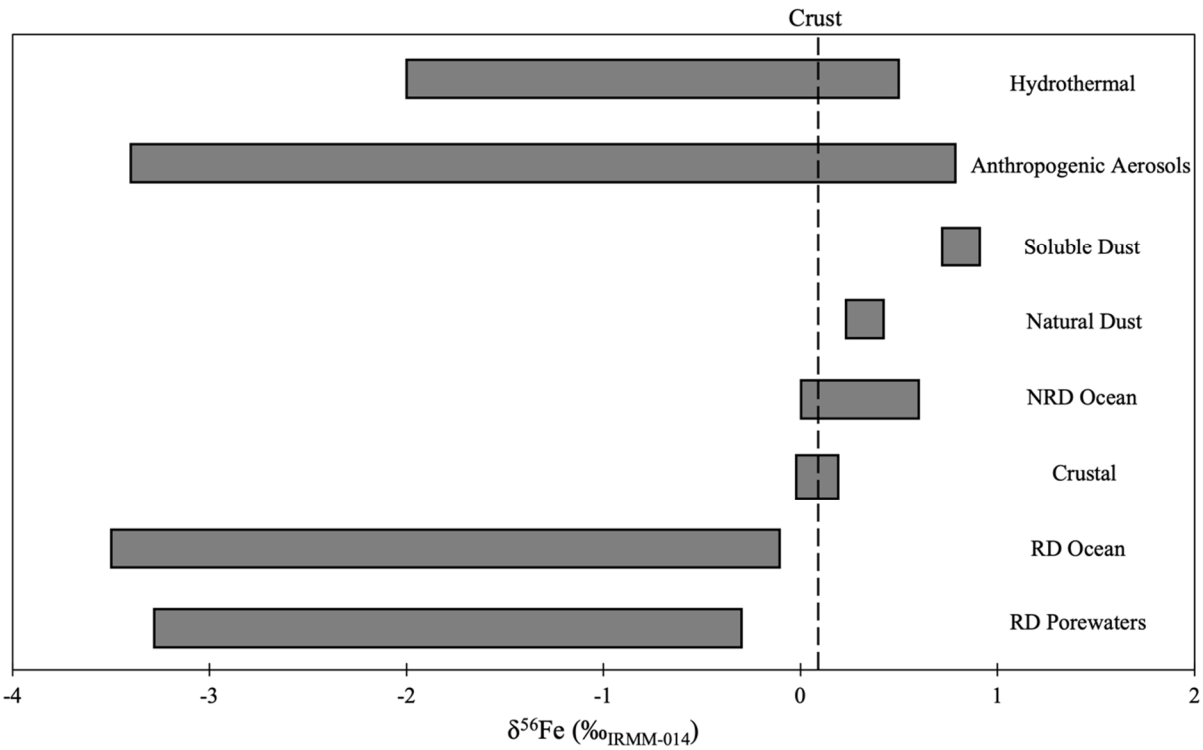

Figure 1. Fe Isotopic Signatures of Potential Oceanic Sources. The crust has an average δ^{56}Fe signature of +0.09 (range: -0.01 to +0.19‰), and its mean is represented by the dashed line. Data from Beard *et al.* (2003); Poitrasson *et al.* (2006); Severmann et al. (2010); Radic et al. (2011); John and Adkins (2012); Homoky *et al.* (2013); Staubwasser *et al.* (2013); Conway and John (2014); Ellwood *et al.* (2015); Chever *et al.* (2014); Labutut *et al.* (2014); Mead *et al.* (2013); Fitzsimmons *et al.* (2016); Klar *et al.* (2017); Klar *et al.* (2018); Homoky *et al.* (2021).

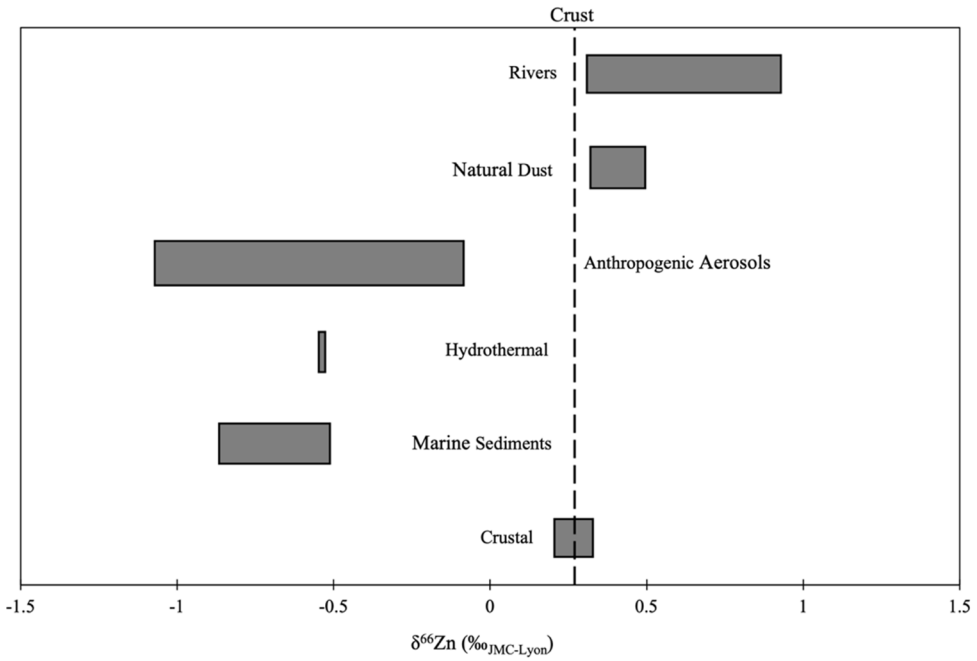

Figure 2. Zn Isotopic Signatures of Potential Oceanic Sources. The crust has an average δ^{66}Zn signature of +0.27 (range: +0.20 to +0.34‰), and its mean is represented by the dashed lines. Data sourced from Maréchal *et al.* (2000); Archer and Vance (2004); Chapman *et al*. (2006); Bermin *et al.* (2006); John *et al.* (2007); Andersen *et al.*, (2011); Boyle *et al.* (2012); Homoky *et al.* (2013); Conway *et al.* (2013); Zhao *et al.* (2014); Conway and John, (2014); Little *et al.* (2014); Samanta *et al.* (2017); John *et al.* (2018); Wang *et al.* (2019) ; Lemaitre *et al.* (2020).

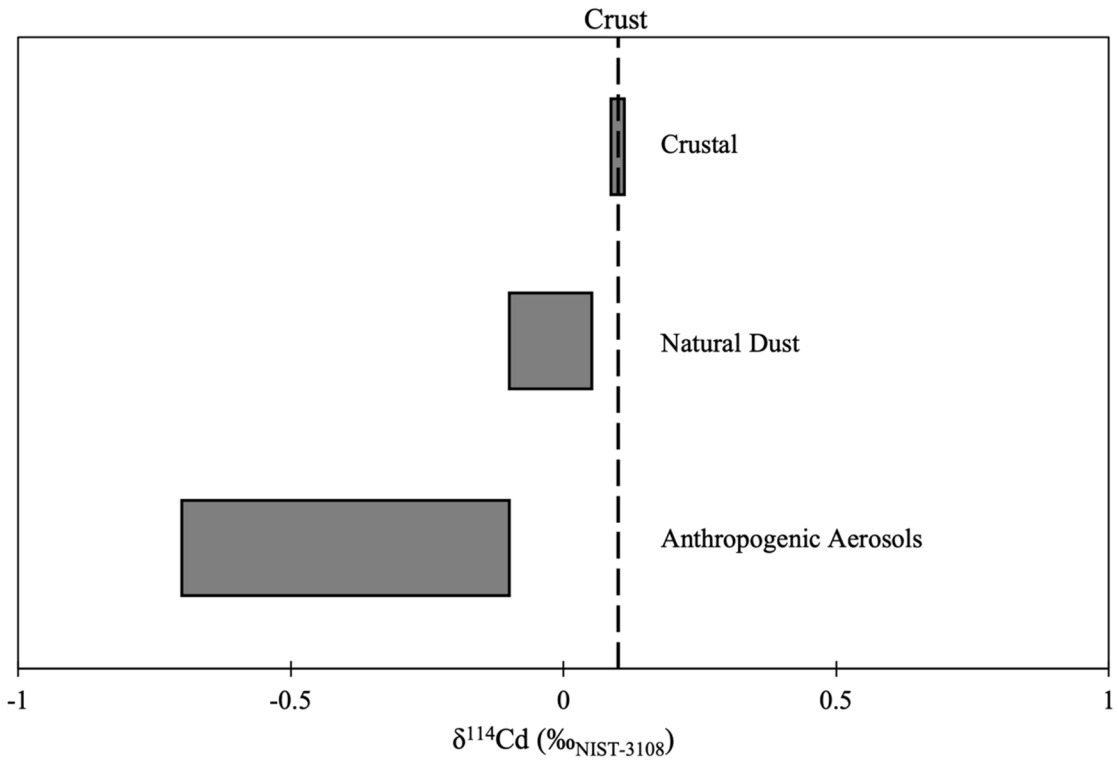

Figure 3. Cd Isotopic Signatures of Potential Oceanic Sources. The crust has a δ^{114}Cd signature of -0.04‰ and is represented by the dashed line. Data sourced from Abouchami *et al.* (2014); Bridgestock *et al.* (2017); George *et al.* (2019).

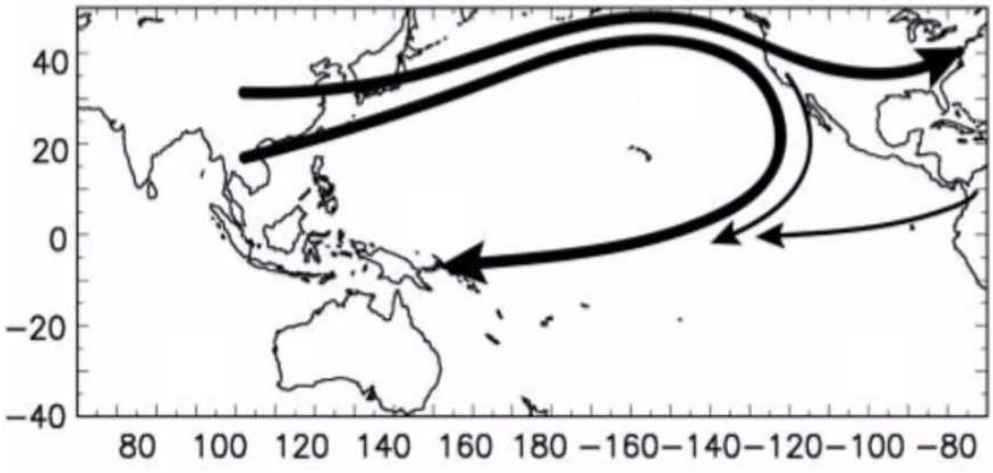

Figure 4. Generalized North Pacific Atmospheric Circulation (reproduced from Martin *et al.*, 2002)

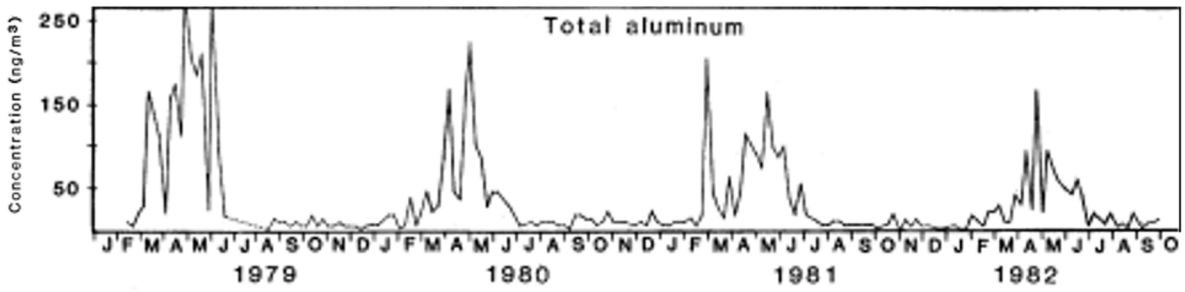

Figure 5. North Pacific Dust Seasonality. Seasonal trends based on total aerosol Al (modified from Parrington *et al.*, 1983).

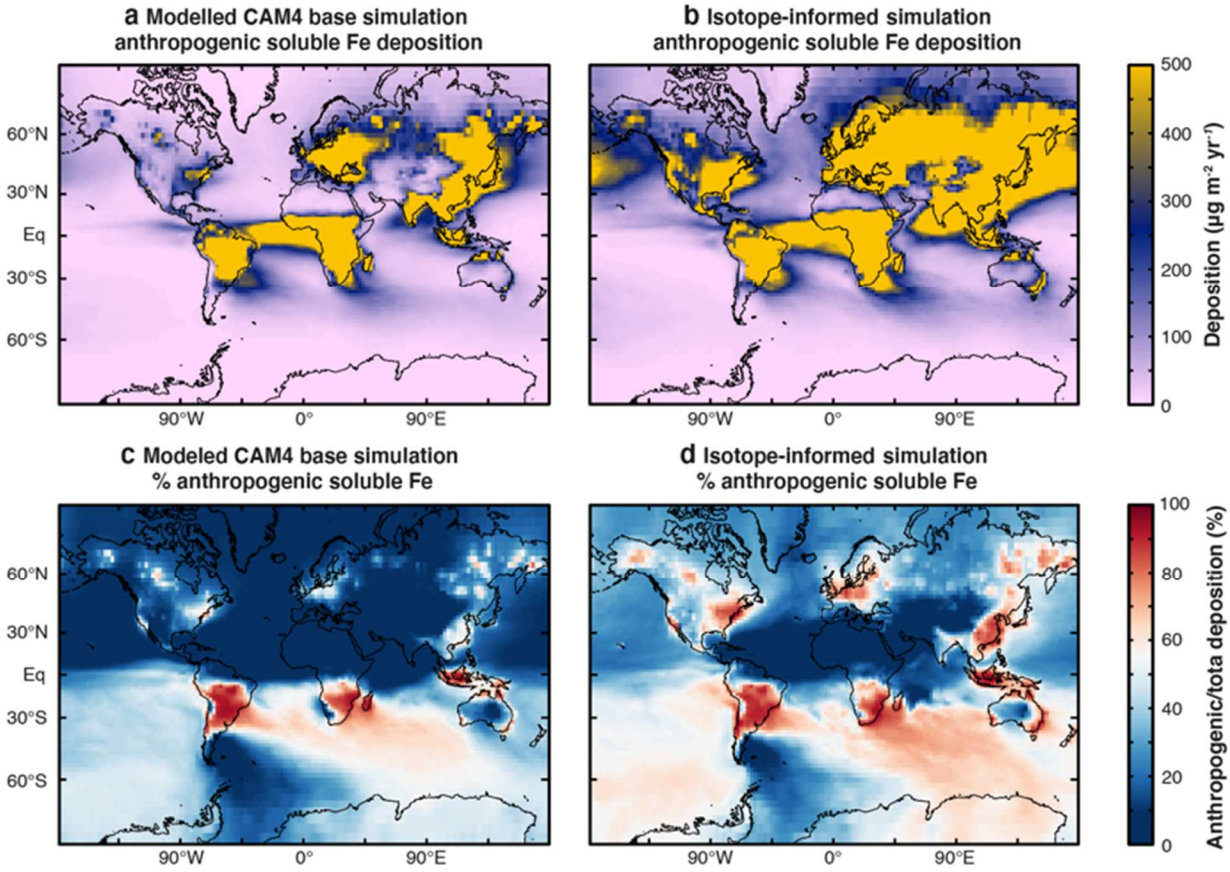

Figure 6. Dust Deposition Model Output from Conway *et al.* (2019). Model Comparison Original CAM4 base simulation of **A)** soluble Fe deposition and **C)** % anthropogenic soluble Fe compared to isotope informed CAM4 simulation of **B)** soluble Fe deposition and **D)** % anthropogenic soluble Fe. Isotope informed simulation was performed by increasing anthropogenic Fe emissions by five times and decreasing dust solubility from 25 to 10%. (reproduced from Conway *et al*. 2019).

CHAPTER TWO:

METHODS

2.1 Sample Overview

A total of 23 bulk aerosol filter and 12 size-fractionated aerosol filter deployments were collected by collaborators from the University of Georgia (UGA) onboard the R/V *Roger Revelle* as part of the US GEOTRACES GP15 section cruise from Alaska to Tahiti (Fig. 7; September to November 2018; Marsay *et al.*, 2022). Aerosol filters were leached onboard or digested back on shore at UGA by collaborators (Marsay and Buck) to provide 'soluble' or 'total' samples for this project. Here, 'soluble' samples denote the soluble fraction or dissolvable amount of trace metals from a given aerosol upon instantaneous leaching of an aerosol-laden filter with ultrapure water (UPW) and filtration through a 0.2 μm backing filter (Buck *et al.*, 2006). Total aerosol samples, also referred to as 'bulk' samples, denote the total amount of trace metals collected, obtained following digestion of the aerosol-laden filter with HF-HNO_3 (Marsay et al., 2022). A detailed overview of the sample collection procedure is provided in Section 2.2.

Following processing, samples from 12 deployments were made available for this project (one UPW and two bulk digest samples per deployment), and two bulk and two soluble 'blank' samples were provided for blank correction (with clean and undeployed filters processed through the methods below). Bulk samples were measured at USF for total Fe and Zn concentrations and isotope ratios and Cd concentrations to complement total Fe and Zn concentrations measured on separate bulk filter digests at UGA. UPW leaches were measured for soluble Fe, Zn, and Cd concentrations and isotope ratios at USF. Size-fractionated (based on particle size cut-off) bulk digests (80) were also supplied for total Fe concentration and isotopic analysis (12 size-fractionated deployments with six filter stages each, five stage filter blanks, and three backing filter blanks).

2.2 Shipboard Sample Collection and Primary Processing (Buck and Marsay, UGA*)*

Aerosol samples were collected by collaborators during GEOTRACES GP15 aboard R/V Roger Revelle (September 15th – November 25th, 2018) onto filters using five Tisch Environmental high-volume samplers, following published methods (Marsay *et al.*, 2022). A Campbell Scientific CR800 data-logger, anemometer, and wind vane was used to maintain constrained sampling conditions (Marsay *et al.*, 2022); the samplers only collected samples when there was a relative wind speed of >0.5-1 ms^{-1} and direction of ± 60^{o} with respect to the bow of the ship sustained for at least five minutes. To avoid contamination from sea spray and ship exhaust, the samplers were deployed above the ship deck and forward of the smokestack at the bow. Aerosols were collected onto 12 acid-cleaned 47-mm diameter Whatman 41 ashless cellulose filters inserted in the sampler during each deployment (Marsay *et al.*, 2022). Clean and undeployed Whatman 41 ashless cellulose filters were either digested or leached to provide bulk and soluble blanks, respectively. Soluble, bulk, and size-fractionated aerosol samples for this work were then further processed under clean conditions using one of three chemical procedures prior to analysis.

1) Soluble metals. Aerosol-laden filters were leached shipboard to collect leachate samples for 'soluble' trace metals following Buck *et al.*, (2006; 2010; 2013) using ultrapure water (Procedure 1). The leachate samples (soluble) were collected "instantaneously" by placing a 47 mm diameter Whatman 41 ashless cellulose filter containing aerosols on a Nalgene polysulfone filter holder attached to a vacuum pump and passing 100 mL of UHP water through the filter in approximately 10 seconds. Following collection, double distilled conc. HNO_3 was added to acidify the solution to approximately 0.024 M HNO_3, and samples were stored for at least a year prior to analysis.

2) Total metals. Back on shore, aerosol-laden 47-mm diameter Whatman-41 cellulose fiber filters were digested at UGA to provide bulk 'total' samples (Procedure 2) with three heating and dry-down steps. Heating of solutions was carried out overnight while evaporations occurred the following day. First, a filter is transferred to a 15 mL PFA beaker and heated at 140^{o}C in 1 mL of double distilled concentrated HNO_3 (Buck *et al.*, 2013; Marsay *et al.*, 2021). Next, the resulting filter 'residue' was digested overnight in 500 µL of double distilled concentrated HNO_3, 100 µL concentrated HF, and 100 µL of concentrated H_2O_2 at

140ºC. Lastly, the solution was digested in 500 µL of double distilled concentrated HNO_3 allowed to dry-down on a hotplate (Buck *et al.*, 2013; Marsay *et al.*, 2021). Digest samples were then redissolved in 1 mL of double distilled HNO_3.

3) Size-fractionated total metals. Size-fractionated aerosol samples were collected on five Whatman 41 cellulose ester stage filters and one Whatman 41 cellulose fiber backing filter during 12 deployments using a Tisch Environmental, Inc High Volume Cascade Multi-Stage Particulate Size Fractionator Impactor (Series 230) set to collect 1.2 m^3 air per minute (Tisch Environmental, Inc, 2004; Gurganus *et al.*, 2015). The impactors collect the size-fractionated aerosols onto one of five stage filters or backing filter. Exact size partitioning of each size filter requires additional analytical techniques outside the scope of this work, but the size cut offs for each stage can be estimated as: stage one (>7.2 µm), stage two (3.0-7.2 µm), stage three (1.5-3.0 µm), stage four (0.95-1.5 µm), stage five (0.49-0.95 µm), and backing filter (<0.49 µm) (Tisch Environmental, Inc, 2004; Gurganus *et al.*, 2015). Stage and backing filters were portioned into nine (stage 1) or ten (stages 2-5 and backing filter) strips and were processed in the same manner as bulk aerosol digests (Procedure 2). Briefly, two stage filter strips (one for backing filter) were digested in a series of HNO_3, HF-HNO_3-H_2O_2, and HNO_3 overnight dry-downs heated to 140ºC in a Teflon beaker. After digestion, the samples were dried down before being redissolved in 13 mL of 2% HNO_3.

2.3 Trace Metal Concentration and Isotope Analysis (USF)

2.3.1 USF Clean Lab Procedures

Clean lab work was performed in an ISO Class 5 laminar flow hood inside of an ISO Class 6 lab space at USF CMS. Ultrapure water (UPW) was used from a Thermo Scientific Barnstead GenPure (18.2 MΩ) water purification system. All nitric (HNO_3) and hydrochloric (HCl) acids used were distilled in-house from trace-metal grade acid, using Savillex DST-1000 Acid Purification Systems. Other reagents used during clean lab chemistry were ultrapure Fisher Optima Grade. Cleaning procedures for plasticware in the lab were performed following Conway *et al.* (2013) and are only described briefly here. Low density polyethylene (LDPE) plasticware was cleaned by immersing in a weak Citrad detergent solution overnight,

thorough rinsing with UPW, immersion in 1M HCl for at least a week, and then copious rinsing with UPW. New Savillex™ or Nalgene Teflon PFA, FEP, and PFTE plastic equipment were cleaned with sequential soaking in 7M HNO_3, 6 M HCl, 2% HNO_3, and 3 M HNO_3 at 150°C. Re-used Teflon plasticware was cleaned overnight at 150°C using 3M HNO_3. Whatman polycarbonate Nucleopore (8 μm pore size) filters were cleaned with 6M HCl for a week and stored in a weak HNO_3 solution.

2.3.2 Chemical Methods

To measure trace metal isotope ratios in seawater by MC-ICPMS, the metals of interest require purification from both the sea salt matrix and any interfering elements (see Table A1). This was achieved here using a two-stage extraction and purification method (Conway *et al.,* 2013; Sieber *et al.*, 2019, described in detail below. For soluble aerosol samples with larger sample volumes, both steps were used, while for digested bulk and size-fractionated aerosol samples, only the purification step was necessary.

2.3.2.1 Trace Metal Extraction Procedure (Nobias-PA1)

To prepare soluble aerosol samples for trace metal extraction, Fe, Zn, and Cd double spikes were added to each acidified sample in a sample:spike ratio of 1:2, 1:1, and 1:1, respectively, based on initial concentration measurements performed at UGA. Additionally, 1 mL of 10 mM hydrogen peroxide per liter of UPW was added and samples were left overnight to equilibrate. Subsequently, ~0.8 g (2.5 mL) of Nobias PA-1 resin was added and shaken on a shaker table for ~2 hours to allow Fe to adhere to the resin. To extract Zn and Cd, a 5 M ammonium acetate buffer solution and 11 M NH_4OH, was added to adjust the pH of the sample to 6.2 (± 0.3) and shaken again for ~2 hours. The resin was then filtered from the UPW matrix using a PFA filter rig-vacuum and Whatman polycarbonate Nucleopore (8 μm pore size) filter. To remove any remaining salt ions, the resin was rinsed with ~150-200 mL of UPW. Subsequently, trace metals were eluted using ~30 mL of 3 M HNO_3, collected in a 30 mL Savillex PFA beaker and dried down at ~180°C.

2.3.2.2 Trace Metal Micro-Column Purification Procedure (AGMP-1)

For total and size-fractionated digested samples, aliquots were pipetted into 7 mL PFA beakers, spiked with double spikes as above, and evaporated to dryness. For soluble samples, dried down samples were taken from the previous step (Section 2.2.2.1). To ensure digestion of any organic material in the samples, 180 µL of 15 M HNO_3 and 20 µL of conc. H_2O_2 were added, the samples refluxed at 180°C for 1-2 hours and dried down again. The samples were then redissolved in 200 µL of a 7 M HCl + 0.001% H_2O_2 solution for microcolumn purification with AGMP-1 anion-exchange resin (Bio-Rad), following Sieber *et al.* (2019a). For this, inhouse PTFE micro-columns were filled with ~20 µL of acid cleaned AGMP-1 resin, pretreated with four aliquots of 250 µL of 7 M HCl + 0.001% H_2O_2, and then rinsed with five aliquots of 60 µL of UPW. The columns were conditioned with 200 µL 7 M HCL + 0.001% H_2O_2 prior to sample loading. Ni, Cu, and any remaining salts were eluted in 7 aliquots of 60 µL 7 M HCl + 0.001% H_2O_2, which was discarded. Following this, 6 aliquots of 60 µL 1 M HCl were added to the columns to elute Fe from the resin and collected into 7 mL PFA beakers. Next, 6 60 µL aliquots of 2 M HNO_3 + 0.1 M HBr were added to the columns and collected in 7 mL PFA beakers for Zn. Subsequently, 6 60 µL aliquots of 2 M HNO_3 were added to elute the Cd into separate 7 mL PFA beakers. The Fe, Zn, and Cd samples were dried down before being redissolved in 2% v/v HNO_3 for MC-ICP-MS analysis.

2.3.3 Double Spike Technique

Double spike mixtures contain an unnatural isotopic ratio and are prepared by dissolution of two enriched isotope 'spikes' (in our case either ^{57}Fe-^{58}Fe, ^{64}Zn-^{67}Zn, or ^{111}Cd-^{113}Cd). Addition of double spike prior to processing allows to correct for any fractionation that may occur during chemical processing, as well as instrumental mass bias during measurement on the Neptune MC-ICPMS (Bermin *et al.*, 2006). Double spike calculations are completed using a data reduction method based on the iterative approach of Siebert *et al.* (2001). Additionally, the use of double spike technique allows for accurate concentration measurements via the isotope dilution technique, simultaneously with isotope analyses.

2.3.4 MC-ICPMS Analytical Methods

Analyses of stable Fe, Zn, and Cd isotope ratios were performed on a Thermo Scientific Neptune MC-ICP-MS in the Tampa Bay Plasma Facility at USF CMS, using previously published methods (Conway *et al.*, 2013; Sieber *et al.*, 2019a; Sieber *et al.*, 2021). Fe was measured in 'high' resolution, and Zn and Cd in 'low' resolution mode. Samples were introduced via a ~100 uL per min ESI PFA-ST nebulizer, and either an Apex-Ω (Fe, Zn) or Apex-Q desolvator (Cd). The cones, 'cup-configuration,' and the major interferences on each isotope (isobaric and polyatomic) are listed for each element in Table A1. A measurement of blank 2% HNO_3 dilution acid is made before every sample and standard, and used as an on-peak blank correction, and isotope voltages are mathematically corrected for isobaric interferences using natural abundances (Table A1).

For all three elements, delta notation is used (Equations 4-6), and ratios are expressed relative to international isotope standards (IRMM-14 for δ^{56}Fe; JMC-Lyon for δ^{66}Zn, and NIST SRM-3108 for δ^{114}Cd); during each analytical session on the Neptune, isotopic 'zero' standards (δ^{56}Fe: IRMM-014; δ^{66}Zn: JMC-Lyon; δ^{114}Cd: NIST SRM-3108) are measured before and after every five sample measurements (Conway *et al.*, 2013), and data expressed relative to these. A secondary isotopic standard (δ^{56}Fe: NIST-3126a; δ^{66}Zn: AA-ETH; δ^{114}Cd: BAM-1012) is measured with each block of 5 samples in order to assess accuracy and external precision (discussed further in next section).

It is important to assess uncertainty (precision and accuracy) of any measurements made. Typically, the amount of sample required for isotope analyses of low concentration marine samples means that replicate isotope analyses are not possible. Therefore, instead of using replicates to assess analytical precision, the long term 2SD of the mean isotope ratio obtained from the secondary standard reference solutions is used to assess precision of MC-ICPMS analysis. For Fe, this is the NIST-3126a standard (δ^{56}Fe: +0.36 ± 0.05‰, n = 524, runs = 37). For Zn, AA-ETH is the standard (δ^{66}Zn: +0.27 ± 0.03‰, n = 147, runs = 10). For Cd, this is the BAM-1012 standard (δ^{114}Cd: -1.32 ± 0.06‰, n=172, runs = 8). The mean δ^{56}Fe value for NIST-3126a at USF is in good agreement with previous measurements of +0.32 ± 0.02‰ made by Conway et al. (2013). Similarly, δ^{66}Zn and δ^{114}Cd values for AA-ETH and BAM-1012 agree with

published compositions of +0.28 ± 0.02‰ and -1.33 ± 0.04‰, respectively (Abouchami *et al.*, 2013; Archer *et al.*, 2017). For sample data, we use these values as a conservative estimate of precision for each isotope system, except if the internal 2SE of analysis is larger, and then this value is used.

Trace metal concentrations were calculated by isotope dilution; Conway *et al.* (2013) previously assessed the uncertainty of this method as 2%, and we apply the same uncertainty here. Uncertainty on Fe concentration measurements with this analytical method at USF has also been confirmed at ~2% for all three elements (Sieber *et al.*, 2019; Summers, 2020).

Eq. 4
$$\delta^{56}Fe = \left[\frac{\left({}^{56}Fe/{}^{54}Fe \right)_{Sample}}{\left({}^{56}Fe/{}^{54}Fe \right)_{IRMM-014}} - 1 \right] \times 1000$$

Eq. 5
$$\delta^{66}Zn = \left[\frac{\left({}^{66}Zn/{}^{64}Zn \right)_{Sample}}{\left({}^{66}Zn/{}^{64}Zn \right)_{JMC-Lyon}} - 1 \right] \times 1000$$

Eq. 6
$$\delta^{114}Cd = \left[\frac{\left({}^{114}Cd/{}^{110}Cd \right)_{Sample}}{\left({}^{114}Cd/{}^{110}Cd \right)_{NIST\ SRM-3108}} - 1 \right] \times 1000$$

2.4 Elemental and Isotopic Calculations from Neptune ICPMS Data

2.4.1 Trace Metals in Complete (Bulk and Soluble) and Size-fractionated Aerosols

Following calculation of Fe, Zn and Cd concentration in each analyzed 'blank' or total or soluble aerosol sample aliquot, this concentration must be converted to a mass of each metal in the original aerosol sample processed. This calculation was carried out using Equation 7:

Eq. 7 $$Trace\ Metal\ Sample\ Mass\ (ng) = TM_{sample\ or\ blank} = [TM]_{aliquot} \times \left(\frac{Volume_{total}}{Volume_{aliquot}}\right)$$

Where $[TM]_{aliquot}$ and $Volume_{aliquot}$ are the concentration and volume of the aerosol aliquot measured at USF, and $Volume_{total}$ is the total volume the original aerosol sample was digested or leached into. Each total and soluble sample was then blank corrected with their respective blank (with blank mass similarly calculated using Eq 7), using Equation 8:

Eq. 8 $$Blank\ Corr.Trace\ Metal\ Sample\ Mass\ (ng) = TM_{sample} - TM_{blank}$$

Where the blank for soluble samples was defined as the average of two USF measured blank filter leaches (Fe: 59 ng; Zn: 5.6 ng), and the blank for total samples was defined as the average of two USF blank filter digestions (Fe: 4.2 ng). For total and soluble Zn samples and soluble Cd samples, blanks were very low, and constituted a small amount (<10%) of Zn and Cd; accordingly, these parameters were not blank corrected (Marsay, pers. Comm.). Blank-corrected masses were then converted from ng to picomoles and divided by the total volume (m^3) of air used for sample collection during each GP15 deployment to provide a soluble and bulk atmospheric concentration for each metal from each deployment (Atmospheric [TM]) in pmol m^{-3} using Equation 9):

Eq. 9 $$Atmospheric\ [TM]\left(\frac{pmol}{m^3}\right) = \frac{[Blk\ Corr.TM * \left(\frac{TM\ mass\ (ng) * 10^{-3}}{Molar\ Mass\ TM}\right)]}{Volume_{air}\ (m^3)}$$

Metal masses in size-fractionated digested aerosol samples were also calculated using Eq. 7, and then blank corrected and scaled to the full filter using the ratio of total number of filter strips to the number of filter strips that were digested (Equation 10.). Ratios of 9:2, 10:2, and 10:1 were used for stage one, stages two to five, and backing filter, respectively. The blank for size-fractionated stage filter concentration

and isotope measurements is defined as the average of five blank stage filter digests (Fe: 82.3 ng), and the blank for backing filter aerosols is defined as the average of three blank backing filter digestions (Fe: 87.9 ng). Blank corrected size fractionated calculations were done separately for USF and UGA data, and the reported values are the average of USF and UGA measurements. The masses were then converted to atmospheric aerosol concentrations using Equation 9:

Eq. 10 $$Blank\ Corr.TM\ (ng) = \frac{\left[TM_{sample} - AverageTM_{blank}\right] \times \#\ total\ strips}{\#\ digested\ strips}$$

2.4.2 Aerosol Trace Metal Isotope Compositions

Trace metal isotopic compositions of bulk total (Fe and Zn), soluble (Fe, Zn, and Cd) and size-fractionated (Fe) samples were measured as described in Section 2.3.4. These compositions were then blank corrected using the measured isotopic composition of aerosol blanks and the relative masses of samples and blanks via equation 11:

Eq. 11 $$\delta\mathrm{TM}(‰) = \frac{[(\delta\mathrm{TM}_{sample} \times TM_{sample}) - (\delta\mathrm{TM}_{blank} \times Average\ TM_{blank})]}{Blank\ Corr.TM_{sample}}$$

The blank compositions for total δ^{56}Fe and δ^{66}Zn measurements was defined as the average of two blank filter digestions (Fe: +0.39 ± 0.05‰; Zn: -0.06 ± 0.05‰), and the Fe blank for soluble aerosol δ^{56}Fe was defined as the average of two blank filter leaches (Fe: +0.23 ± 0.09‰ ng). As with concentration calculations, soluble Zn and soluble Cd blank concentrations constituted only a small amount (<10%) of Zn and Cd and were also below detection for isotopic ratio measurement, so were not used to correct δ^{66}Zn and δ^{114}Cd. Unfortunately, bulk δ^{114}Cd data were compromised by a Sn interference, and so total δ^{114}Cd are not presented. Total size-fractionated Fe samples were corrected similarly to total and soluble Fe samples for blank isotopic composition; stages one to five samples were corrected using the average Fe

concentrations and δ^{56}Fe of five clean and unused stage filters, and the backing filters were corrected using the average concentrations and δ^{56}Fe of three clean and undeployed backing filters.

2.4.3 Trace Metal Operational Solubility and Enrichment Factor Calculations

An average operational solubility for each element for each GP15 deployment was calculated three times using one soluble concentration from leaching one discrete filter (USF) and three total concentrations from digests of three discreet filters (2 USF and 1 measured at UGA; Equation 3) per deployment. This provides some estimate of variability in solubility between filters, assessed by calculating the standard deviation between the three solubilities. Enrichment factors for odd deployment GP15 aerosols (Equation 2) are taken from Marsay *et al.*, (2022), and shown in the supplementary Fig. A2 (Marsay *et al.*, 2022).

2.4.4 Total and Coarse and Fine Binned Size-fractionated Fe Calculations

A weighted mean δ^{56}Fe signature of all size fractions in a size-fractionated aerosol deployment was calculated to compare with the representative bulk deployment δ^{56}Fe composition (Equation 12). Here, $\delta^{56}Fe_i$ denotes the isotopic composition for a filter stage and Stage $[Fe]_i$ denotes the respective Fe concentration for that filter stage.

Eq. 12
$$Weighted\ Mean\ \delta^{56}Fe\ \ (‰) = \frac{\sum(\delta^{56}Fe_i \times Stage\ [Fe]_i)}{\sum Stage\ [Fe]}$$

Using Equation 12, size fractions were binned to generate ‘coarse’ and ‘fine’ aerosol mean compositions. This was done in two different ways, based on earlier studies: 1) defining ‘coarse’ particles as >3 μm (stages 1-3) and fine as <3.0 μm (stages four to backing filter); and 2) defining ‘large particles as >0.95 μm (stages 1-4) and ‘small’ particles as <0.95 μm (stage five and backing filter). The first (coarse/fine) was done here to make our measurements comparable to existing δ^{56}Fe size fractionation studies in the North Pacific (e.g., Kurisu *et al*., 2021), which used 2.5 μm as their size cutoff (3.0 μm is the

nearest cutoff available for GP15 size-fractionated aerosol samples). However, previous work has also shown that a 1 μm as size cutoff may be a more effective size partitioning between natural and anthropogenic Fe aerosols (Kurisu *et al.*, 2016), and so we also calculated the second size-fraction definition (small/large) to provide further insight into Fe source along GP15. We also recommend that this second definition is calculated routinely going forward.

CHAPTER THREE:

RESULTS

Please note: GP15 aerosol total and soluble Cd concentrations and soluble δ^{114}Cd from this work are also available in Sieber *et al*. (in review); other data are presented here for the first time.

3.1 GP15 Atmospheric Setting

GP15 provided the opportunity to assess the atmospheric deposition of Fe, Zn, and Cd to the North Pacific Ocean during the low-dust season (Marsay *et al.*, 2022). Three-day HYSPLIT back-trajectory models were used to observe if characteristics of GP15 aerosol deployments (Fig. 7) could be related to distinct air masses coming from the coasts of East Asia or North and South America; however, there were no apparent air masses that had interacted with land recently (Marsay *et al.*, 2022). At the longer scale, ten-day back trajectories for the dates and locations of each deployment show that deployments 1 and 3 were influenced by air masses that had interacted with the Alaskan coast, while other northern deployments (5-11) were influenced by air masses travelling from the west originating in East Asia, and southern deployments (13-23) by air masses from the east from North and South America (Marsay et al., 2022). It is worth noting, however, that the uncertainty of back-trajectories significantly increases as the hindcast period increases (Buck, pers. comm.; Marsay, pers. comm.). Based on the general atmospheric circulation in the North Pacific (Fig. 4) and 10-day HYSPLIT models (Figs A3-5), we divide GP15 deployments into margin (deployments 1 and 3), northern (52°N to 32°N; deployments 5, 7, 9 and 11), and southern (20°N to 20°S; deployments 13, 15, 17, 19, 21, and 23; see Section 1.7) for interpretation. Additional GP15 metadata is provided in Appendix A (Table A2). We note that margin and northern deployments, referenced in this thesis, correspond to "North Pacific" deployments from Marsay *et al.* (2021), and that our southern

deployments correspond with their "equatorial Pacific" deployments. Additionally, while deployments are referenced as deployment 1, 3, 5, etc. throughout this thesis, deployments are referenced as Aer1, Aer3, Aer5, etc. in Marsay *et al.* (2021).

3.2 USF and UGA GP15 Total Aerosol Comparisons

Bulk digests of three discrete filters from each deployment were measured at USF (two filters) or UGA (one filter; Marsay *et al.*, 2022), allowing us to assess variability of concentrations obtained from the same aerosol deployments, as well as compare datasets between the two laboratories. Iron and Zn show broad agreement between labs and filters, with Fe showing excellent agreement between the three filters, and Zn showing more variability between filters (Fig. 8). This likely reflects more variability between aerosol filter loading for Zn than Fe, rather than analytical issues. Overall, total GP15 Fe concentrations ranged from 14.1 to 157 pmol m^{-3} (USF) and 10.7 to 144 pmol m^{-3} (UGA), total GP15 Zn concentrations ranged from 3.40 to 16.5 pmol m^{-3} (USF) and 4.30 to 18.7 pmol m^{-3} (UGA), and total GP15 Cd concentrations ranged from 0.10 to 0.27 pmol m^{-3} (USF) and 0.01 to 0.24 pmol m^{-3} (UGA). Given the broad overall agreement between labs, we regard the average of the three discrete filters as providing the most representative value for each total concentration measurement for Fe and Zn, and for representing variability during calculation of elemental solubilities. Thus, total Fe and Zn concentrations used in this study represent the average of USF and UGA measurements (Table 2). Uncertainty on total concentrations is expressed as the standard deviation from the three separately digested filters (data from Marsay *et al.*, 2022 and this study). Total Cd data from UGA was not available for comparison at the time of writing, and so the average (and standard deviation) of the two USF Cd measurements is used here instead. Enrichment factors are taken directly from UGA data (Marsay et al., 2022).

3.3 GP15 Aerosol Fe, Zn, and Cd Concentrations, Solubilities and Enrichment Factors

GP15 bulk and soluble aerosol Fe, Zn, and Cd concentrations are displayed in Fig. 9 and data are also tabulated in Table 2. GP15 solubilities are shown in Fig. 10 and Table 3 while Fig. 11 and 12 displays Fe EFs compared to Mn, Zn, and Ni EFs and Zn EFs compared to Mn and Ni EFs, respectively.

Fe. GP15 Total aerosol Fe concentrations range from 13.0 to 152 pmol m^{-3}, while soluble Fe concentrations range from 0.3 to 7.0 pmol m^{-3} (Fig. 9), leading to Fe solubilities from 0.80-11.3% (Fig. 10). Total aerosol Fe concentrations are higher for northern deployments (52°N to 32°N) than for the southern (20°N to 20°S) and margin deployments (Fig. 9). This dichotomy agrees with previous observations in the North Pacific which found the highest bulk Fe concentrations between 50°N and 20°N (Buck *et al.,* 2006; Buck *et al.,* 2013). Soluble Fe concentrations exhibit a similar pattern, with higher concentrations at northern and margin deployments (3 to 15 pmol m^{-3}), and the highest values at deployments 1, 5, and 9 (15, 10, and 11 pmol m^{-3}; Fig. 9). Iron solubility is highest at the margin deployments (7-11%) and follows a general decrease over the rest of the deployments (5 to 1%; Fig. 10) but does not correlate with either total or soluble Fe concentrations.

Notably, aerosol Fe concentrations measured along GP15 during September to November 2018 are among the lowest observed for bulk and soluble aerosols over the North Pacific Ocean; for example, bulk Fe measured on the CLIVAR-CO_2 P16 leg, also along 152ºW from January to March, ranged from 23 to 2350 pmol m^{-3} while soluble Fe ranged from 0.7 to 343 pmol m^{-3} (Buck *et al.*, 2013). The fourth Intergovernmental Oceanographic Contaminant Baseline Survey (IOC) along 170ºN observed bulk values of 257 to 4932 pmol m^{-3} and soluble values of 1 to 148 pmol m^{-3} (Buck *et al.*, 2006). This difference with previous study can be attributed to the time of sampling, with the main Asian dust peak occurring outside our sampling dates (Buck *et al.*, 2006; Buck *et al.*, 2013).

Enrichment factors were not calculated by Marsay *et al.* (2022) for deployments 1 and 3 as Ti concentrations were below the detection limit. Other EFs are shown in Fig A2. Iron EFs do not show any clear enrichments in Fe with values ranging from 0.9 to 3 (c.f. natural <10; Buck *et al.*, 2019; Perron *et al.*, 2022), although southern deployments Fe EFs are slightly elevated (1.29 to 3.11) in comparison to northern

deployments (<2; Fig. 11). While total and soluble Fe concentrations and solubility also do not correlate with Fe, Zn, Cd, Al, V, Mn, Ni, or Pb EFs, there are distinct relationships between the EFs of some elements; the 'natural tracer' Mn EFs are crustal in the northern deployments, and slightly elevated in the South (in comparison to the North), with Mn EFs correlating well with Fe, especially in the South (Fig. 11). Further, of the possible anthropogenic tracers, Zn and Ni are elevated in the northern deployments, and also well-correlated with Fe EFs, again especially in the South (Fig. 11).

Zn. Bulk and soluble Zn concentrations range from 3.9 to 17.2 pmol m^{-3} and 1.6 to 8.0 pmol m^{-3}, respectively, and are variable throughout the transect with no meridional concentration gradient or clear difference between northern and southern deployments (Fig. 9). Additionally, bulk and soluble Zn concentrations show no correlations with Zn solubility. Calculated Zn solubility spans a significantly larger range than Fe solubility with a minimum of 34% and maximum of 112% (Fig. 10) and does not show a systematic trend along GP15 or between regions. Elevated Zn solubilities are likely indicative of the presence of non-crustal Zn. Notably, deployments 1, 15, and 19 have solubilities ≥100% (Fig. 9); however, all of these are within error of 100%, and thus are most likely the result of variability in Zn loading between filters from the same deployments. As such, apparent calculated solubilities >100% highlight the variability in aerosol Zn between filters but are also likely indicative of a large fraction of anthropogenically-produced (expected to be more highly soluble) Zn.

Zinc EFs are highly elevated throughout GP15 ranging from 32 to 693, where >10 is anthropogenic, and are also strong indicators of non-crustal Zn. Total and soluble Zn concentrations and Zn solubility do not correlate or show any clear relationships with Zn, Fe, Cd, Al, V, Mn, Ni, or Pb EFs. However, Zn EFs do exhibit good correlations with Fe, Mn, and Ni EFs (Figs. 11 and 12) as well as show distinctions between regions; northern deployments (other than deployment 11) group together at the lowest (yet still significantly enriched over crustal) Zn and Ni EFs, while southern deployments exhibit higher Zn EFs that increase with increasing Ni, Fe, and Mn EFs (Figs. 11 and 12).

Cd. Cadmium bulk concentrations range from 0.01 to 0.27 pmol m^{-3} and soluble concentrations range from 0.01 to 0.11 pmol m^{-3} (Fig 9). Both bulk and soluble Cd concentrations are variable with no

clear trends along the transect. Cadmium solubility ranges from 24 to 175%, with only deployment 19 exhibiting solubility >100%, and exhibits a similar general trend as Zn solubility throughout the transect (Fig. 10). Cadmium EFs, ranging from 263 to 10774, are highly enriched throughout GP15 but do not show correlations with bulk and soluble aerosol Cd concentrations or solubility. Unlike Zn and Fe, there is no dichotomy between northern and southern deployments Cd EFs, nor clear relationships with other EFs.

3.4 Trace Metal Isotopic Compositions of GP15 Bulk and Soluble Aerosols

GP15 δ^{56}Fe, δ^{66}Zn, and δ^{114}Cd from bulk and soluble GP15 aerosols are displayed in Fig. 13 and data are also tabulated in Table 4.

Fe. Total aerosol GP15 δ^{56}Fe values range from -0.03 to +0.41‰ throughout the transect with deployments 15 and 21 exhibiting the highest δ^{56}Fe (+0.32 and +0.41‰; Fig. 13). While this range is broadly similar to the expected UCC range (-0.01 to +0.19‰), it extends beyond the crustal range, with subtle differences between regions: margin and southern deployments have δ^{56}Fe values that are close to or elevated beyond (up to +0.4‰) the maximum δ^{56}Fe signature of the UCC (+0.19‰), and northern deployments are at or slightly below (-0.03 to +0.07‰) the minimum δ^{56}Fe of the UCC (-0.01‰; Beard *et al.*, 2003; Gong *et al.*, 2016). This dichotomy is also observed when comparing total aerosol δ^{56}Fe with EFs – there are broad relationships between total δ^{56}Fe and Fe, Al, Mn, Ni, and Zn EFs (Figs 14 and A6). Notably, a striking relationship is observed between δ^{56}Fe and Al EFs with the heavier total δ^{56}Fe of southern deployments corresponding to elevated Al EFs, while the lighter δ^{56}Fe of northern deployments correspond to crustal Al EFs and show non-natural V EFs (Fig. 14). For soluble aerosol Fe, most (9 out of 11) samples exhibit δ^{56}Fe values (-1.28 to -0.14‰) lower than crustal isotope signatures, with just deployment 1 and 21 having crustal values (+0.02 to +0.18‰). However, there are no clear relationships between soluble δ^{56}Fe and the EFs of any elements.

Zn. Total and soluble δ^{66}Zn values both generally decrease from north to south over the course of the transect, except for deployment 17, with values from -0.29 to +0.01‰ and -0.35 to +0.19‰, respectively (Fig. 13). All bulk and soluble GP15 deployment exhibit lower δ^{66}Zn than previously recorded in crustal

Zn aerosols (+0.20 to +0.34‰; Little *et al.*, 2014), with a mean of -0.11 ± 0.11‰ and -0.17 ± 0.15‰ for total and soluble aerosols, respectively. Total and soluble δ^{66}Zn do not show clear relationships with Fe, V, and Mn EFs (Fig. A7); however, the southward decrease in soluble δ^{66}Zn is also concurrent with a general increase in Zn EF (Fig. 15), suggesting an increasing input of light Zn through the section.

Cd. Soluble δ^{114}Cd are generally isotopically lighter than the crust (-0.04‰; Fig. 3; e.g., Schmitt *et al.*, 2009), with values ranging from -0.07‰ to -1.91‰, and is highly indicative of an anthropogenic contribution throughout GP15. In contrast to Fe and Zn, however, δ^{114}Cd compositions are highly variable along the transect and exhibit no apparent trends (Fig. 13).

3.5 Size-fractionated Bulk Fe Concentrations and Isotopes

A total of 12 size fractioned samples were collected during GP15, either during single aerosol deployments or spanning multiple deployments to get enough sample mass (3, 4, 5/6, 7/8, 9/10, 11/12, 13/14, 15/16, 17/18, 19/20, 21/22/23, and 23). GP15 bulk Fe concentrations and δ^{56}Fe are compared to GP15 total size-fractionated concentrations and δ^{56}Fe in Figure 16. Iron concentrations (average of USF and UGA measurements) and δ^{56}Fe are shown for each filter stage of each size-fractionated deployment (Fig. 17; Tables 5 and 6).

3.5.1 Comparison of Total 'Bulk' and Size-fractionated Aerosols

The overall composition (weighted mean of all stages) of the size-fractionated aerosols should correspond to the bulk aerosol loading for each GP15 aerosol deployment, allowing both to be used in our interpretation of sources to each deployment. Here, we assess the agreement/variability (Fig 16) of the two approaches for sampling bulk Fe and δ^{56}Fe for the deployments where we received size-fractionated aerosols (12 deployments). One caveat in this approach is that since the size-fractionated deployments span multiple standard aerosol deployments, we had to use the most relevant bulk deployment for comparison (or average where possible).

Overall, we find that while the weighted means of size-fractionated total Fe concentrations agree broadly with bulk Fe concentrations, the weight means systematically exhibit lower concentrations (16.3 to 116.9 pmol m^{-3}) than the bulk Fe samples (13.0 to 152 pmol m^{-3}). This offset could result from natural variability in sampling. Additionally, differences between total size-fractionated and bulk Fe concentrations and δ^{56}Fe could arise from different sampling methods for each sample type. Similar filters were used for both samples, but the type of impactor and the collected air volumes were different (see Section 2.2), possibly missing or biasing certain particle sizes. Nevertheless, the weighted mean of the size-fractionated total δ^{56}Fe agree within error with bulk total δ^{56}Fe samples, suggesting that both sampling methods are capturing aerosols of overall near-identical isotopic (and presumably source) compositions (Fig. 16).

3.5.2 *Total Fe Concentrations and δ^{56}Fe Composition by Filter Stage*

Figure 17 displays Fe concentrations and δ^{56}Fe of size-fractionated Fe aerosol samples grouped into northern, southern, and margin deployments, and the data is also tabulated in Tables 5 and 6. Concentrations throughout the various filter stages are generally higher for northern deployments (2.7 to 35.3 pmol m^{-3}) and the margin deployments (1.4 to 49.4 pmol m^{-3}) than southern deployments (0.9 to 19.6 pmol m^{-3}, Fig. 17), reflecting higher loading in the bulk phase in the North (Section 3.3). Overall, no distinct particle size range (or stage) dominates aerosol Fe throughout GP15, and while concentrations are higher for northern deployments, partitioning across stages does not show systematic differences between northern and southern deployments. There is a general decrease in δ^{56}Fe in the size-fractionated aerosols from stages 1 (>7.2 μm, +0.21 ± 0.28‰) to 5 (0.49-0.95 μm, -0.27 ± 0.28‰), corresponding to decreasing particle size, followed by a slight increase to +0.01 ± 0.28‰ in the smallest size-fraction collected in the backing filter (<0.49 μm; Table 6). In more detail, Stages 1 to 3 (>7.2 to 1.5 μm) δ^{56}Fe are variable throughout the transect (-0.29 to +0.37‰) and all but one (deployment 4, stage 1) are crustal or notably heavier. Stage 4 filters (0.95-1.5 μm) are also crustal or slightly heavier (-0.01 to +0.25‰), but deployments 3, 11/12, and 19/20 are only just within error (0.05‰) of the lightest end of the crustal range (-0.03‰, -0.02‰, and -0.04‰,

respectively). Stage 5 (0.49 to 0.95 μm) shows the largest variation among stages, ranging from -0.57 to +0.28‰, and the backing filters (<0.49 μm) range from -0.33 to +0.38‰. However, the large variation in the fine fraction (<3 μm) may reflect different Fe sources as northern deployments' stage 5 and backing filters carry light Fe, while southern deployments exhibit crustal or elevated δ^{56}Fe.

3.5.3 GP15 δ^{56}Fe *Composition Subdivided by Binned Particle Size*

A clearer picture of variability in δ^{56}Fe composition related to particle size emerges when binning the size-fractionated data into operationally defined coarse and fine fractions (Fig. 19). Isotope compositions of coarse particles (>3 μm; filter stages 1 and 2) range from +0.01 to +0.33‰, similar to bulk aerosol δ^{56}Fe (-0.03 to +0.41‰), reflecting the fact that bulk GP15 aerosols are dominated by coarse particles (Fig. 17). Fine particle δ^{56}Fe (<3 μm; stage 3 to backing filter) are also variable, but reach lower values, ranging from -0.50‰ to +0.30‰ (Fig. 19; Table 7). Light Fe in the fine fraction is strongly indicative of the presence of anthropogenic Fe particles (Kurisu *et al.*, 2021). However, it is worth noting that the fine fraction isotope compositions do not reach values as low as soluble δ^{56}Fe (-1.28 to +0.02‰) for corresponding deployments, and in fact, some fine size samples are crustal or isotopically heavy. This difference between fine particle digests and soluble Fe likely reflects the fact that soluble aerosol δ^{56}Fe is heavily influenced by highly soluble anthropogenic Fe, and less by insoluble dust Fe, while fine particles include a contribution of fine dust particles. As such, perhaps not unexpectedly, there is no clear dichotomy of natural and anthropogenic Fe between the coarse and fine fractions.

However, based on work by Kurisu *et al.* (2016), a binning threshold of 1 μm may better capture the anthropogenic Fe in the small particles compared to a 3 μm cutoff. As such, we also assessed GP15 data using a threshold of 0.95 μm for the binning method by dividing filters into 'large' and 'small' size particles as close as we can to sizes >1 μm and <1 μm, respectively (Fig. 19). On doing this, large particles (filter stages 1 – 4) have a slightly tighter range of δ^{56}Fe (+0.02 to +0.27‰) than coarse, while small particles occupy a similar range overall to fine (stage 5 and backing filter, -0.44 to +0.34‰; Fig. 19 and Table 8). Notably, however, there are distinct differences between northern and southern deployments; in the

northern deployments, small particles (<1 μm) are systematically ~2x lighter than fine particles (<3 μm), and more similar to 'soluble' δ^{56}Fe, while at margin and southern deployments, there is no systematic difference (Fig. 19). This suggests that the small/large definition may be more effectively separating light anthropogenic Fe from other sources than the fine/coarse threshold (at least in Asian dust), with the 'small' definition capturing fewer dust particles than the 'fine'. Thus, for future studies we recommend using a threshold near 1 μm, as initially suggested by Kurisu *et al.* (2016), to provide a better partitioning between natural dust and anthropogenic Fe aerosols.

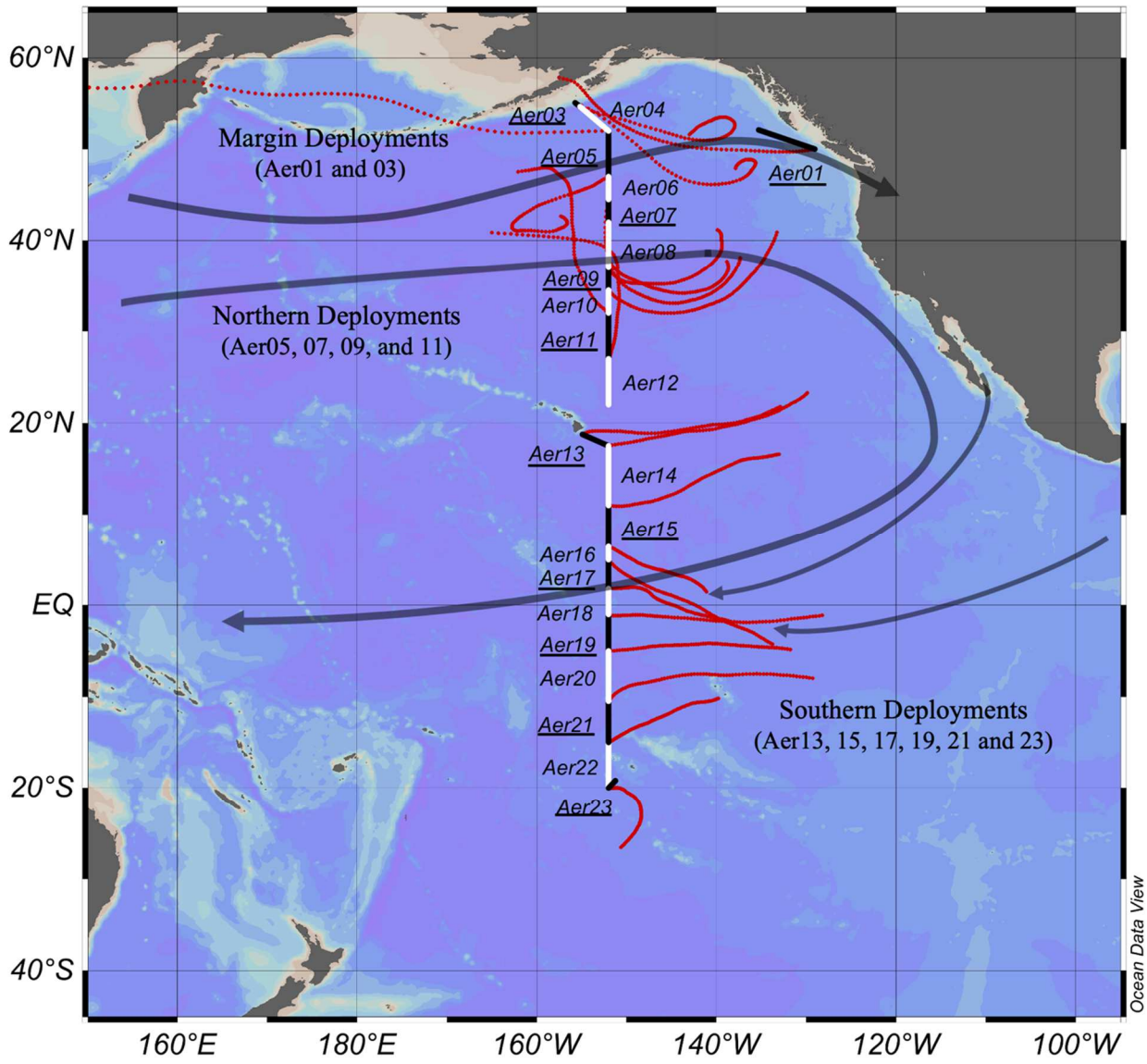

Figure 7. US GEOTRACES GP15 Aerosol Deployment Location Map. For each aerosol deployment corresponding 3-day air mass back trajectories (determined using HYSPLIT) are shown in red. Gray arrows represent the atmospheric circulation based on Martin *et al.* (2002). Bulk and soluble samples were collected during deployments 1, 3, 5, 7, 9, 11, 13, 15, 17, 19, 21, and 23, and size-fractionated samples were collected during deployments 3, 4, 5/6, 7/8, 9/10, 11/12, 13/14, 15/16, 17/18, 19/20, 21/22/23, and 23. (modified from Marsay *et al.*, 2021).

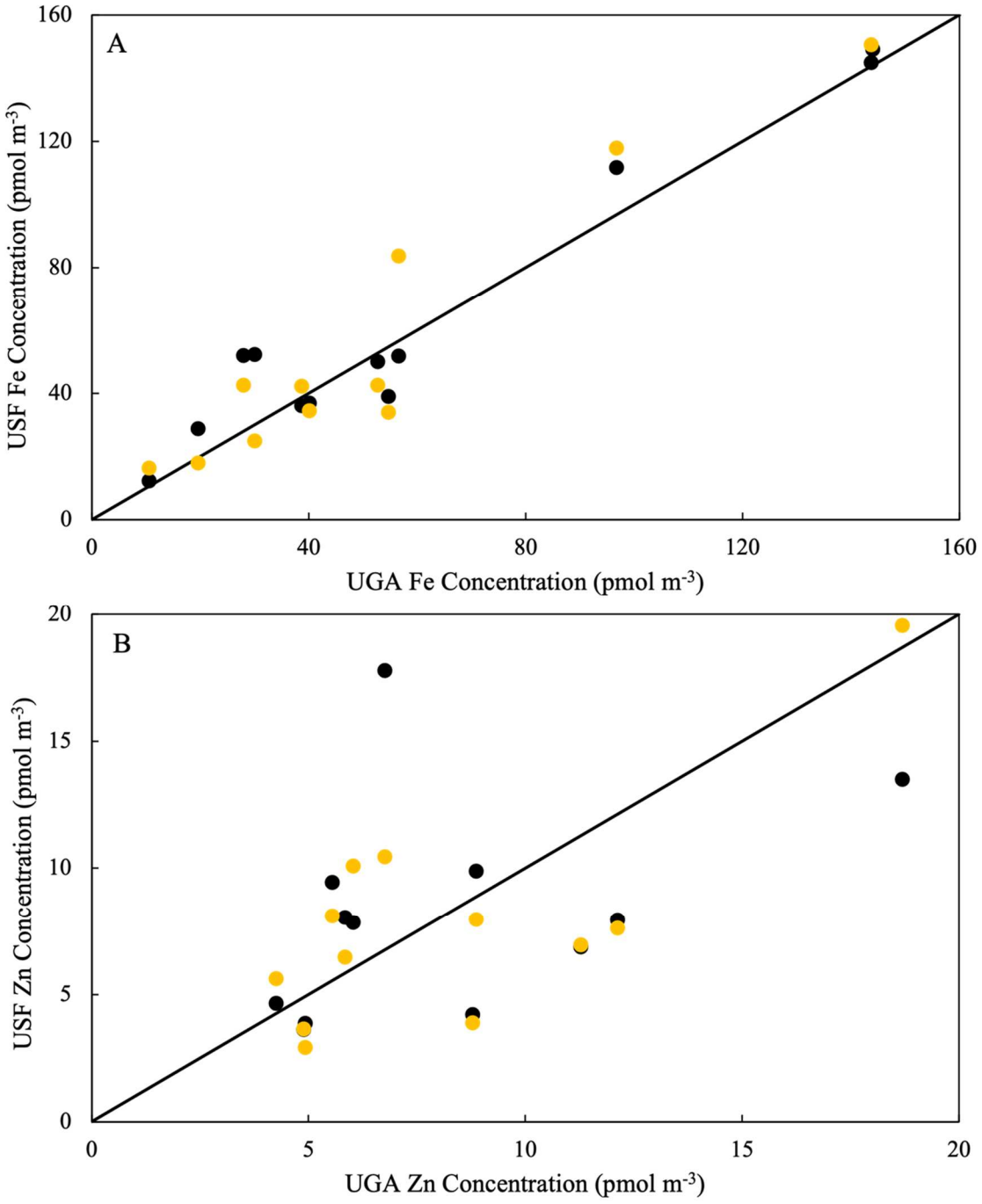

Figure 8. UGA and USF GP15 Total Aerosol Fe and Zn Concentration Intercomparison. GP15 bulk **A)** Fe concentrations and **B)** Zn concentrations. Black ciricles represent one USF bulk filter compared to one UGA bulk filter, and the yellow circles represent a second USF bulk filter compared to the same UGA bulk filter.

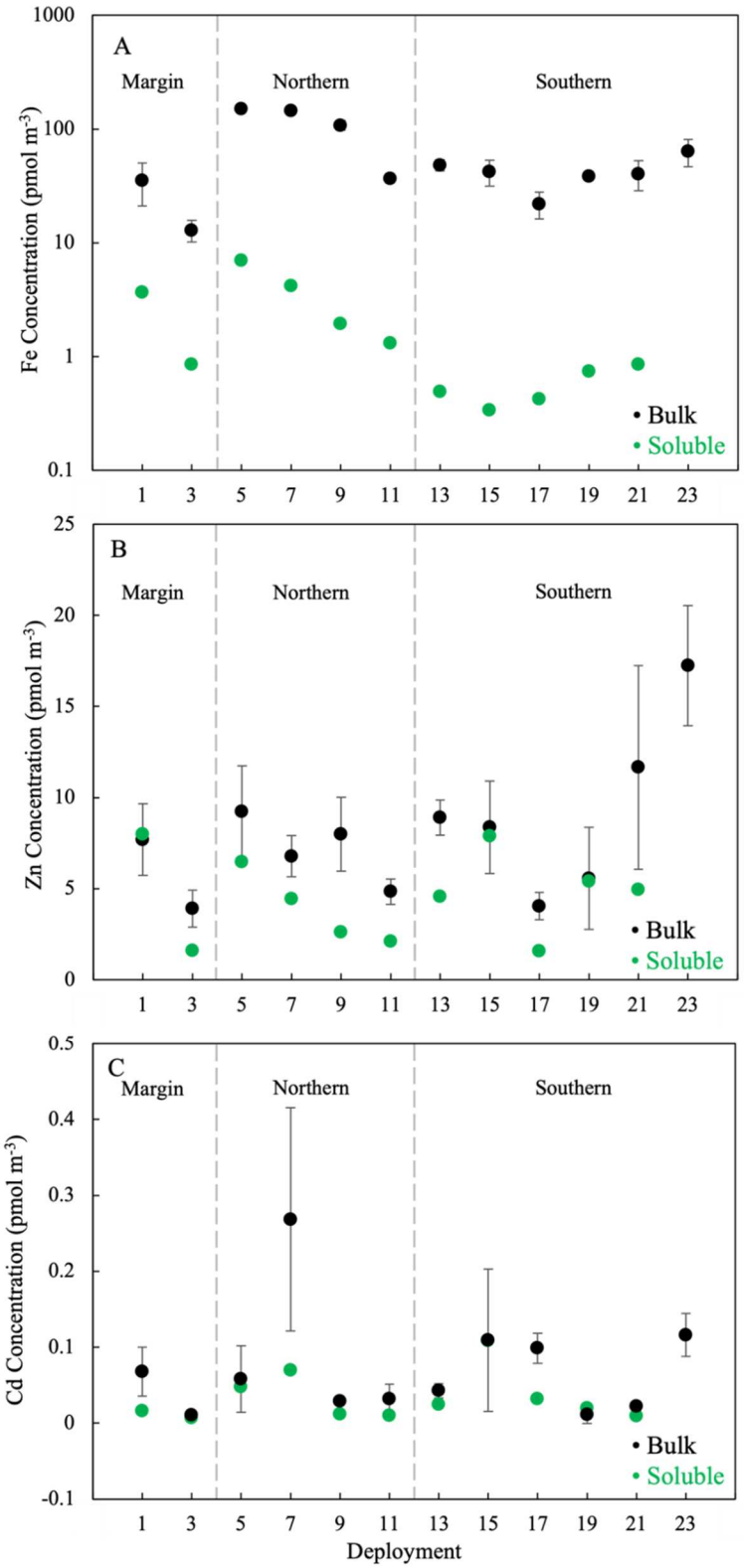

Figure 9: GP15 Total and Soluble Aerosol Trace Metal Concentrations. A) Fe, **B)** Zn, and **C)** Cd. Total concentrations are black circles and soluble are green. Error bars on total concentrations represent the standard deviation of the average of 2 USF filters and one UGA filter measurements and are shown where larger than the points.

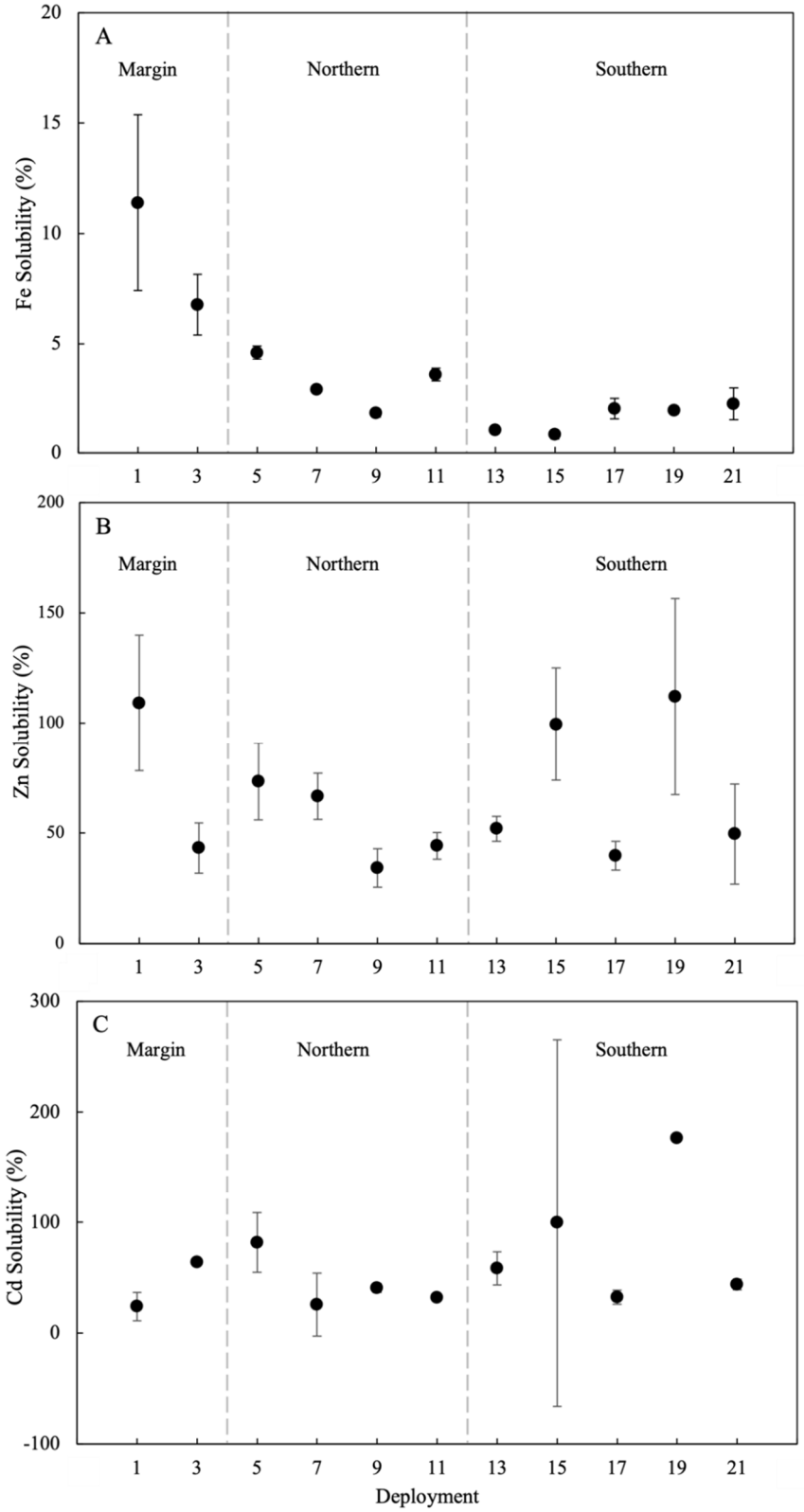

Figure 10: GP15 Aerosol Trace Metal Aerosol Solubilities. A) Fe, **B)** Zn, and **C)** Cd. Error bars are defined as the standard deviation between 3 discreet Fe and Zn and 2 Cd discreet solubility calculations and are shown where larger than the points.

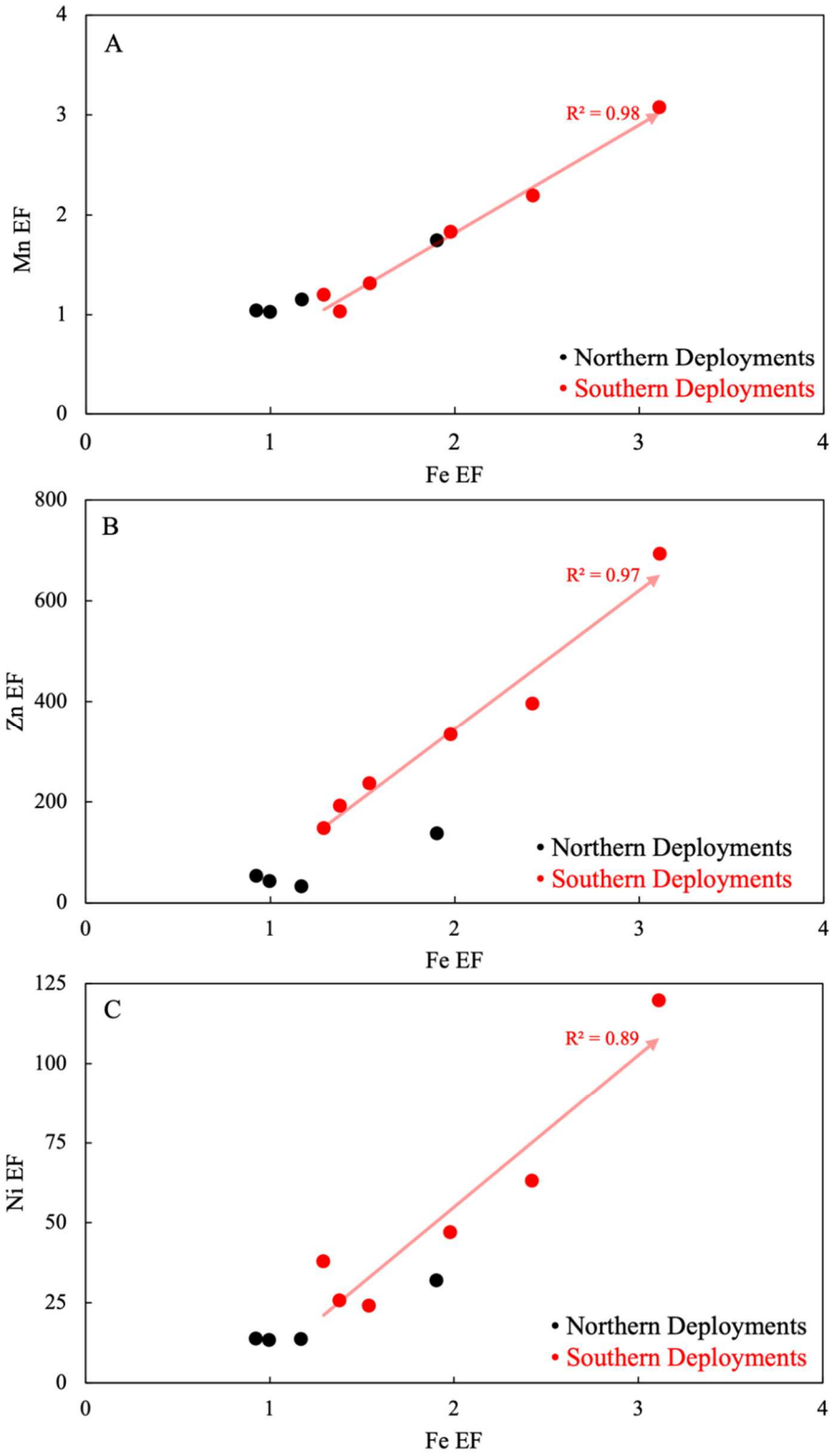

Figure 11. GP15 aerosol Fe EF Comparison with Mn, Zn, and Ni Enrichment Factors. Northern (black circles) and southern (red circles) deployments Zn EFs compared to **A)** Mn EF, **B)** Zn EF **C)** Ni EF. Lines represent the correlation (R^2) between the Fe and other TM EF of southern deployments. EFs are taken from Marsay et al. (2022) and are calculated using Eq. 2.

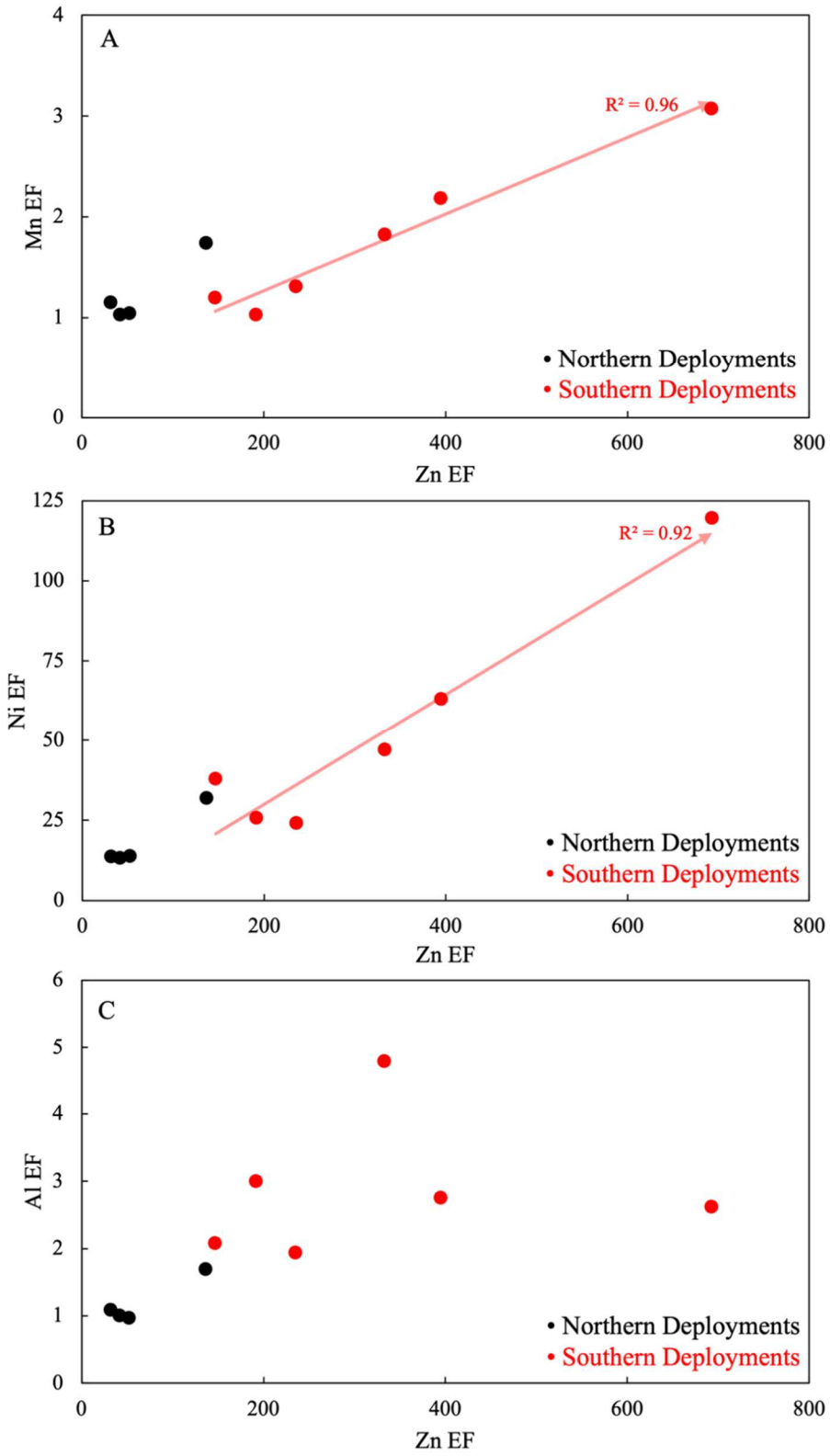

Figure 12. GP15 Aerosol Zn Comparison with Mn and Ni Enrichment Factors. Northern (black circles) and southern (red circles) deployments Zn EF compared to **A)** Mn EFs, **B)** Ni EFs, and **C)** Al EFs. Lines represent the correlation (R^2) between the Fe and other TM EFs of southern deployments. EFs are taken from Marsay et al. (2022) and are calculated using Eq. 2.

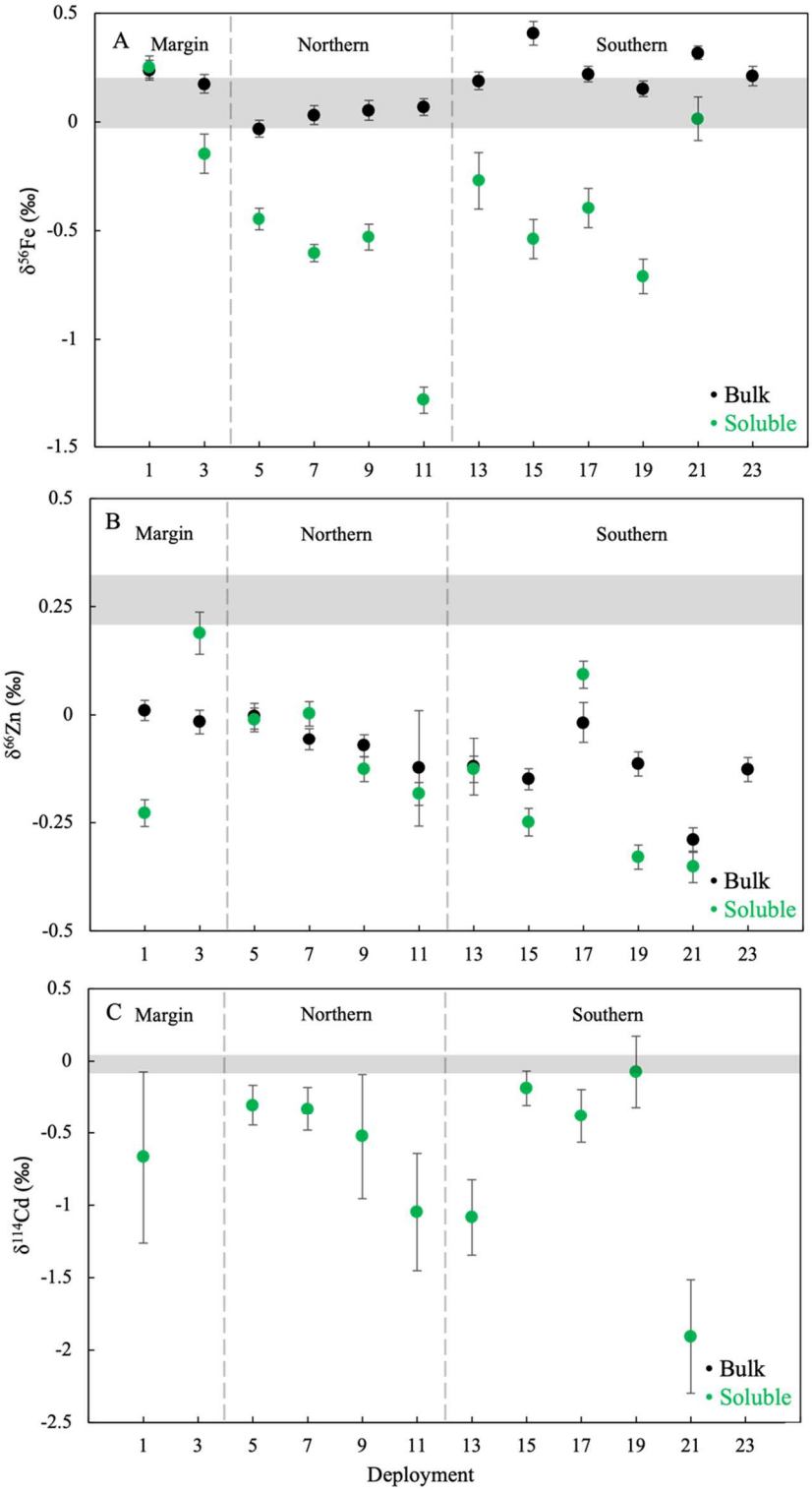

Figure 13. GP15 Aerosol Total and Soluble Trace Metal Isotope Ratios. A) Total (black circles) and soluble (green circles) δ^{56}Fe by deployment. The gray bar depicts the δ^{56}Fe range of crustal aerosols, -0.01 to +0.19‰ (Beard *et al.* 2003; Gong *et al.*, 2016). **B)** Total (black circles) and soluble (green circles) δ^{66}Zn by deployment. The grey bar depicts the δ^{66}Zn range of crustal aerosols, +0.27 to +0.34‰ (Little *et al.*, 2014). **C)** Soluble (green circles) δ^{114}Cd by deployment. The grey bar depicts the δ^{114}Cd range of crustal aerosols, -0.1 to +0.05‰ (Bridgestock *et al.*, 2017).

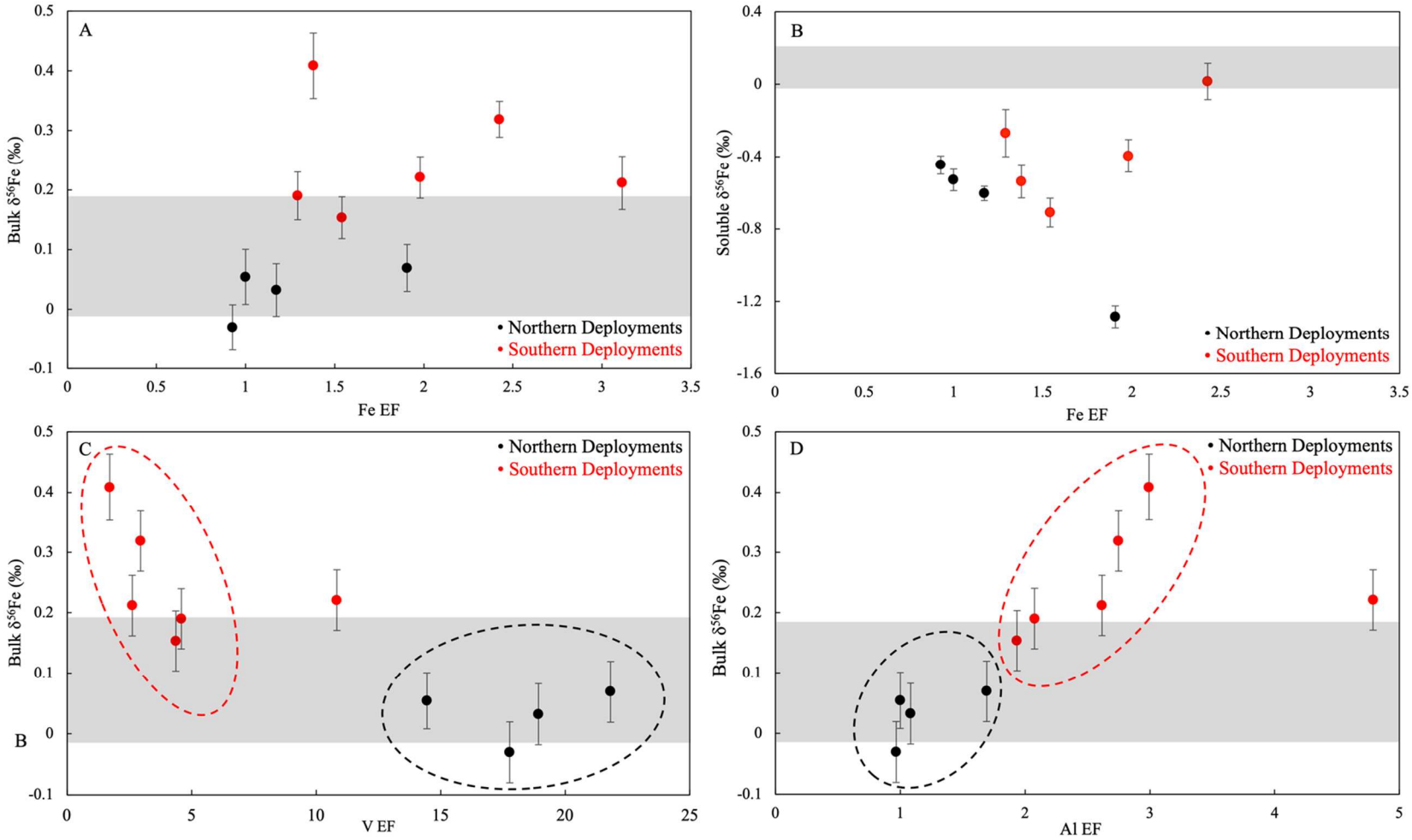

Figure 14. Comparison of Total and Soluble GP15 Aerosol δ^{56}Fe with Aerosol Enrichment Factors. Northern (black circles) and southern (red circles) deployment's **A)** total δ^{56}Fe vs. Fe EF, **B)** soluble δ^{56}Fe vs Fe EF, and bulk δ^{56}Fe compared to **C)** V EF and **D)** Al EF. The gray bar depicts the crustal aerosol δ^{56}Fe range (-0.01 to +0.19‰; Beard *et al.* 2003; Gong *et al.*, 2016). Dashed circles represent approximate fields of northern and southern aerosols. EFs are from Marsay *et al.* 2022.

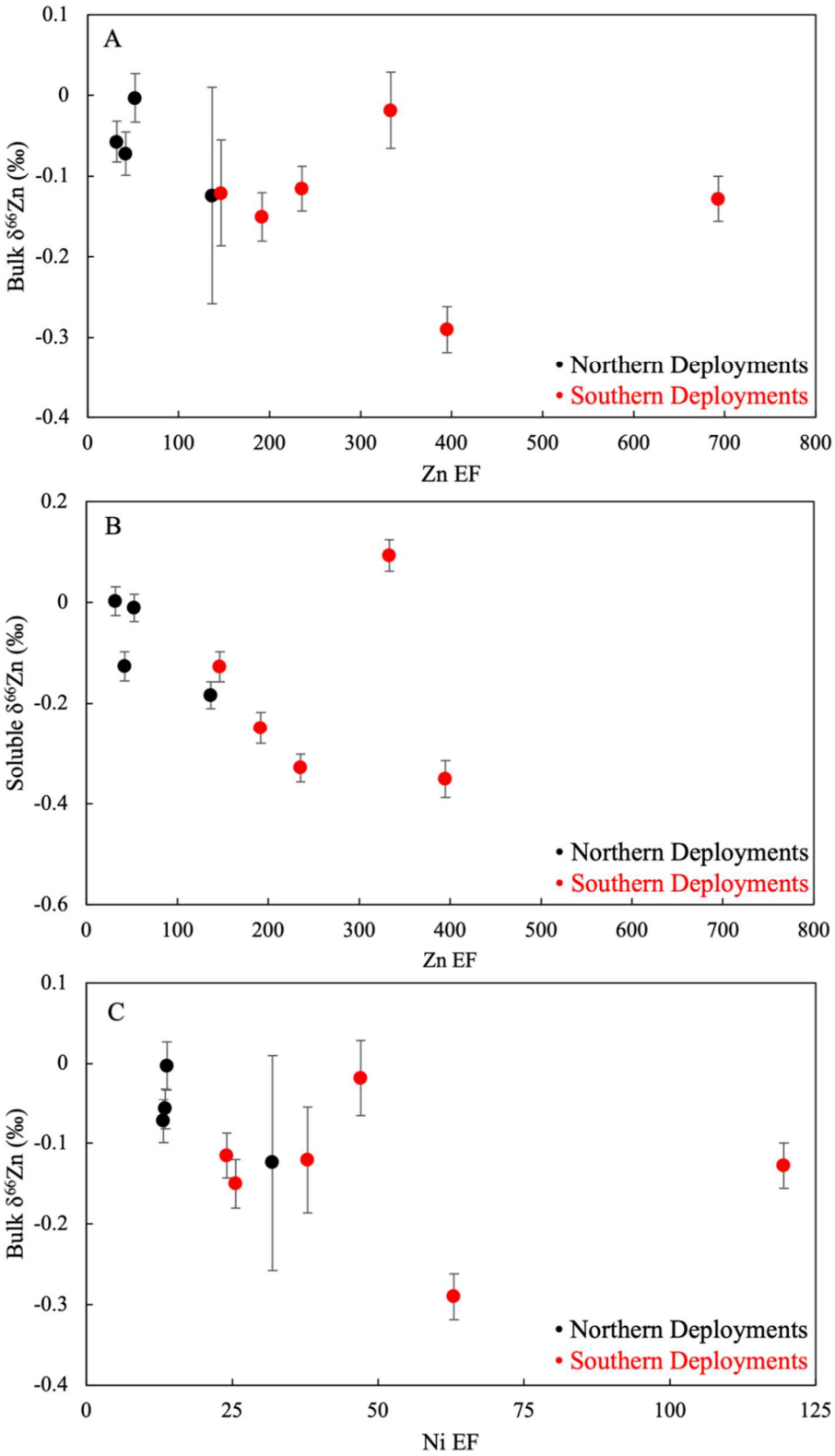

Figure 15. Comparison of Total and Soluble GP15 Aerosol δ^{66}Zn with Aerosol Enrichment Factors. Northern (black circles) and southern (red circles) deployments **A)** total δ^{66}Zn, and **B)** soluble δ^{66}Zn vs Zn EF, and **C)** total δ^{66}Zn compared to Ni EF. The crustal δ^{66}Zn range is from +0.20 to +0.34‰ but does not intersect with the plots (Little *et al.* (2014). EFs are from Marsay *et al.* 2022.

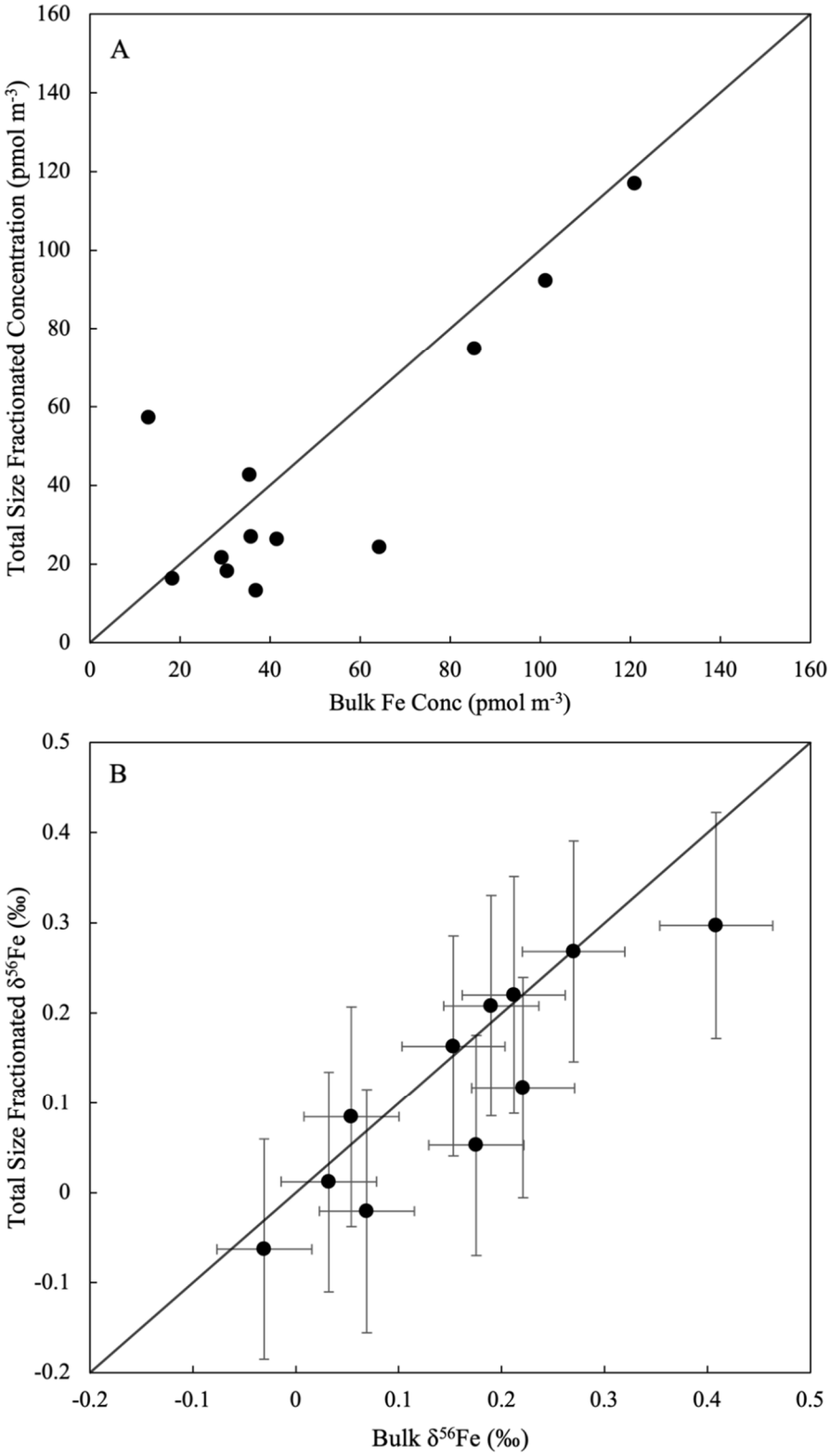

Figure 16. GP15 Total and Size-fractionated Weighted Total Fe Concentration and δ^{56}Fe Comparison. A) Total Fe concentrations compared to size-fractionated Fe concentrations, and **B)** total δ^{56}Fe compared to weighted total size-fractionated δ^{56}Fe. Error bars represent the analytical error for bulk δ^{56}Fe (x-axis) and the propagated error for the total size-fractionated δ^{56}Fe (y-axis).

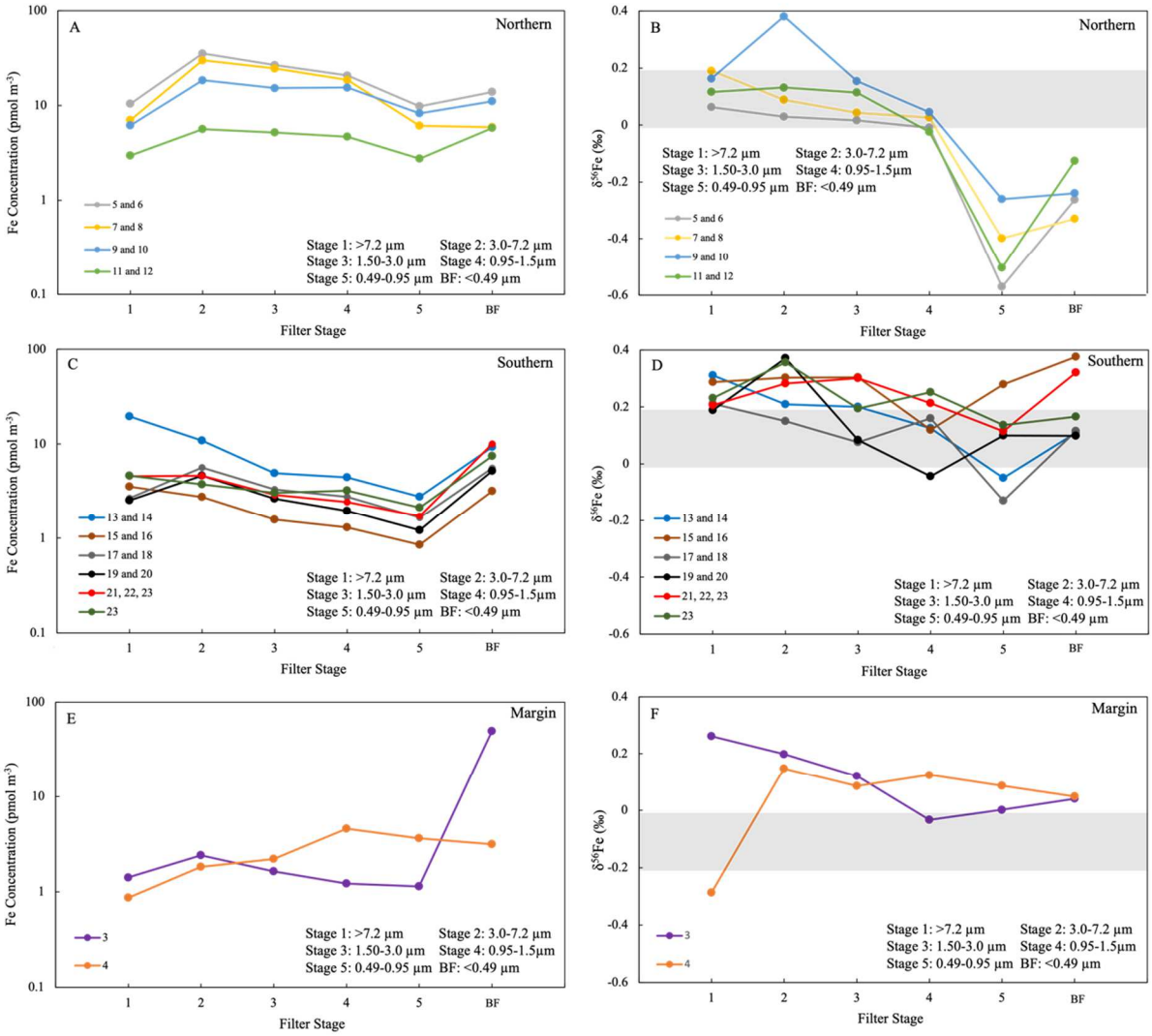

Figure 17. GP15 Size-fractionated Aerosol Fe Concentrations and δ^{56}Fe by Filter Stage. A-B) Northern deployments; **C-D)** southern deployments; **E-F)** margin deployments. The gray bars depict the crustal δ^{56}Fe range (-0.01 to +0.19‰; Beard *et al.,* 2003; Gong *et al.*, 2016.). For clarity, error bars on δ^{56}Fe are not shown, but errors are typically 0.05‰ (see Table 3 for detail).

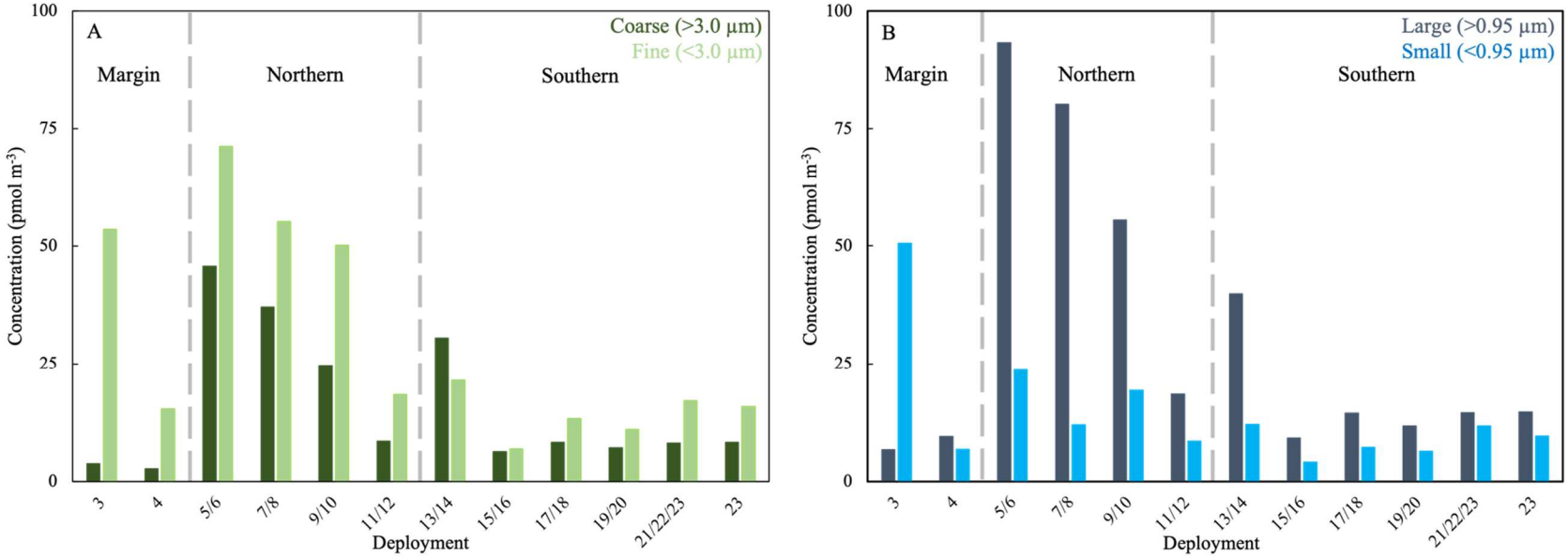

Figure 18. GP15 Coarse/Fine (3 µm) and Large/Small (0.95 µm) Total Aerosol Concentrations. A) coarse (dark green) and fine (light green) size-fractionated Fe concentrations using a threshold of 3 µm and **B)** large (dark blue) and small (light blue) size-fractionated Fe concentrations using a threshold of 0.95 µm.

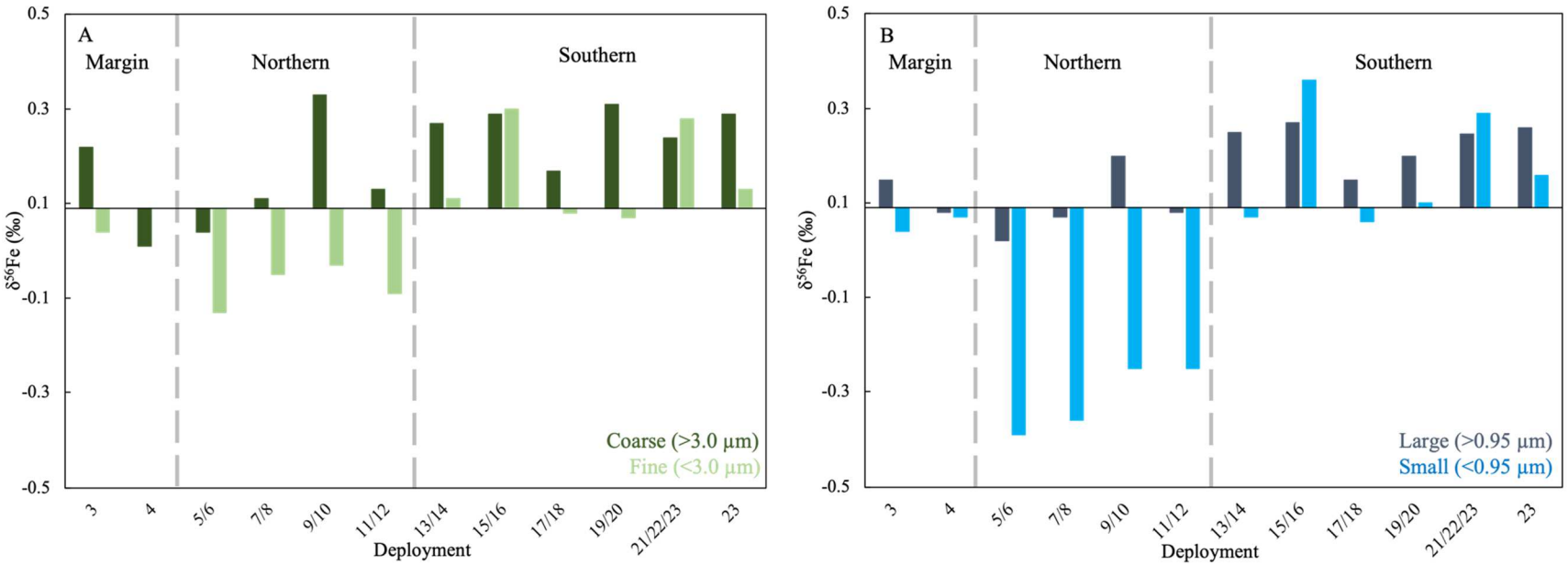

Figure 19. GP15 Coarse/Fine (3 µm) and Large/Small (0.95 µm) Total Aerosol δ^{56}Fe. A) coarse (dark green) and fine (light green) size-fractionated δ^{56}Fe using a threshold of 3 µm and **B)** large (dark blue) and small (light blue) size-fractionated δ^{56}Fe using a threshold of 0.95 µm. Note the x-axis intersects at the average crustal δ^{56}Fe value of +0.09‰. For clarity, error bars on δ^{56}Fe are not shown, but propagated errors are shown in Tables 6-7.

Table 1. GP15 Aerosol Soluble and Bulk Trace Metal Concentrations. Bulk Fe and Zn concentrations are calculated as the average of three discreet filters (with SD) while Cd was calculated using only two.

Deployment	Soluble Fe Conc. (pmol m^{-3})	Bulk Fe Conc. (pmol m^{-3})	Soluble Zn Conc. (pmol m^{-3})	Bulk Zn Conc. (pmol m^{-3})	Soluble Cd Conc. (pmol m^{-3})	Bulk Cd Conc. (pmol m^{-3})
1	3.7	35.6 ± 14.5	8.0	7.7 ± 2.0	0.02	0.06
3	0.9	13.0 ± 2.8	1.6	3.9 ± 1.0	0.01	0.01
5	7.0	152.4 ± 10.4	6.5	9.2 ± 2.5	0.04	0.05
7	4.2	146.3 ± 3.5	4.4	6.8 ± 1.1	0.06	0.25
9	1.9	108.7 ± 10.7	2.6	8.0 ± 2.0	0.01	0.03
11	1.3	37.0 ± 3.0	2.1	4.8 ± 0.7	0.01	0.03
13	0.5	48.3 ± 5.3	4.6	8.9 ± 1.0	0.02	0.04
15	0.3	42.5 ± 10.9	7.9	8.4 ± 2.5	0.10	0.10
17	0.4	22.0 ± 5.8	1.6	4.0 ± 0.7	0.03	0.09
19	0.7	38.9 ± 3.0	5.4	5.6 ± 2.8	0.02	0.01
21	0.9	40.8 ± 12.0	4.9	11.7 ± 5.6	0.01	0.02
23	n.d.	64.3 ± 17.1	n.d.	17.2 ± 3.3	n.d.	0.11

Table 2. GP15 Aerosol Trace Metal Solubility. Errors are standard deviation of solubilities calculated using three different bulk filter digests (two filters for Cd).

Deployment	Fe Solubility (%)	Zn Solubility (%)	Cd Solubility (%)
1	11.4 ± 4.0	109.0 ± 30.8	24.2 ± 12.8
3	6.8 ± 1.4	43.2 ± 11.4	64.2 ± 0.0
5	4.6 ± 0.3	73.2 ± 17.4	81.8 ± 27.0
7	2.9 ± 0.1	66.5 ± 10.5	25.9 ± 28.3
9	1.8 ± 0.2	34.2 ± 8.7	40.8 ± 3.9
11	3.6 ± 0.3	44.1 ± 6.0	32.0 ± 0.0
13	1.0 ± 0.1	51.8 ± 5.7	58.4 ± 15.1
15	0.8 ± 0.2	99.4 ± 25.6	99.6 ± 165.4
17	2.0 ± 0.5	39.6 ± 6.6	32.6 ± 6.3
19	1.9 ± 0.2	111.9 ± 44.6	175.7 ± 0.0
21	2.2 ± 0.7	49.4 ± 22.7	54.9 ± 4.8

Table 3. GP15 Aerosol Soluble and Bulk Trace Metal Isotope Ratios.

Deployment	Soluble $\delta^{56}Fe$ (‰)	Bulk $\delta^{56}Fe$ (‰)	Soluble $\delta^{66}Zn$ (‰)	Bulk $\delta^{66}Zn$ (‰)	Soluble $\delta^{114}Cd$ (‰)
1	+0.25 ± 0.05	+0.24 ± 0.05	-0.23 ± 0.03	+0.01 ± 0.03	-0.67 ± 0.59
3	-0.14 ± 0.05	+0.18 ± 0.05	+0.19 ± 0.05	-0.02 ± 0.03	n.d.
5	-0.45 ± 0.05	-0.03 ± 0.05	-0.01 ± 0.03	0.0 ± 0.03	-0.31 ± 0.14
7	-0.60 ± 0.05	+0.03 ± 0.05	+0.00 ± 0.03	-0.06 ± 0.03	-0.33 ± 0.15
9	-0.53 ± 0.06	+0.05 ± 0.05	-0.13 ± 0.03	-0.07 ± 0.03	-0.52 ± 0.43
11	-1.28 ± 0.06	+0.07 ± 0.05	-0.18 ± 0.03	-0.12 ± 0.13	-1.05 ± 0.40
13	-0.27 ± 0.13	+0.19 ± 0.05	-0.13 ± 0.03	-0.12 ± 0.07	-1.08 ± 0.26
15	-0.54 ± 0.09	+0.41 ± 0.06	-0.25 ± 0.03	-0.15 ± 0.03	-0.19 ± 0.12
17	-0.40 ± 0.09	+0.22 ± 0.05	+0.09 ± 0.03	-0.02 ± 0.05	-0.38 ± 0.19
19	-0.71 ± 0.08	+0.15 ± 0.05	-0.33 ± 0.03	-0.12 ±0.03	-0.07 ± 0.25
21	+0.02 ± 0.10	+0.32 ± 0.05	-0.35 ± 0.04	-0.29 ± 0.03	-1.91 ± 0.39
23	n.d.	+0.21 ± 0.05	n.d.	-0.13 ± 0.03	n.d.

Table 4. Fe Concentrations from Each Filter Stage for Size-fractionated GP15 Aerosols. Values are calculated as an average of USF and UGA measurements. Stage filters were corrected with the average of UGA and USF stage filter blank measurements, and backing filters were blank corrected with the average of UGA and USF backing filter blanks.

Deployment	Stage 1 (pmol m^{-3})	Stage 2 (pmol m^{-3})	Stage 3 (pmol m^{-3})	Stage 4 (pmol m^{-3})	Stage 5 (pmol m^{-3})	BF (pmol m^{-3})
3	1.4	2.4	1.6	1.2	1.1	49.4
4	0.9	1.8	2.2	4.6	3.6	3.2
5/6	10.4	35.4	26.8	20.8	9.8	13.9
7/8	7.0	30.1	24.6	18.5	6.1	5.9
9/10	6.2	18.5	15.3	15.5	8.3	11.1
11/12	3.0	5.6	5.2	4.7	2.8	5.8
13/14	19.6	10.9	4.9	4.3	2.8	9.3
15/16	3.6	2.8	1.6	1.3	0.9	3.2
17/18	2.7	5.6	3.3	2.8	1.6	5.6
19/20	2.5	4.6	2.6	2.0	1.2	5.2
21/22/23	4.6	4.6	2.9	2.4	1.7	10.0
23	4.6	3.8	3.0	3.2	2.1	7.5
Average	5.2	10.1	7.6	6.6	3.4	10.0

Table 5. GP15 δ^{56}Fe (‰) for Each Filter Stage for Size-fractionated Aerosol Samples. Isotope ratios from stage filters were blank corrected using measured stage filter blank ratios and backing filter isotope ratios were corrected with backing blank ratios. Both stage and backing filter. The last row is the weighted mean δ^{56}Fe for each stage along with its propagated error.

Deployment	Stage 1 (‰)	Stage 2 (‰)	Stage 3 (‰)	Stage 4 (‰)	Stage 5 (‰)	BF (‰)
3	+0.26 ± 0.05	+0.20 ± 0.05	+0.12 ± 0.05	-0.03 ± 0.05	0.00 ± 0.05	+0.04 ± 0.05
4	-0.29 ± 0.05	+0.15 ± 0.05	+0.09 ± 0.06	+0.12 ± 0.05	+0.09 ± 0.05	+0.05 ± 0.05
5/6	+0.06 ± 0.05	+0.03 ± 0.05	+0.02 ± 0.05	-0.01 ± 0.05	-0.57 ± 0.05	-0.26 ± 0.05
7/8	+0.19 ± 0.05	+0.09 ± 0.05	+0.04 ± 0.05	+0.03 ± 0.05	-0.40 ± 0.05	-0.33 ± 0.05
9/10	+0.16 ± 0.05	+0.38 ± 0.05	+0.15 ± 0.05	+0.05 ± 0.05	-0.26 ± 0.05	-0.24 ± 0.05
11/12	+0.12 ± 0.08	+0.13 ± 0.05	+0.11 ± 0.05	-0.02 ± 0.05	-0.50 ± 0.05	-0.13 ± 0.05
13/14	+0.31 ± 0.05	+0.21 ± 0.05	+0.20 ± 0.05	+0.13 ± 0.05	-0.05 ± 0.05	+0.11 ± 0.05
15/16	+0.29 ± 0.05	+0.29 ± 0.05	+0.30 ± 0.05	+0.12 ± 0.05	+0.28 ± 0.06	+0.38 ± 0.05
17/18	+0.21 ± 0.05	+0.15 ± 0.05	+0.08 ± 0.05	+0.16 ± 0.05	-0.13 ± 0.05	+0.11 ± 0.05
19/20	+0.19 ± 0.05	+0.37 ± 0.05	+0.08 ± 0.05	-0.04 ± 0.05	+0.10 ± 0.05	+0.10 ± 0.05
21/22/23	+0.21 ± 0.05	+0.28 ± 0.05	+0.30 ± 0.05	+0.21 ± 0.05	+0.11 ± 0.05	+0.32 ± 0.05
23	+0.23 ± 0.05	+0.36 ± 0.05	+0.19 ± 0.06	+0.25 ± 0.06	+0.14 ± 0.05	+0.17 ± 0.05
Weighted Mean	+0.21 ± 0.28	+0.18 ± 0.28	+0.09 ± 0.28	+0.05 ± 0.28	-0.28 ± 0.28	0.00 ± 0.28

Table 6. GP15 Aerosol Coarse (>3 µm) and Fine (<3 µm) Fe concentrations.

Deployment	Coarse Fraction	Fine Fraction
3	+0.22 ± 0.07‰	+0.04 ± 0.10‰
4	+0.01 ± 0.07‰	+0.09 ± 0.11‰
5/6	+0.04 ± 0.07‰	-0.13 ± 0.10‰
7/8	+0.11 ± 0.07‰	-0.05 ± 0.10‰
9/10	+0.33 ± 0.07‰	-0.03 ± 0.10‰
11/12	+0.13 ± 0.09‰	-0.09 ± 0.10‰
13/14	+0.27 ± 0.07‰	+0.11 ± 0.10‰
15/16	+0.29 ± 0.07‰	+0.30 ± 0.10‰
17/18	+0.17 ± 0.07‰	+0.08 ± 0.10‰
19/20	+0.31 ± 0.07‰	+0.07 ± 0.10‰
21/22/23	+0.24 ± 0.07‰	+0.28 ± 0.10‰
23	+0.13 ± 0.07‰	+0.13 ± 0.11‰

Table 7. GP15 aerosol Large (>0.95 µm) and Small (<0.95 µm) δ^{56}Fe.

Deployment	Large Fraction	Small Fraction
3	+0.15 ± 0.10‰	+0.04 ± 0.07‰
4	+0.08 ± 0.11‰	+0.07 ± 0.07‰
5/6	+0.02 ± 0.10‰	-0.39 ± 0.07‰
7/8	+0.07 ± 0.10‰	-0.36 ± 0.07‰
9/10	+0.20 ± 0.10‰	-0.25 ± 0.07‰
11/12	+0.08 ± 0.10‰	-0.25 ± 0.07‰
13/14	+0.25 ± 0.10‰	+0.07 ± 0.07‰
15/16	+0.27 ± 0.10‰	+0.36 ± 0.07‰
17/18	+0.15 ± 0.10‰	+0.06 ±0 .07‰
19/20	+0.20 ± 0.10‰	+0.10 ± 0.07‰
21/22/23	+0.25 ± 0.10‰	+0.29 ± 0.07‰
23	+0.26 ± 0.10‰	+0.16 ± 0.07‰

CHAPTER FOUR:
DISCUSSION

GP15 deployments are discussed in the context of Fe, Zn, and Cd isotope compositions together with elemental concentrations, solubilities, and enrichment factors, to assess the relative importance of possible sources supplying atmospheric TMs to the North Pacific Ocean. For Fe, two-component mixing models and global deposition modeling (CAM6-QFED) are used to estimate and verify the proportions of major Fe sources supplying Fe to each GP15 aerosol deployment. GP15 aerosol size-fractionated aerosol data is combined with data from Kurisu *et al.* (2021) to provide a more complete picture of size-fractionated North Pacific Fe aerosols and asses different binning methods used for coarse and fine size-fractionated Fe aerosols. Lastly, soluble aerosol δ^{56}Fe, δ^{66}Zn, and δ^{114}Cd are compared with GP15 surface seawater dissolved trace metal isotope compositions to assess any impact of aerosols on North Pacific surface isotope distributions.

4.1 Fe Source Apportionment to Northern, Southern, and Margin Deployments

4.1.1 Asian Anthropogenics and Dust Sources Supply Fe to the Northern Deployments

Bulk Fe concentrations for northern deployments between 52°N and 32°N are the highest among GP15 bulk deployments (37 to 152 pmol m^{-3}), consistent with previous observations in the North Pacific that show elevated Fe concentrations between 23°N and 52°N (Buck *et al.*, 2006 and 2013). Although concentrations observed during the CLIVAR-CO_2 P16 and fourth IOC cruises during the high dust season were orders of magnitude higher than GP15 during the low dust season, the overall trend between the cruises is similar (Buck *et al.*, 2006 2013). Buck *et al.*, (2013) attribute elevated Fe concentrations at these latitudes to the supply of aerosols originating from Asia (Fig. 4; Martin *et al.*, 2002). Aerosols originating

from the eastern coast of Asia are likely to be a combination of natural dust and anthropogenic Fe (Huang *et al.*, 2010). Soluble concentrations show a similar trend as bulk deployments and are also elevated due to the influence of Asian dust (1.3 to 7 pmol m^{-3}).

While aerosol Fe concentrations, solubilities, and EFs do not clearly pick out the presence of anthropogenic Fe in northern deployments, bulk, soluble, and size-fractionated $\delta^{56}Fe$ demonstrate the presence of anthropogenic Fe. Bulk $\delta^{56}Fe$ (-0.03 to +0.07‰) are light or crustal, near the minimum of the observed range of natural aerosols (-0.01‰), hinting at an anthropogenic influence at northern GP15 deployments (Fig. 13). The presence of anthropogenic Fe can be distinguished more clearly in the fine particles (-0.39 to -0.25‰), and even more clearly in the small particles compared to near-crustal signatures in larger particles (Fig. 19). Lastly, the presence of anthropogenic Fe at northern deployments is evident in soluble $\delta^{56}Fe$ (-1.28 to -0.45‰) and falls within the previous observed range of anthropogenic aerosols produced from combustion (-4.7 to -0.3‰; Kurisu *et al.*, 2016a; Kurisu *et al.*, 2016b; Conway *et al.*, 2019; Kurisu *et al.*, 2021). Overall, the data is supportive of northern deployments comprising of a mix of natural dust and anthropogenic Fe, with natural dust likely dominating the bulk phase and coarse/large particles, and anthropogenic Fe dominating the soluble phase and small particles. Elevated V (combustion tracer) and Ni and Zn EFs help confirm the presence of anthropogenic components in the northern deployments (Fig. 11), while Fe and Mn EFs are dominated by natural dust. As such, we conclude that Fe signatures at northern deployments are dominated by Asian dust that is a combination of natural Chinese loess and anthropogenic combustion Fe from the eastern coast of Asia. However, Alaskan dust sources can be ruled out as 3- and 10-day HYSPLITs show air masses did not interact with the Alaskan mainland.

In principle, a two-component mixing model can be used as a first order estimate of the proportions of two sources supplying Fe to a sample, in this case GP15 aerosols. It should be noted, however, there are some important caveats to this approach. First, it simplifies the calculation to only two sources when there potentially could be a mix of multiple sources with different $\delta^{56}Fe$ signatures, and so only works if two sources dominate. Second, it requires well constrained endmembers, and third, it assumes no further isotopic fractionation of source signatures with transport. Previous studies such as Conway *et al.* (2019)

and Kurisu *et al.* (2021) were able to constrain the sources of aerosol Fe to the North Atlantic and Northwest Pacific Oceans by modelling aerosols as a mixture of natural dust and anthropogenic combustion Fe, either by assuming wildfire to be negligible or to have the same isotopic signature as anthropogenic combustion.

These modelling approaches used data-informed fixed isotope endmember compositions; Conway *et al.* (2019) set natural and anthropogenic endmembers (including wildfire derived Fe) δ^{56}Fe at +0.09‰ and -1.60‰, respectively, while Kurisu *et al.*, (2021) used +0.09‰ for natural Fe and a range of North Pacific anthropogenic Fe (with an average of -4.3‰). North Atlantic soluble anthropogenic (including wildfire-derived) δ^{56}Fe was constrained at -1.60‰ based on the lightest observed value near industrial hotspots along the coast of North America and Europe and observations showing fossil fuel combustion and biomass burning can produce δ^{56}Fe as light as -1.60‰ (Conway *et al.*, 2019), while Kurisu used a lighter endmember based on their work on combustion source signatures and aerosol data (Kurisu *et al.*, 2021). Since δ^{56}Fe and EF relationships indicate the northern GP15 deployments are dominated by just two major sources, a two-component mixing model can also be used here as a first order estimate of aerosol source proportions.

Based on bulk and soluble δ^{56}Fe and EFs, the northern deployments were modelled as a mix of anthropogenic combustion and natural dust. Using the anthropogenic endmembers provided by Conway *et al.* (2019) and Kurisu *et al.* (2021) of -1.6‰ and -4.3‰, respectively, the range of relative proportions of natural and anthropogenic Fe calculated for GP15 bulk and soluble samples using two-component mixing are provided in Table 9 and 10, respectively. Northern deployment bulk Fe ranged from 0.5 to 7% anthropogenic combustion Fe and 93-99.5% natural dust Fe (Table 9). This is similar to, but slightly elevated from, the negligible anthropogenic Fe amount that Kurisu *et al.* (2021) calculated for bulk Northeast Pacific Aerosols, perhaps because their samples were dominated by crustal dust, something which could vary seasonally and with location. Using the same endmember range for combustion as for bulk aerosols (-1.6‰ and -4.3‰), northern deployment soluble Fe ranged from 12 to 81% anthropogenic and 19 to 88% natural Fe, reflecting the more-soluble nature of combustion Fe than dust Fe, and the advantage of using the soluble phase to identify and constrain anthropogenic Fe (Ito *et al.*, 2016; Ito *et al.*,

2019). A model output from Conway *et al.* (2019; Fig. 6) predicted that anthropogenic Fe contributes 20 to 40% of the annual soluble Fe in the North Pacific in the region of northern GP15 deployments. The proportion of soluble anthropogenic Fe calculated for GP15 northern deployments is broadly similar to this prediction (12-40%), and broadly similar to the 10-20% Fe calculated by the IMPACT model in Kurisu *et al.* (2021). Notably, however, one sample reaches as high as 81%, which could suggest the model is underestimating the significance of anthropogenic Fe in the North Pacific. Overall, though, the two-component mixing model suggests that Conway *et al.* (2019) modelling scenario is doing a good job of capturing broad source apportionment in the North Pacific based on the large isotopic range of anthropogenic Fe aerosols, at least in the low dust season. More field data from around the globe, specifically the North Pacific, is required to do a more in depth and accurate seasonal or annual comparison.

4.1.2 Which Atmospheric Sources Supply Fe to the Southern Deployments?

Bulk aerosol Fe concentrations of southern deployments (between 20°N and 20°S) are lower than northern deployments (20 to 64 pmol m^{-3}; Fig. 8) consistent with previous observations south of 20°N (Buck *et al.,* 2013); Asian dust is the dominant source to the North Pacific Ocean, and Buck *et al.* (2013) attribute a decrease in bulk Fe concentrations to the increased distance from the source of Asian dust as well as limited major dust sources south of 20°N (Ding *et al.*, 2001; Sec. 4.1). Additionally, most Asian dust particles are expected to be deposited closer to the source, thus, it would be expected that northern deployments have higher Fe deposition than southern deployments (Martin *et al.*, 2002; Kurisu *et al.*, 2021).

In contrast to the northern deployments, the bulk δ^{56}Fe of southern deployments are heavier than crustal (+0.19 to +0.41‰; Fig. 13), indicating Fe contributed by a source that is heavier than natural dust, perhaps from the coast of North America. Further, size-fractionated δ^{56}Fe do not show clear evidence of light δ^{56}Fe in small particles, suggesting that a) heavy Fe is present across different particle sizes, and b) there is no clear indication of anthropogenic combustion Fe. Additionally, and unlike northern deployments, V EFs are not elevated in the south, further indicating the lack of combustion sources in the south (Fig 11). Although Fe, Mn, and Al EFs are again all close to crustal in southern deployments (as in the northern),

there is a remarkable correlation between bulk δ^{56}Fe and Al EFs as well as elevated Fe and Mn EFs relative to northern deployments in these aerosols (Figs 11 and 14). All of these suggest the presence of a different non-dust and non-combustion source supplying heavy Fe (and Al and Mn) in the south.

A major question then, is: what is this source of heavy Fe? One option is wildfire, which has typically been assumed to supply isotopically light Fe in prior studies (Mead et al., 2014; Conway et al., 2019; Kurisu et al., 2021), and a second could be shipping emissions (also assumed to be light in prior modelling). In fact, GP15 sailed from September to November of 2018 which corresponds with the peak wildfire season on the North American west coast. General North Pacific atmospheric circulation and 10-day HYSPLIT models (Fig. S6) also indicate southern deployments were influenced by air masses that had traveled along or passed over the western coast of North America where NASA MODIS images show wildfires occurring (NASA Goddard Space Flight Center, 2022). By contrast, shipping emissions are expected to be less at the southern deployments than the northern (see Section 4.4.2 and 4.4.3). Therefore, the heavy Fe in southern bulk Fe aerosols could originate from a yet to be constrained wildfire source.

Previous studies have suggested that Fe taken up into plants is isotopically light (-1.6 to -0.3‰; Guelke and von Blankenburg 2007; Guelke-Stelling and von Blankenburg, 2012), and thus, wildfire was initially considered to produce isotopically light Fe (Mead et al., 2014; Conway et al., 2014). Recently, however, Hamilton *et al.* (2022) showed that up to 64% of the Fe found in aerosols derived from wildfires is derived from the pyro-convective entrainment of soils, echoing similar work showing that Fe and δ^{56}Fe released from biomass burning events are likely strongly influenced by soil particles (Kurisu and Takahashi *et al.*, 2019). While Kurisu and Takahashi could not definitively constrain the δ^{56}Fe signature of biomass due to a high combustion background in their aerosols, and assumed soil to be near-crustal, they did show that bulk and soluble aerosol δ^{56}Fe were up to 0.75‰ heavier during a distinct biomass burning event compared to immediately before and after (Kurisu and Takahashi et al., 2019). In fact, the global δ^{56}Fe of soils is variable, ranging from -0.5 to +0.95‰ (Johnson *et al.*, 2020), but soils such as laterites, andosols, and podzols, found along the west coast of North America exhibit δ^{56}Fe from +0.20 to +0.95‰ suggesting

they could be the source of heavy Fe to GP15 (Fantle and DePaolo, 2004, Emmanuel *et al.*, 2005, Wiederhold *et al.*, 2007, Thompson *et al.*, 2007, Akerman *et al.*, 2014; Johnson *et al.*, 2020).

Iron, Mn, Zn, and Ni and lithogenic metals such as Ti and Al are all found in soils or biomass, and as such, wildfires can be a large source of TMs in atmospheric aerosols (Marschner *et al.*, 1993; Cempel and Nikel 2005; Poonkothai and Vijayavathi 2012; Kurisu *et al.*, 2019; Perron *et al.*, 2020). For example, Kurisu and Takahashi (2019) also showed that TMs (e.g., Ti, Zn, Al, and Fe) were elevated during a biomass burning event compared to the combustion background and Schlosser *et al.* (2017) showed elements such as Fe, Al, Mn, and Zn to be elevated in Western US wildfire events, which they attributed to soil entrainment. Most recently, Perron *et al.* (2022) showed around two-fold increases in Fe, Mn, and Al aerosol loading from biomass burning in Western Australia. Although Fe EFs remain near-crustal in southern deployments, they are elevated compared to the north and are well correlated with Mn, Zn, Ni, and Al EFs, all showing a concurrent increase as Fe EFs increase (Fig. 11). This pattern is consistent with Fe, Mn, and Al being sourced to southern aerosols from North American wildfires entraining soil and plant debris. Furthermore, a range of studies have now shown that bulk biomass-burning derived aerosol Fe is likely to have low Fe solubilities, likely due to the proportion of entrained soil (2-6%; Paris *et al*., 2010; Winton *et al*., 2016; Kurisu and Takahashi 2019; Perron *et al*., 2022); this observation is consistent with the relatively-low solubilities of the GP15 southern deployments (1-2%), which indicate the heavy Fe is not especially soluble compared to combustion Fe.

Taken together, GP15 bulk δ^{56}Fe and EFs suggest that Fe derived from wildfires via pyro-convective entrainment of isotopically heavy Fe from soils found along the coast of North America can explain the heavy δ^{56}Fe in the bulk deployments of the southern portion of GP15. Thus, we suggest that for southern deployments, a mixture of Asian dust carrying natural dust, combustion Fe, and entrained wildfire Fe from North American airmasses are the sources of Fe to the bulk phase. We note that while a source of heavy Fe was not considered by Conway *et al.* (2019) in their Atlantic mixing models, there is in fact prior evidence for unexplained heavier-than-crustal Fe in atmospherics aerosols collected near to Portugal and Papa New Guinea (Conway *et al.*, 2019; Labutut *et al.*, 2014), and in particles collected over the eastern

North Pacific (Kurisu et al., 2021). Although northern and southern deployments show a clear difference in Fe sources to the bulk phase, southern deployments show soluble δ^{56}Fe that is similar to northern deployments (-0.27 to +0.02‰) As with northern deployments, this light Fe is likely indicative of anthropogenic combustion that continues to show up in the soluble phase more prominently due to elevated solubility. However, we do note that since the δ^{56}Fe signature of biomass has been shown to be light, and the biomass-derived Fe may be more soluble than soil-derived Fe, so the light isotopic signatures in the soluble phase of the southern deployments could be a sourced from a combination of anthropogenic combustion and biomass Fe from wildfires.

Overall, a range of evidence including δ^{56}Fe and EF relationships indicates there are more than two distinct sources supplying Fe to southern deployments in the bulk and possibly in the soluble phase. The GP15 δ^{56}Fe data, combined with literature data, also suggests that wildfire-derived Fe has a different isotopic signature to combustion Fe. As such, a two-component mixing model cannot be used to estimate source proportions, and a more complex three of four component model cannot be used without further constraints since this would require an additional parameter that directly scales with the Fe source. The implications of this are that globally, source attribution using δ^{56}Fe is likely to be more complex than previous studies have suggested, unless in regions where only two dominant sources can be isolated, or global deposition models are used to inform other variables.

4.1.3 Margin Deployments Fe

Deployment 1 was collected off the coast of Seattle east of the GP15 transect with airmasses coming from the west and circling the Gulf of Alaska, and deployment 3 was collected nearshore of Alaska with airmasses also circling the Gulf of Alaska. Margin deployment Fe concentrations are significantly lower than those of northern deployments, but similar to southern deployments (13 to 36 pmol m^{-3} Fig. 9). While deployment 1 is south of the northern boundary of 52°N previously observed by Buck *et al.* (2013) during the CLIVAR-CO2 P16 cruise, the lower concentrations of deployment 1 are a result of the deployment being located further downwind and further along the transport pathway from the source region of Asian

dust. Deployment 1 has an elevated soluble Fe concentration and may be the result of point source addition of a soluble anthropogenic Fe from the coast of North America. The bulk δ^{56}Fe of margin deployments are crustal (Fig. 12) and are near the upper UCC bound (+0.19‰; Beard *et al.*, 2003; Gong *et al.*, 2016) which indicate natural dust is dominant. Margin deployments soluble δ^{56}Fe is heavy at deployment 1 (+0.25‰) and is indicative of a source supplying isotopically heavy Fe, which could be wildfires. The soluble δ^{56}Fe of deployment 3 is light (-0.14‰) and suggests a relatively large contribution of anthropogenic or biomass Fe to the soluble phase. A lack of enrichment factor data for deployments 1 and 3 make it difficult to look more deeply into possible additional sources influencing the bulk and soluble Fe phases.

4.2 Fe Aerosol Addition to Surface Waters during GP15

Recently, Pinedo-Gonzalez *et al.* (2020) found elevated Fe concentrations in the surface of the North Pacific that they argued correlated with an increase in surface Pb concentrations during the high dust season (May) and attributed both to the input of anthropogenic aerosols. Here, we compare surface water sections for dissolved δ^{56}Fe from GP15 seawater samples (Sieber, pers. comm.) to aerosol δ^{56}Fe from GP15 aerosol deployments to observe if aerosols δ^{56}Fe signatures are influencing surface ocean δ^{56}Fe.

North Pacific surface seawater data from the top 50 m of GP15 was used for comparison, chosen to most closely match mixed layer depths during the cruise (up to 90 m but typically less than 50m; Rian *et al.*, in review) and seawater sample locations were matched to generate ranges for either northern (32 to 52°N) or Southern (20°S to 20°N) deployments, avoiding stations deemed to be influenced by Fe sources on the Alaskan Margin or Hawaii (based on Conway, pers. comm). This comparison generally shows the δ^{56}Fe in surface waters (+0.05 to +1.95‰) to be isotopically heavier than the soluble δ^{56}Fe from GP15 aerosols (-1.28 to +0.25‰). By deployments, northern stations surface seawater δ^{56}Fe ranges from +0.15 to +1.78‰, while soluble aerosols range from -1.28 to –0.45‰. Southern deployment surface seawater δ^{56}Fe ranges from -0.30 to +1.95‰, while soluble aerosols range from -0.71 to +0.02‰. Thus, unlike Pinedo-Gonzalez *et al.* (2020) we do not see clear evidence of dust or combustion aerosol Fe addition influencing the primary Fe isotopic signature of GP15 surface seawater, which is consistent with the very

low dissolved Fe concentrations measured in GP15 mixed layers across both aerosol deployment ranges (0.05-0.26 nmol kg-1). However, we do note that the lightest surface seawater values on both deployments correspond to the highest dissolved Fe concentrations (~0.23 nmol kg^{-1}) suggesting possible limited evidence of aerosol addition of Fe to surface waters in these locations.

A lack of light dissolved $\delta^{56}Fe$ from aerosol Fe addition to the surface is not surprising as it was also absent in the dusty North Atlantic (Conway and John, 2014). This is most likely due to internal cycling processes, such as uptake, organic complexation, and precipitation that add, remove, and fractionate Fe derived from aerosols in surface waters (Conway and John, 2014; König *et al.*, 2021). Any influence of Fe aerosols to the North Pacific may be even more diluted by fractionation of Fe in surface waters in the low dust season when Fe addition is low and Fe-limitation and uptake become more important. Further, if the signal of biomass-derived aerosol Fe is heavy, this would not drive surface seawater towards lower $\delta^{56}Fe$ values. Overall, more data and modelling are likely needed (e.g., König *et al.*, 2022) to determine whether the light Fe observed by Pinedo-Gonzalez *et al.* (2020) is from aerosols or from elsewhere.

4.3 Fe Trends Across North Pacific Ocean

Kurisu *et al.* (2021) published size-fractionated data from the Western and Central North Pacific that compliments the GP15 size-fractionated data. To provide a basin-scale description of Fe aerosols over the North Pacific, size-fractionated $\delta^{56}Fe$ data (coarse: >2.5 μm; fine: <2.5 μm) from Kurisu *et al.* (2021) is shown together with GP15 size-fractionated $\delta^{56}Fe$ data (coarse: >3.0 μm; fine: <3.0 μm) in Figure 20. Taken together, total, coarse and, fine size-fraction $\delta^{56}Fe$ from both studies display similar latitudinal and longitudinal trends throughout the North Pacific which are consistent with the atmospheric circulation of the North Pacific. The lightest bulk aerosols are seen closest to Asia (-0.91 to -0.07‰) and continue to be the among the lightest eastward throughout the Asian dust band (20°N and 52°N), in both datasets from Kurisu *et al.* (2021; (-0.91 to +0.39‰) and GP15 (-0.06 to +0.08‰; Fig. 20). The same trend holds for the coarse and fine fractions within the Asian dust band, with $\delta^{56}Fe$ being lightest near the coast of Asia and becoming heavier farther east: coarse size-fractionated $\delta^{56}Fe$ near Asia are (-0.24 to +0.37‰) and (+0.04

to +0.33‰) towards North America, and fine fraction δ^{56}Fe is (-2.16 to -0.1‰) near Asia and (-0.13 to -0.03‰) farther east at GP15 deployments. Fine fraction δ^{56}Fe is lighter than the coarse fraction throughout the Asian dust band of North Pacific, indicating the consistent presence of anthropogenic aerosols. However, GP15 deployments show slightly heavier δ^{56}Fe than data from Kurisu *et al.* (2021), perhaps due to the slight difference in binning, a different mix of dust sources in Asia during different seasons, or dilution of Asian dust with Alaskan or other possible Fe sources due east.

South of the Asian dust band, total, coarse, and fine δ^{56}Fe all become heavier (+0.09 to +0.42) as air masses are deflected to the south along the coast of North America and west across the open ocean, and each fraction's δ^{56}Fe ranges continue to increase as air masses travel back towards Asia along the equator. Furthermore, the fractionation between coarse and fine particles is lost. Once air masses reach the east and take a southward trajectory along North America, they pick up additional Fe along the coast from sources such as Alaskan and American dust, wildfires, and anthropogenic activity, and the dominance of Asian (dust and combustion) is lessened. Size-fractionated data from Kurisu *et al.* (2021) shows that the elevated δ^{56}Fe values observed in the south of GP15 are carried eastward across the equator back towards Asia suggesting a large-scale influence of wildfire derived Fe to the region. Overall, the size-fractionated δ^{56}Fe data Kurisu *et al.* (2021) accentuates the findings of Asian dust to the northern deployments and North American and Asian dust to the southern deployments. While all phases of the size fractionated δ^{56}Fe show the lightest isotopes within Asian dust (northern deployments) as the result of anthropogenic Fe addition, they are much heavier at the southern deployments as the result of wildfire (soil) Fe addition.

4.4 Fe Deposition Models for Source Attribution

Based on observational GP15 data, we suggest Asian dust (which is a combination of crustal and anthropogenic Fe) dominates northern deployments. Southern deployments are a mixture of Asian dust and North American crustal, wildfire, and anthropogenic sources influence the South. As noted earlier (Section 4.1.1 and 4.1.2), simple isotopic mixing models lack suitable constraints to test these assertions or constrain multiple sources. However, global Fe deposition models provide us with further opportunity to investigate

aerosol Fe sources and test assertions – specifically whether the heavy endmember in the bulk phase is indeed wildfire, and whether our interpretations of sources to GP15 can be validated.

Model-predicted soluble and total Fe concentrations in air for grid cells from the atmospheric dust deposition CAM6 model within the National Center for Atmospheric Research Community Earth System Model (CESM), using the Quick Fire Emissions Dataset (QFED) were produced by collaborators (Hamilton and Mahowald, pers. comm.), and matched to the latitude, longitude, date, and time of the GP15 aerosol deployments (Scanza *et al.*, 2018; Hamilton *et al.*, 2020a; Hamilton *et al.*, 2020b). As well as providing simulated total and soluble aerosol Fe concentrations to a grid cell, the CAM6 Fe deposition model with QFED allows separation of both soluble and total Fe into distinct sources of natural, wildfire, and anthropogenic Fe (coal, oil, biomass, fossil fuel combustion, and smelting Fe; Scanza *et al.*, 2018; Hamilton *et al.*, 2019 Hamilton *et al.*, 2020a; Rathod *et al.*, 2020). Then, by assigning a fixed Fe isotopic endmember to each source in the model output, the weighted-average Fe isotopic composition of the modeled aerosol in each grid cell can be calculated (as done for CAM4 by Conway *et al.*, 2019) for comparison with GP15 aerosol isotopic compositions. The model match or mismatch can then help inform understanding of the Fe sources in GP15 aerosols, as well as informing where models may need refinement.

In order to predict model-derived δ^{56}Fe isotopic compositions, suitable δ^{56}Fe endmembers for Fe sources must be chosen. Conway *et al.* (2019) used endmembers for wildfire, anthropogenic, and dust sources in the Atlantic (Tables 11 and 12), but these likely require refinement or updating to include sources which are likely different in the Pacific (e.g., heavy wildfire and shipping). For example, Conway *et al.* (2019) assigned the wildfire endmember for the CAM4 output to -1.60‰ due to the preferential uptake of light Fe by biomass (and for simplicity to match combustion), but as I have shown in Section 4.1.2, wildfire Fe to the Pacific is heavy and dominated by soils. Relevant to GP15, δ^{56}Fe in soils along the west coast of North America where wildfires are present from July to November have been observed to range from +0.25 to +0.95‰, revealing that the wildfire endmember used in Conway *et al.* (2019) needs to be updated to better represent the fire contribution over the North Pacific.

Shipping could be an additional source of heavy Fe to aerosols as since gasoline and coarse-combustion particles are +0.35‰ (Kurisu *et al.*, 2016) and the δ^{56}Fe signature of oil fly ash standards (from burning fuel oil range from +0.1 to +0.5‰ (Mead et al., 2014). As such, if heavy fuel oil is burnt by ships with less effective fractionation than from transport of distal combustion (e.g., if coarse and fine particles make it to aerosol collection from shipping), then this heavy signal could be transferred. One thing is clear, however, the North Pacific δ^{56}Fe shows a heavy wildfire Fe source that was not included in previous modelling. Our size-fractionated data for southern GP15 deployments shows that this heavy wildfire Fe is present over the full range of particle sizes from <0.5 to >8 µm, not just coarse particles (Figs 17-18), inconsistent with the suggestion of the heavy Fe coming simply from long distance (or shipping-derived) coarse 'heavy' combustion particles.

Here, we carried out a range of simulations using CAM6 QFED model deposition output matched to GP15 bulk and soluble aerosol deployments, changing model endmembers to test various scenarios by how well model data matched observations (Figs 22-23; Tables 10-11) via sum of the squares of misfits (Table 12). The first scenarios (termed QFED-B1 and QFED-S1 for bulk and soluble respectively) were set with endmembers to match the endmembers chosen by Conway *et al*. (2019) for the Atlantic but used in their global CAM4 isotope-informed deposition modelling (see Tables 10-11 for values). Later scenarios kept the natural dust δ^{56}Fe endmember the same (at +0.09‰), and varied the fire, anthropogenic, and/or shipping δ^{56}Fe endmembers (Tables 10-11).

4.4.1 QFED-B1 and QFED-S1: Original Model and GP15 Observations

The first aspect of observation-model comparison was to compare the modelled bulk and soluble Fe 'concentrations' from CAM6-QFED with their respective GP15 Fe concentrations. Overall, the model overestimates both bulk and soluble concentrations compared to observations (Fig. 21), with the bulk showing a better match (~50% of points are similar) than the soluble (most points are overestimated by the model). This finding suggests the model has too high a flux of both soluble and total Fe aerosol to the region

during the low dust season, which may have a significant impact on how well the model can capture the predicted isotope ratios, especially if one or more source in particular is over-represented.

When comparing the bulk and soluble GP15 δ^{56}Fe observations with QFED-B1 and QFED-S1, the model generally predicts lighter isotope compositions than observed (Figs 22 and 23). The mismatch between model and observational δ^{56}Fe is the greatest for the southern deployments in the bulk phase while the margin deployments have the worst fit in the soluble phase. Overall, GP15 bulk and soluble δ^{56}Fe finds wildfires are a heavy source of Fe to aerosols, as such, the difference between the model and observations also indicate that a heavy wildfire endmember is needed. The fit between model and observational bulk and soluble data is quantified by a sum of the squares of misfit calculation (Table 12). QFED-1 has a bulk and soluble δ^{56}Fe sum of squares of misfit with GP15 observations of 3.92 and 7.53 respectively that will be compared with subsequent bulk and soluble δ^{56}Fe model scenarios. The sum of squares of misfit calculation was carried out by squaring the difference between model and GP15 δ^{56}Fe for each deployment and then summing the squared values of all deployments.

4.4.2 QFED Updated Isotope Endmember Simulations

We then carried out four more CAM6-QFED simulation scenarios to investigate if this model-observation mismatch of bulk and soluble δ^{56}Fe could be explained and verify a heavy wildfire Fe endmember, or if it could be improved by reasonable changes to other endmembers based on the findings of GP15 (Figs 22-24).

4.4.2.1 Adding a Heavy Endmember: Wildfire vs. Shipping?

The combined North Pacific bulk δ^{56}Fe dataset mandates a need for a heavy aerosol Fe source. There are two plausible options for a heavy source to the bulk phase, wildfire-derived or shipping-derived Fe. In the original scenario QFED-B1, both sources are set to -1.6‰ (Section 4.4.1). Here, we tested the impact of changing these endmembers in several ways: QFED-B2 (heavy Fe from wildfire), QFED-B3 (heavy Fe from shipping), QFED-B4 (heavy Fe from both). Scenarios QFED-B2, B3, and B4 thus allow us

to investigate the possible influence of a heavy wildfire and/or shipping endmember(s) on model-predicted North Pacific bulk aerosol δ^{56}Fe (Fig. 22). To do this, since shipping is not separated from other combustion in the CAM6 QFED output, a separate model run was conducted without shipping (Hamilton, pers. comm), and then shipping calculated as the difference between combustion Fe in the two runs. An updated Fe wildfire endmember of +0.70‰ was chosen based on GP15 Fe data, possible soil sources in N. America, and recent studies signifying the importance of wildfires (discussed in Section 4.1.2) for QFED-B2 (Table 10; Fig. 22B). The shipping endmember was updated to +0.35‰ for the QFED-B3 simulation based on expectation of the isotopic signature of coarse anthropogenic particle signatures as discussed above (Table 10; Fig. 22C). The QFED-B4 simulation has wildfire Fe set to +0.70‰ and shipping Fe set to +0.35‰ (Fig. 22D).

Each simulation, QFED-B2, B3, and B4, is a significant improvement from the original QFED-B1 simulation (Table 12; Fig. 22). However, while QFED-B2 and B3 both improve the sum of the squares of misfits to a similar degree, a heavy wildfire endmember (+0.70‰) drastically improves the fit for southern deployments but only nominally for the northern and margin deployments, and vice versa, a heavy shipping endmember (+0.35‰) leads to great improvement for northern and margin deployments but has little effect on the fit of southern deployments (Table 10; Fig. 22). As the model estimates, this is a result of there being more shipping Fe in North and more wildfire Fe in the South and can also be corroborated by elevated V EFs as the result of oil combustion in the North (Marsay *et al.*, 2021). Thus, both independently updated endmember simulations only improve the fit for certain northern, margin, or southern deployment types; as such, these simulations suggest both sources must be heavy to best explain North Pacific data. This assumption is borne out by QFED-B4 providing the best fit among simulations (Fig. 22; Table 12).

QFED-B4 provides the best fit from all four the simulations, but we note the model still predicts lighter δ^{56}Fe than observations; this could reflect our original conclusion that combustion Fe is being overestimated in the model, or it could suggest that the endmember choices for fire and shipping are too light (Fig. 23). To address this question, a final QFED-B5 simulation was conducted to produce the best fit by increasing the wildfire and shipping endmembers to values that obtain the minimum sum of the square

of misfits (+2.00‰ and +2.50‰). However, both these endmembers are unrealistic and heavier than any natural or anthropogenic Fe source to aerosols (Table 10; Table 12). Thus, we conclude that the misfit between model and observations is likely driven by bulk anthropogenic combustion Fe concentrations being overestimated, causing the contribution of anthropogenic Fe to be too large. The model may also not be accurately capturing proportions between sources.

Overall, the model-data comparison reinforces our findings that wildfire is the heavy Fe source to GP15 aerosols, but also suggests an additional source of heavy Fe that appears to be shipping. The fit improves most in the northern and southern deployments, consistent with our conclusions of dust and combustion dominating the northern GP15 deployments and a mix of sources contributing to southern deployments (Section 4.4.2). Furthermore, it shows the need for an additional source of heavy Fe from shipping, especially at stations within the Asian dust band that are not affected by wildfires.

4.4.2.2 Insights from Bulk $\delta^{56}Fe$ Comparison for a Soluble $\delta^{56}Fe$ Comparison

The CAM6-QFED simulations also output soluble Fe concentrations. Assuming no isotopic fractionation during dissolution (Conway *et al*., 2019), we can compare our findings from the bulk aerosol data-model comparisons with soluble comparisons. As commented previously, QFED-S1 shows that the model is predicting soluble aerosol δ^{56}Fe signatures which are too light (Fig. 24A). QFED-S2 was thus parametrized based on the QFED-B4 wildfire (+0.70‰) and shipping (+0.35‰) endmembers that provide the best (and most realistic) fit for bulk aerosols (Fig 24B). QFED-S2 improves the comparison, providing a much better fit than the original QFED-S1 (Fig. 24A; Table 12); however, now, the model predicts soluble δ^{56}Fe that is overall heavier than observations (Fig. 23). This suggests that the same endmember signatures cannot explain the soluble Fe phase (or that wildfire or shipping Fe solubility is overestimated). However, as we have discussed in Section 4.4.2, there may be an 'effective' isotopic fractionation of wildfire-derived Fe if plant Fe is more soluble than soil Fe, and plant Fe is isotopically light. Varying the fire endmembers within realistic ranges could help address if this could be the case. For shipping, although the size-

fractionated GP15 data seem inconsistent with shipping having different signatures in each phase, it is also worth investigating if lighter soluble Fe could improve fits.

The wildfire and shipping endmembers were thus independently altered to lower values in QFED-S3 and S4, respectively, to observe if one source might provide light Fe to the soluble phase (Table 11; Fig. 24). QFED-S3 was updated to a biomass Fe signature of -1.60‰ (Table 11). This change may improve the model-observation match with GP15 southern deployments (Fig 24), although they are now too light. However, because of the negligible contribution of wildfires to the northern and margin deployments, the fit shows little improvement to these deployments with the QFED-S3 simulation. Reflective of the fact that shipping is more important to the North than the South in the model, the QFED-S4 simulation with a light shipping endmember (-1.60‰) only significantly improves the fits for the northern and margin deployments, while four out of five of the southern deployments remain too heavy and the margin deployments are much too light in the QFED-S4 simulation (Fig. 24). Like the bulk comparison δ^{56}Fe both model iterations (QFED-S3 and S4) indicate that the soluble shipping endmember is important to the northern deployments and the soluble wildfire shipping endmember is important to the southern deployments.

Thus, to improve the model-observation match, an endmember that significantly influences each deployment must be lowered to improve the fit between the model and observations, or the model source breakdown is incorrect. The remaining endmember that could be lighter and improve the fit is the anthropogenic endmember, since the δ^{56}Fe of natural Fe is very well constrained. While such a lighter endmember cannot work in the bulk phase (Fig. 22), we know that anthropogenic combustion shows isotopic fractionation between particle sizes, and it may be that the lighter, smaller particles are more soluble than the overall combustion aerosol. As such, the soluble signature could be lighter than the bulk. To test this, a QFED-SA simulation was carried out with a lighter anthropogenic source endmember (-4.30‰) based on Kurisu *et al.* (2021; Table 11; Fig. 23). In fact, the QFED-SA simulation does provide the best overall fit between model predictions because it improves the fit among all deployment types (Fig. 23; Table 11), but we acknowledge that this value may be representative of the source signature while the -

1.60‰ used by Conway *et al.* 2019 is a more accurate value for anthropogenic aerosols over the open ocean. Thus, while more work is clearly needed to constrain aerosol $\delta^{56}Fe$ endmembers in order to conclusively address some of these questions, our final soluble simulation is consistent with the model broadly capturing sources in the North Pacific when both soluble anthropogenic Fe and soluble wildfire Fe are both lighter than in their respective bulk phase (Table 11; Table 12; Fig. 23). Alternatively, we note the model estimates wildfire Fe solubilities from 11-73%, but that recent work found coarse wildfire Fe to be relatively insoluble (2-6%; discussed in Section 4.4.2; Hamilton *et al.*, 2019). Therefore, while this is outside the scope of this thesis, if the CAM6-QFED model could have parameters adjusted to fix the aspects which result in overestimation of wildfire Fe solubility, then this could also result in a lower contribution of the heavy wildfire-derived Fe component that would provide a better fit to observations and reduce/eliminate the need for different endmembers in bulk and soluble phases.

4.5 Atmospheric Sources of Zn to GP15 and Their Impact on Surface Seawater

Although bulk Zn aerosol data for the North Pacific are very scarce, but one previous study along 160°W from the summer reported a mean concentration of 90 pmol m^{-3} (Furutani et al., 2010), almost an order of magnitude higher than the bulk Zn concentrations on GP15 (3.9 to 17.2 pmol m^{-3}). This limited comparison suggests that that bulk Zn broadly follows Fe, with an increase in the high dust season and decrease in the low dust season; as such this pattern is likely driven by changes to the amount of Asian dust over the basin (Ding *et al.*, 2001; Buck *et al.*, 2013). In terms of natural or anthropogenic sources in Asian dust, Zn solubilities are very high along the GP15 section (34-112%) and show similar variation as Zn aerosols from the coast of Taiwan that ranged from 1 to 85% (Hsu *et al.*, 2005), indicative of a dominant contribution of highly soluble anthropogenic Zn. Elevated Zn EFs (32 to 693) and isotopically light $\delta^{66}Zn$ throughout the transect support this suggestion, indicating that the whole GP15 section is dominated by non-crustal Zn (expected to be +0.20 to +0.34‰; Little *et al.*, 2014).

As with Fe, there are distinctions between the northern and southern GP15 deployments that may provide insight into aerosol Zn sources. The southern deployments have the highest EFs (systematically

>200), and also show strong correlations with Fe, Mn, and Ni EFs (Fig. 12). In contrast, the northern deployments have Zn EFs <200. There is no clear dichotomy in Zn concentrations, Zn solubility, or $\delta^{66}Zn$ between northern and southern deployments. However, bulk and soluble $\delta^{66}Zn$ generally decrease, Zn EFs increase, and Zn solubilities decrease in the south. These patterns do suggest a strong anthropogenic Zn signal in Asian Dust as well as a relatively small natural Zn component. However, the extremely high Zn EFs in the South strongly suggest that, like Fe, additional Zn is picked up as air masses are carried along the North American coast.

Based on our analysis of Fe sources (Section 4.1.1 and 4.1.2), possible Zn sources along the coast of western North America might be expected to be wildfires and/or anthropogenic pollution. The question then arises as to whether the isotopically light aerosol Zn is sourced from anthropogenic combustion/activity, or wildfires, or both. Limited literature data exist to establish a wildfire endmember for $\delta^{66}Zn$. Plants preferentially take up light Zn (-0.56 to -0.26‰), while pyro-convective entrainment of soil Zn would be expected to add a heavy isotopic signature (+0.2 to +0.5‰; Weiss *et al.*, 2007; Jouvin *et al.*, 2012; Smolder *et al.*, 2013; Caldelas and Weiss 2017). As with Fe, we would expect wildfire Zn to be a mixture of soil and plant Zn, with studies of biomass burning showing evidence of aerosol to be enriched in Zn, possibly attributed to soil entrainment (Schlosser et al., 2017; Kurisu and Takashi, 2019). However, given that the Zn content of soil is typically much lower than Fe (Soil has ~66-55,000x less Zn than Fe; Bodek *et al.*, 1988; Lindsay, 1972), the different ratio of plant to soil Zn (plants have ~2-6x less Zn than Fe; Timperly *et al.* (1973) likely leads to a wildfire endmember $\delta^{66}Zn$ that is more strongly dominated by plants and thus isotopically light. It is also possible that North American anthropogenic Zn could be a source of light Zn and elevated Zn EFs, but the EFs of apparent wildfire soil tracers (Al, Mn, and Fe) are well correlated with Zn EFs in southern deployments and thus suggest the decrease in bulk and soluble $\delta^{66}Zn$ is due to the addition of wildfire-sourced Zn (Figs. 11 and 12; Perron *et al.*, 2020). Additionally, we note that the southern deployments generally show lighter $\delta^{66}Zn$ and larger $\Delta\delta^{66}Zn_{bulk\text{-}soluble}$ (the difference between bulk and soluble $\delta^{66}Zn$) than in the North, supporting a different Zn source in the South and perhaps further indication of soil-derived Zn in the bulk phase and plant-derived Zn in the soluble phase (Fig. 13). However,

we also note that Perron *et al.* (2022) showed that biomass burning also picked up V and Pb in Western Australia, which they concluded came from contaminated soil. As such, it is also possible that light Zn comes from anthropogenic contributions to soils and wildfire in our study, although V EFs show no enrichment in the South (Fig. 15). While we suggest the decrease in δ^{66}Zn and increase in EFs in the southern deployments are a result of the addition of wildfire and anthropogenic Zn, we do note that Marsay *et al.* 2021 attributed the increase of EFs to the southern deployments as a result of a winnowing effect of coarse mineral dust rather than addition of wildfire and anthropogenic aerosols. However, we do not observe a decrease in Zn concentrations as a result of mineral dust winnowing and size-fractionated Fe does not show a preferential loss or absence of coarse particles. Overall, we suggest that the concomitant increase of EFs of Ni and Zn with Al, Fe, and Mn in GP15 aerosols, coupled to the decrease in soluble δ^{66}Zn in southern deployments is driven by the addition of light Zn aerosol relating to wildfires and anthropogenic sources along the coast of North America (Gioia *et al.*, 2008).

In North Pacific surface seawater, δ^{66}Zn have been shown to be dynamic, with isotopically light anomalies reported in the shallow subsurface due to regeneration and/or scavenging events (Vance *et al.*, (2019); Sieber *et al.*, in prep.). As such, we only compare GP15 aerosol δ^{66}Zn with the very-surface (2 m tow-fish) dissolved δ^{66}Zn here, with seawater data from Sieber *et al.* (in prep.) again matched to aerosol deployment latitudes. Soluble aerosol δ^{66}Zn is lighter (-0.29 to +0.01‰) from all GP15 deployments than surface dissolved δ^{66}Zn (+0.20 to +0.60‰; Fig. A8), and so it appears that Zn aerosols do not directly impart their isotopic signature to the surface of the North Pacific Ocean, at least during the low dust season. This may reflect the fact that bulk deposition of Zn to non-ITCZ samples (12 ± 7 nmol m^{-2} day^{-1}) are much lower than Fe (96 ± 68 nmol m^{-2} day^{-1}; Marsay et al., 2021), while surface dissolved Zn concentrations (0.02-0.75 nmol kg^{-1}) are similar to or much higher than surface dissolved Fe concentrations (0.05-0.26 nmol kg^{-}) in the region (Sieber, pers. comm.); as such, upwelling supply likely dominates the dissolved Zn cycle. Overall, as with δ^{56}Fe aerosols, there is no clear impact of aerosol Zn on surface dissolved δ^{66}Zn along GP15, although aerosol input of isotopically light Zn could contribute to the low upper ocean δ^{66}Zn as has been suggested for the Atlantic (Lemaitre et al., 2021). Conclusions about aerosol Zn input for GP15

differ from that of Liao *et al.* (2021) who used a mass balance to argue that sinking particles in the South China Sea were composed of up to 64% anthropogenic Zn during April to October and November to March. This discrepancy is likely due to the proximity of the site studied by Liao *et al.* (2021) to sources of anthropogenic Zn, as particles are more likely to be deposited near the source rather than the open ocean. Furthermore, Liao *et al.* (2021) were studying the particulate phase in which an anthropogenic source signature might be better conserved than in surface waters.

4.6 Atmospheric Sources of Cd to GP15 and Their Impact on Surface Seawater

Bulk and soluble Cd concentrations are variable along the transect, with no obvious trends (Fig. 9). Consistent with this, there are no clear divisions between northern and southern deployments, nor a distinguishable influence of Asian dust in the northern deployments. Our GP15 bulk Cd concentrations compare well to those reported for anthropogenically-influenced East Asian air masses during the spring from Patterson and Duce (1990), which also showed great variability (0.01 to 0.53 pmol m^{-3}). However, those measurements by Patterson and Duce (1990) were from aerosols collected during the high dust season. Thus, in contrast to Fe and Zn, Cd aerosol deposition may be relatively constant throughout the year rather than strongly peaking during the spring and waning during the fall.

Soluble δ^{114}Cd exhibit significantly lower than crustal values (-1.91 to -0.07; Fig. 14) and together with elevated Cd EFs (263 to 10775; Fig. 25) throughout the entirety of the transect indicate that anthropogenic combustion Cd dominates aerosols in the North Pacific (Nriagu and Pacyna, 1988; Pacyna and Pacyna, 2001; Pacyna *et al.*, 2009). However, GP15 aerosol δ^{114}Cd show no obvious relationship with GP15 aerosol EFs of Fe, Zn, Mn, Ni, Pb, and Al, elements that also reflect variable contributions from anthropogenic activities. In the North Pacific, this is likely because other metals are sourced from a mixture of anthropogenic combustion, wildfire/soil and crustal dust, while Cd almost originates from anthropogenic combustion because Cd is simply so low in natural dust (average: 200 ng g^{-1}) and soil (average: 360 ng g^{-1}; Kubier *et al.*, 2019). While atmospheric δ^{114}Cd data is very limited, we can compare GP15 data with aerosol δ^{114}Cd data from the tropical Atlantic (-0.19 to +0.19‰; Bridgestock *et al.*, 2017). Similar to Zn

aerosols, Cd aerosols are isotopically heavier in the Atlantic and lighter in the Pacific (Little *et al.* and others; Section 4.5). This difference is most likely due to dominant anthropogenic supply of Cd in the Pacific from large anthropogenic hotspots on the coasts of East Asia and the west coast of North America compared to the tropical Atlantic where the large Saharan Dust plumes dominate (Kandler and Scheuvens, 2019; Ginoux *et al.*, 2012).

Unlike for surface δ^{56}Fe and δ^{66}Zn (Section 4.2 and 4.5), Cd aerosols may potentially affect surface water dissolved δ^{114}Cd in the North Pacific, principally because surface dissolved Cd concentrations (top 50 m) are vanishingly low in the gyres of the region (Fig. A8). For northern deployments, dissolved Cd concentrations from the top 50m are 1-424 pmol kg^{-1} with δ^{114}Cd of +0.7 to +1.2‰ (Sieber *et al.*, in review), indicative of the dominance of biological uptake driving surface Cd isotope compositions (Sieber *et al.*, in review). At southern deployments, however, dissolved Cd is even lower (0.4 to 10 pmol kg^{-1}), and δ^{114}Cd range from -0.1 to +0.8‰ (Sieber *et al.*, in review), suggesting a possible impact of Cd aerosol to these locations. Previously, George *et al.* (2019) and Sieber *et al.* (2019) suggested that the addition of anthropogenic Cd may be causing lower than expected δ^{114}Cd in Cd-depleted surface waters in the Southwest Pacific, and a similar effect can be invoked here; for GP15. Sieber *et al.* (in review) argued that surface waters in gyres along the transect deviate from an open system model and have lower than expected δ^{114}Cd. As soluble δ^{114}Cd aerosols are dominated by anthropogenic Cd with values ranging from -1.91 to -0.07‰, the addition of even a small amount of anthropogenic Cd aerosols could explain the lower-than-expected δ^{114}Cd observed in surface waters in the North Pacific (Sieber *et al.*, in review). The apparent lack of strong seasonality in aerosol Cd concentrations could mean that a consistent source of light, anthropogenic Cd helps set surface δ^{114}Cd in the North Pacific gyres.

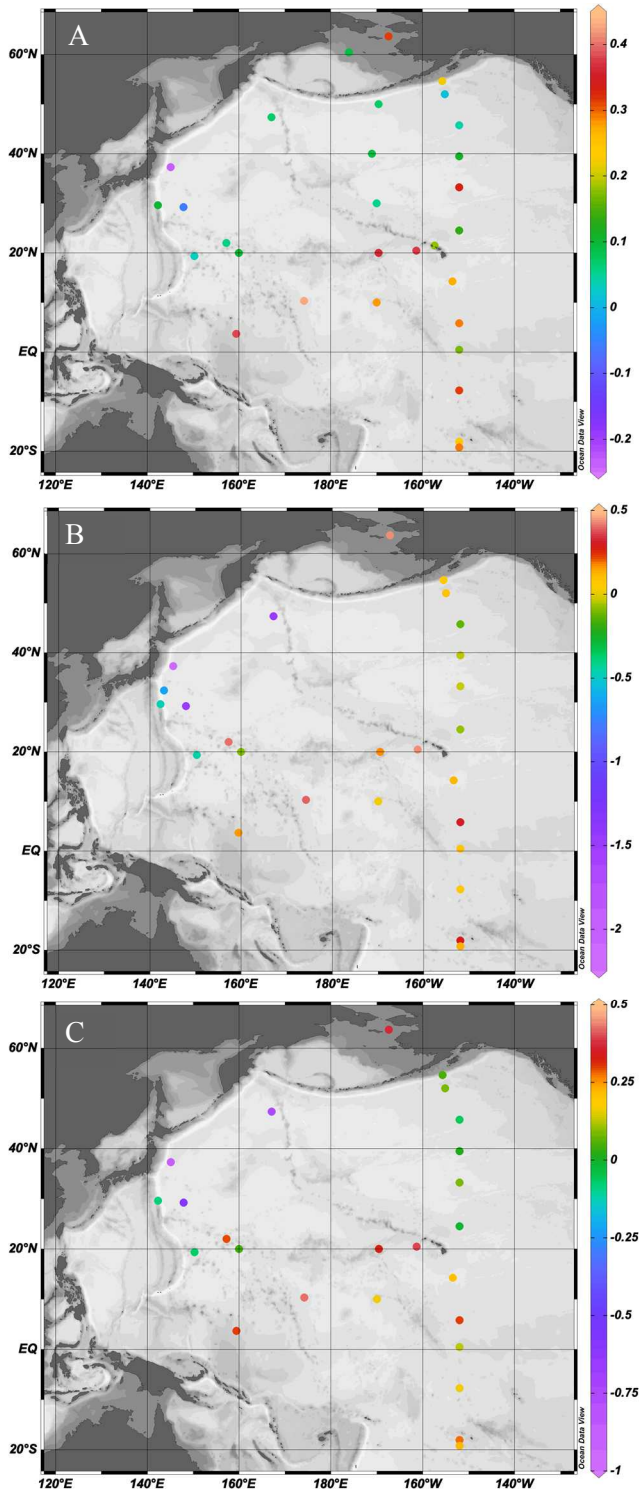

Figure 20. North Pacific Size-fractionated Aerosol δ^{56}Fe Compilation (GP15 and Kurisu *et al.* (2021)). Comparison of A) coarse size fraction δ^{56}Fe from GP15 (>3.0 µm) and Kurisu *et al.* (2021) (>2.5 µm), **B) fine size fraction δ^{56}Fe from** GP15 (<3.0 µm) and Kurisu *et al.* (2021) (<2.5 µm) and **C)**) total δ^{56}Fe from GP15 and Kurisu *et al.* (2021.

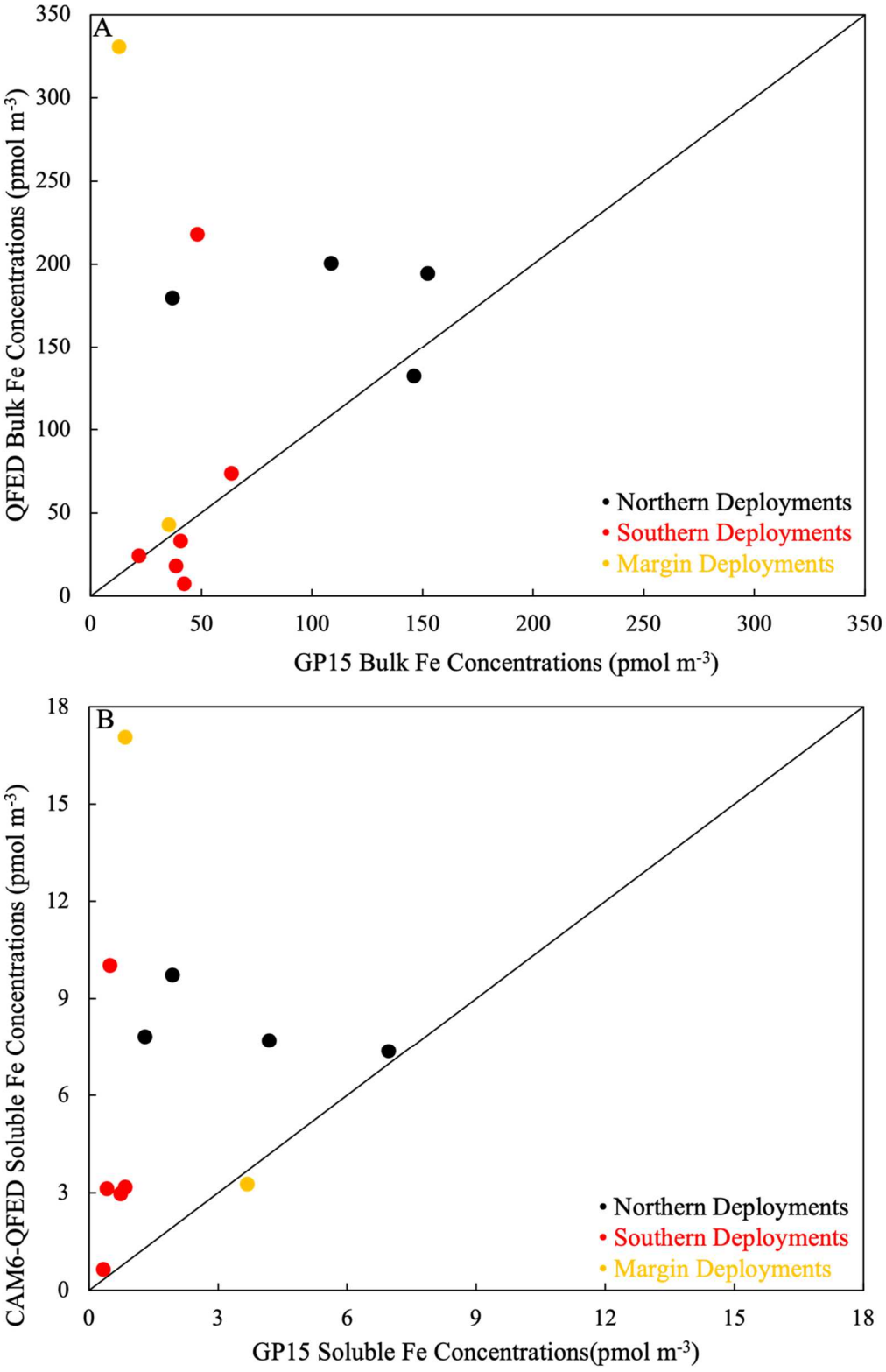

Figure 21. GP15 Aerosol Observation and CAM6-QFED Deposition Model Predicted Comparison. A) bulk and **B)** soluble concentrations.

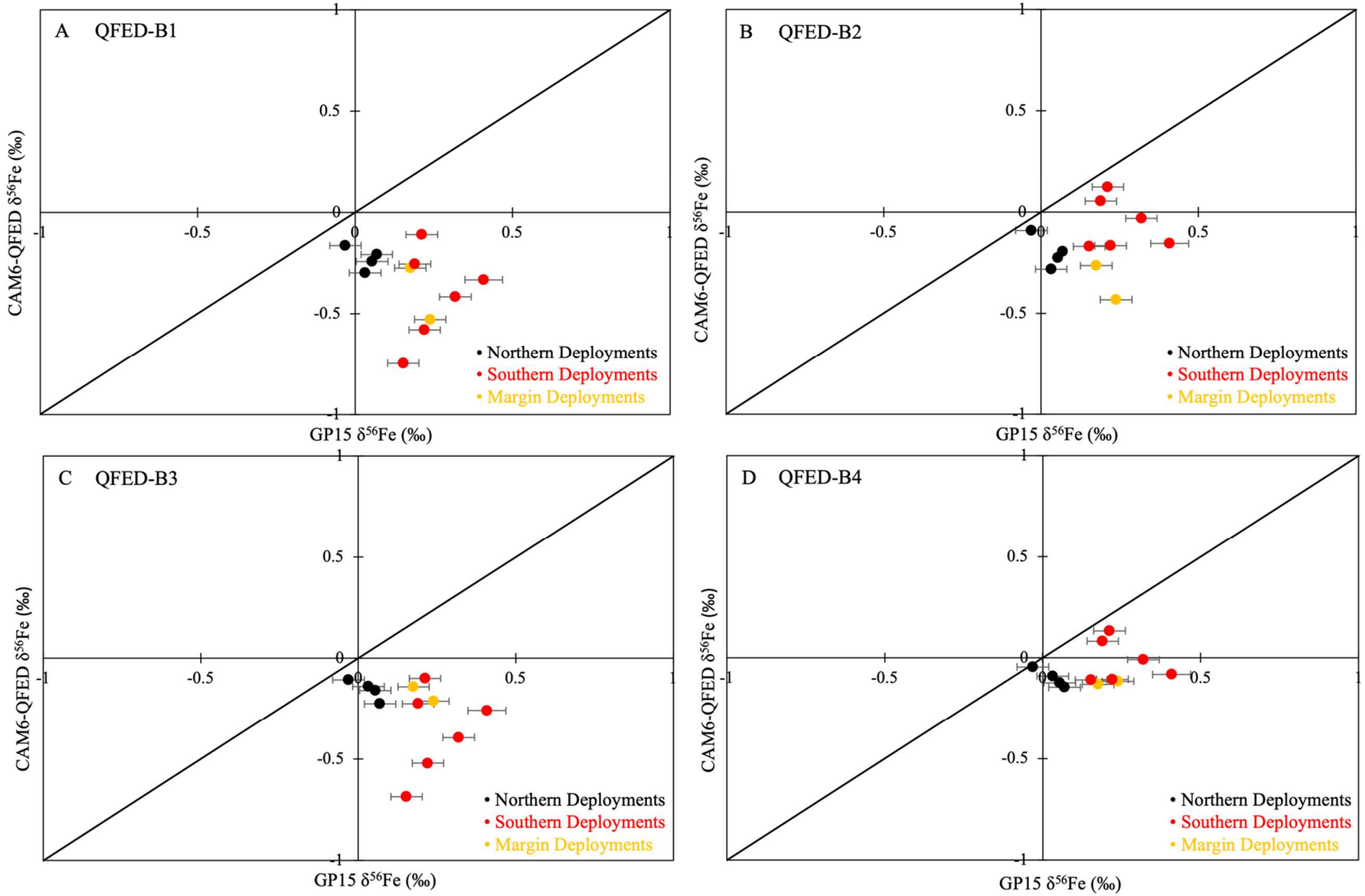

Figure 22. Comparisons of Bulk δ^{56}Fe from GP15 Aerosols and CAM6-QFEDB Output Scenarios. A) QFED-B1 B) QFED-B2 **C)** QFED-B3 **D)** QFED-B4.

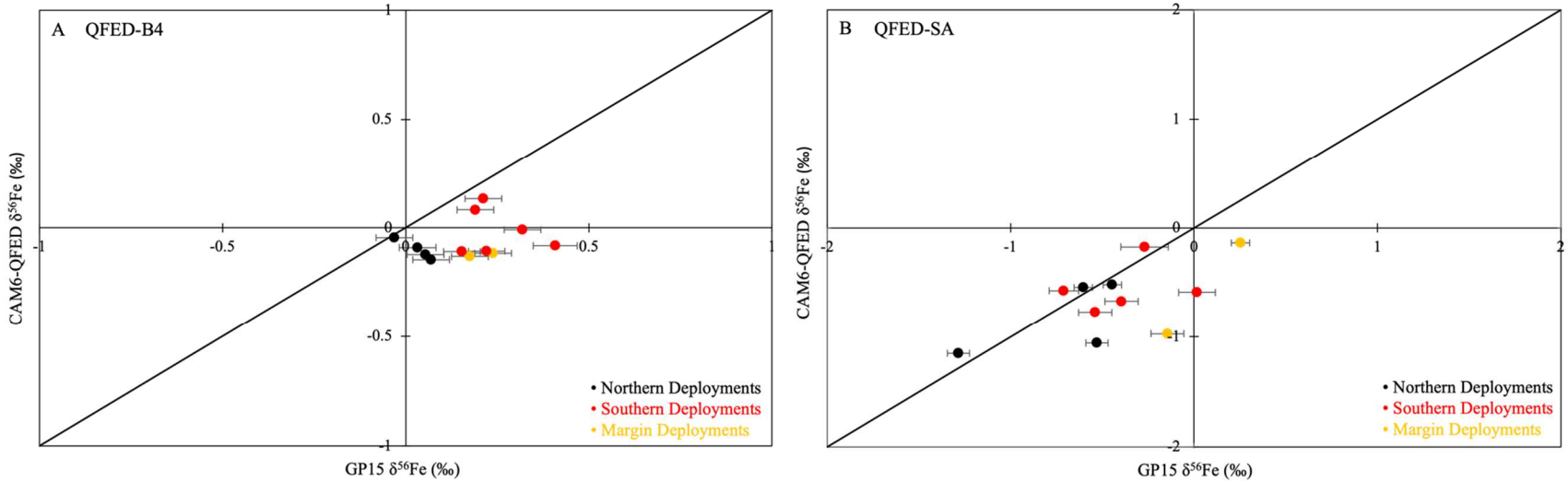

Figure 23. Optimal Bulk and Soluble δ^{56}Fe Endmember QFED and GP15 Comparison. A) QFED-B4 and **B)** QFED-SA.

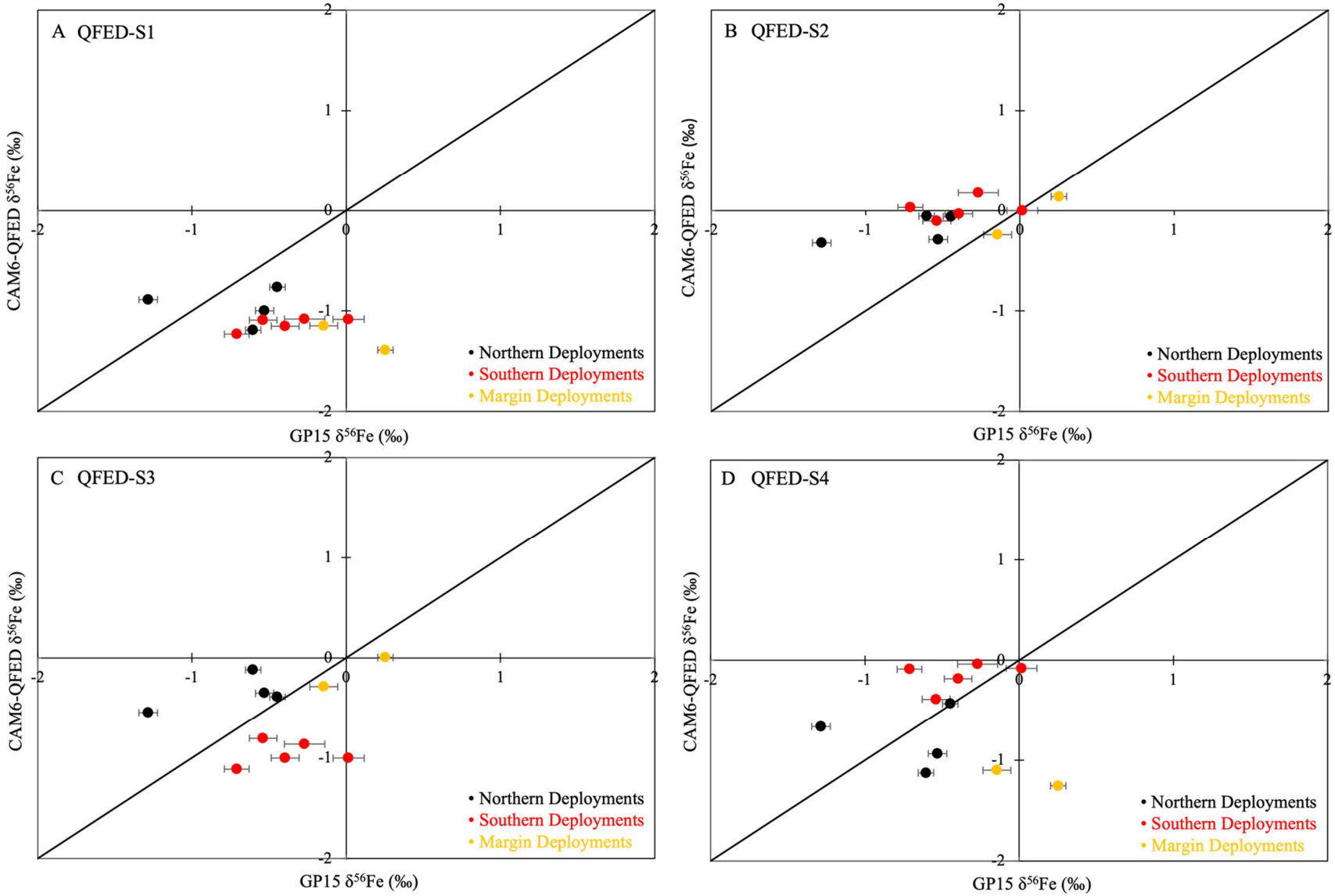

Figure 24. Comparisons of Soluble δ^{56}Fe from GP15 Aerosols and CAM6-QFEDS Output Scenarios. A) QFED-S1 **B)** QFED-S2 **C)** QFED-S3 **D)** QFED-S4.

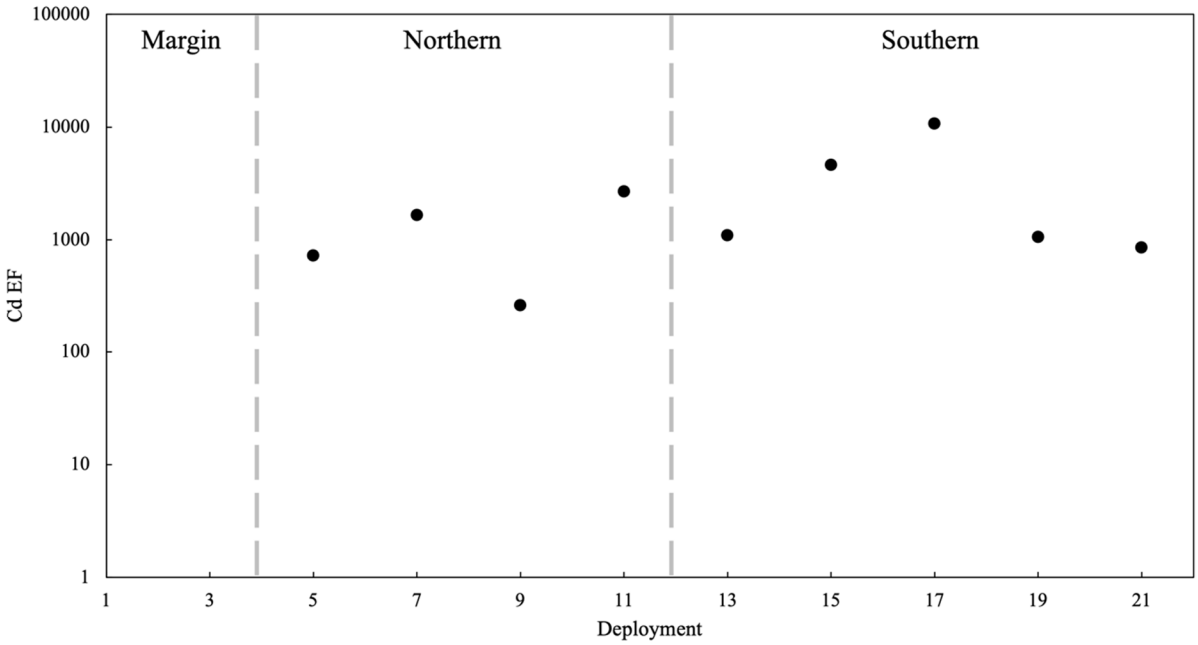

Figure 25. GP15 Cd Enrichment Factors. Note the log scale.

Table 8. Northern Bulk Deployment Two-Component Mixing. Proportion of each source (dust and anthropogenic activity) to bulk GP15 deployments based on endmembers from Conway *et al.* (2019), Beard *et al.* (2003), Gong *et al.*, (2016). Endmembers: Natural (+0.09‰) and Anthropogenic (-1.6 and -4.3‰).

Deployment	% Natural Fe	% Anthropogenic Fe
5	93-97	3-7
7	97-99	1-3
9	98-99	1-2
11	99-99.5	0.5-1

Table 9. Northern Soluble Deployment Two-Component Mixing. Proportion of each source (dust and anthropogenic activity) to soluble GP15 deployments based on endmembers from Beard *et al.* (2003), Gong *et al.*, (2016) Conway *et al.* (2019), and Kurisu *et al.* (2021). Endmembers: Natural (+0.09‰) and Anthropogenic (-1.6 and -4.3‰).

Deployment	% Natural Fe	% Anthropogenic Fe
5	68-88	12-32
7	59-84	16-41
9	63-86	14-37
11	19-69	31-81

Table 10. QFED Simulation Bulk Endmembers. QFED-B1 endmembers derived from Conway *et al.*, (2019). QFED-B2 endmembers derived from Conway *et al.* (2019) and Kurisu and Takahashi (2019). QFED-B3 endmembers derived from Conway *et al.* (2019) and Kurisu *et al.* (2016). QFED-B4 endmembers derived from Conway *et al.*, (2019), Kurisu *et al.* (2016), and Kurisu and Takahashi (2019).

δ^{56}Fe Endmembers	QFED-B1	QFED-B2	QFED-B3	QFED-B4	QFED-B5
Dust	+0.09‰	+0.09‰	+0.09‰	+0.09‰	+0.09‰
Fire	-1.60‰	+0.70‰	-1.60‰	+0.70‰	+2.00‰
Anthropogenic	-1.60‰	-1.60‰	-1.60‰	-1.60‰	-1.60‰
Shipping	-1.60‰	-1.60‰	+0.35‰	+0.35‰	+2.50‰

Table 11. QFED Simulation Soluble Endmembers. QFED-1 endmembers derived from Conway *et al.*, (2019). QFED-B2 endmembers derived from Conway *et al.* (2019) and Kurisu and Takahashi (2019). QFED-B3 endmembers derived from Conway *et al.* (2019) and Kurisu *et al.* (2016). QFED-B4 endmembers derived from Conway *et al.*, (2019), Kurisu *et al.* (2016), and Kurisu and Takahashi (2019).

δ^{56}Fe Endmembers	QFED-S1	QFED-S2	QFED-S3	QFED-S4	QFED-SA
Dust	+0.09‰	+0.09‰	+0.09‰	+0.09‰	+0.09‰
Fire	-1.60‰	+0.70‰	+0.70‰	-1.60‰	+0.70‰
Anthropogenic	-1.60‰	-1.60‰	-1.60‰	-1.60‰	-4.30‰
Shipping	-1.60‰	+0.35‰	-1.60‰	+0.35‰	+0.35‰

Table 12. QFED-1, 2, 3, and 4 Sum of the Squares of Misfits (SSM).

Simulation	Bulk SSM	Soluble SSM
QFED-1	3.9	7.5
QFED-2	1.6	2.5
QFED-3	2.9	2.9
QFED-4	0.9	4.5
QFED-5/A	0.2	1.1

CHAPTER FIVE:

CONCLUSIONS AND FUTURE WORK

5.2 Conclusions

GP15 aerosol trace metals are sourced from a mixture of natural dust and anthropogenic aerosols from East Asia and natural dust, wildfire aerosols, and anthropogenic aerosols from the coast of North America, with Asian dust dominating the northern deployments and a mix of sources dominating the southern deployments (Fig. 26).

Fe. Northern and southern aerosol deployments display stark contrasts between bulk and size-fractionated δ^{56}Fe as well as other parameters (i.e., concentrations, solubility, and enrichment factors) due the different and distinct mix of sources supplying Fe to them. While northern deployments bulk δ^{56}Fe are crustal, an isotopically light fine fraction and elevated V and Ni EFs indicate the influence of anthropogenic activities on Asian dust. In contrast, isotopically heavy bulk δ^{56}Fe of the southern deployments paired with the EFs of soil (Mn and Al) and biomass (Zn and Ni) tracers indicate that natural, wildfire, and anthropogenic Fe from North America are sources of Fe to the bulk. However, both northern and southern soluble δ^{56}Fe are similar and significantly lighter than crustal Fe revealing that anthropogenic Fe is a significant component of soluble Fe throughout North Pacific aerosols. Indeed, a two-component mixing model for northern deployments shows that up to 81% of soluble Fe could is anthropogenic but less than 7% of bulk Fe. However, a two-component model is unable to capture southern deployments as they receive Fe from at least three sources. Furthermore, refining the CAM6-QFED wildfire and shipping δ^{56}Fe endmembers verifies the heavy sources are wildfire and shipping Fe to the North Pacific. Lastly, the influence of aerosol Fe on surface waters may be evident at the corresponding northern deployments/stations where soluble aerosols are isotopically light while surface waters are the lightest of

the transect. In general aerosol $\delta^{56}Fe$ are not simply reflected in the dissolved phase in seawater, precluding the use of this tracer for calculation of aerosol input directly.

Zn. Like Fe, bulk and soluble $\delta^{66}Zn$ also show a dichotomy between northern and southern deployment Zn sources: both bulk and soluble $\delta^{66}Zn$ are light but generally become lighter southwards. While Zn at northern deployments is dominated by Asian dust (natural and anthropogenic), we suggest that southern deployments additionally contain dust, wildfire (soil, plant) and anthropogenic Zn from North America. The similarity between (and little variability within) the average isotopic composition of bulk and soluble GP15 aerosols (-0.11 ± 0.11‰ and --0.17 ± 0.15‰) suggests that we can establish a robust estimate of the isotopic signature of Zn to the North Pacific. However, as soluble aerosol Zn deposition is an order of magnitude less than soluble aerosol Fe, dissolved Zn in North Pacific surface waters are maintained at similar concentrations as Fe, and the impact of aerosol Zn is not observed in the surface of the North Pacific. While soluble aerosol Zn supply is deposited to the surface of the North Pacific, any dissolved $\delta^{66}Zn$ signature is modified by surface processes and upwelling Zn so that aerosol $\delta^{66}Zn$ is not discernible in the surface.

Cd. Soluble $\delta^{114}Cd$ are light throughout GP15 and Cd EFs are elevated but show no relationships with TM EFs. The light isotope compositions in combination with the absence of correlations with EFs are indicative of a consistent and dominant supply of anthropogenic Cd to North Pacific aerosols. While various TM EFs show distinctions between the northern and southern deployments as a result of different sources, Cd EFs are elevated along the entire transect. Cd concentrations from GP15 are similar to a previous Cd aerosol concentration study in the North Pacific during the high dust season and highlight the possibility of an anthropogenic Cd source to the North Pacific that is constant throughout the year and far more dominant than natural Cd.

5.2 Future Work

Fe. While Fe sources can be attributed to the northern and southern deployments, the supply of additional and isotopically unconstrained sources from Alaska, such as glacial flour or volcanism,

complicates the interpretation of which sources are supplying Fe to the margin deployments and more generally to the wider near-shore region. Although model comparison with GP15 δ^{56}Fe data shows the importance of heavy Fe from wildfire and shipping in the North Pacific, the bulk δ^{56}Fe fit remains lighter than observations. This is a consequence of bulk anthropogenic Fe being overestimated in the model, and perhaps refining the model could further improve the fit. The model also predicts wildfire Fe to have solubilities from 11 to 73%, but recent work has found bulk and soluble wildfire Fe to have solubilities lower than that (Hamilton *et al.*, 2019), and thus may not be as important in the soluble phase as for the bulk. As such, further work can be done to adjust solubility of wildfire-derived Fe and identify how this influences the fit between model and observations.

Zn and Cd. While recent studies have investigated the range of δ^{56}Fe of wildfires and the partitioning between soil and biomass, little to no work has been done to characterize δ^{66}Zn from wildfires or the ratio of soil to biomass Zn. Having a constraint on wildfire δ^{66}Zn along with relationships with EFs could potentially provide a good constraint to differentiate wildfire Zn from anthropogenic Zn. For Cd, while there are several studies identifying δ^{114}Cd produced from various anthropogenic processes, work on atmospheric Cd aerosols remains very limited. However, based on GP15 data, δ^{114}Cd can be used as a tracer of anthropogenic Cd in atmospheric aerosols, and therefore, further work can and should be done to constrain the range of anthropogenic Cd in atmospheric aerosols around the globe to advance this tracer.

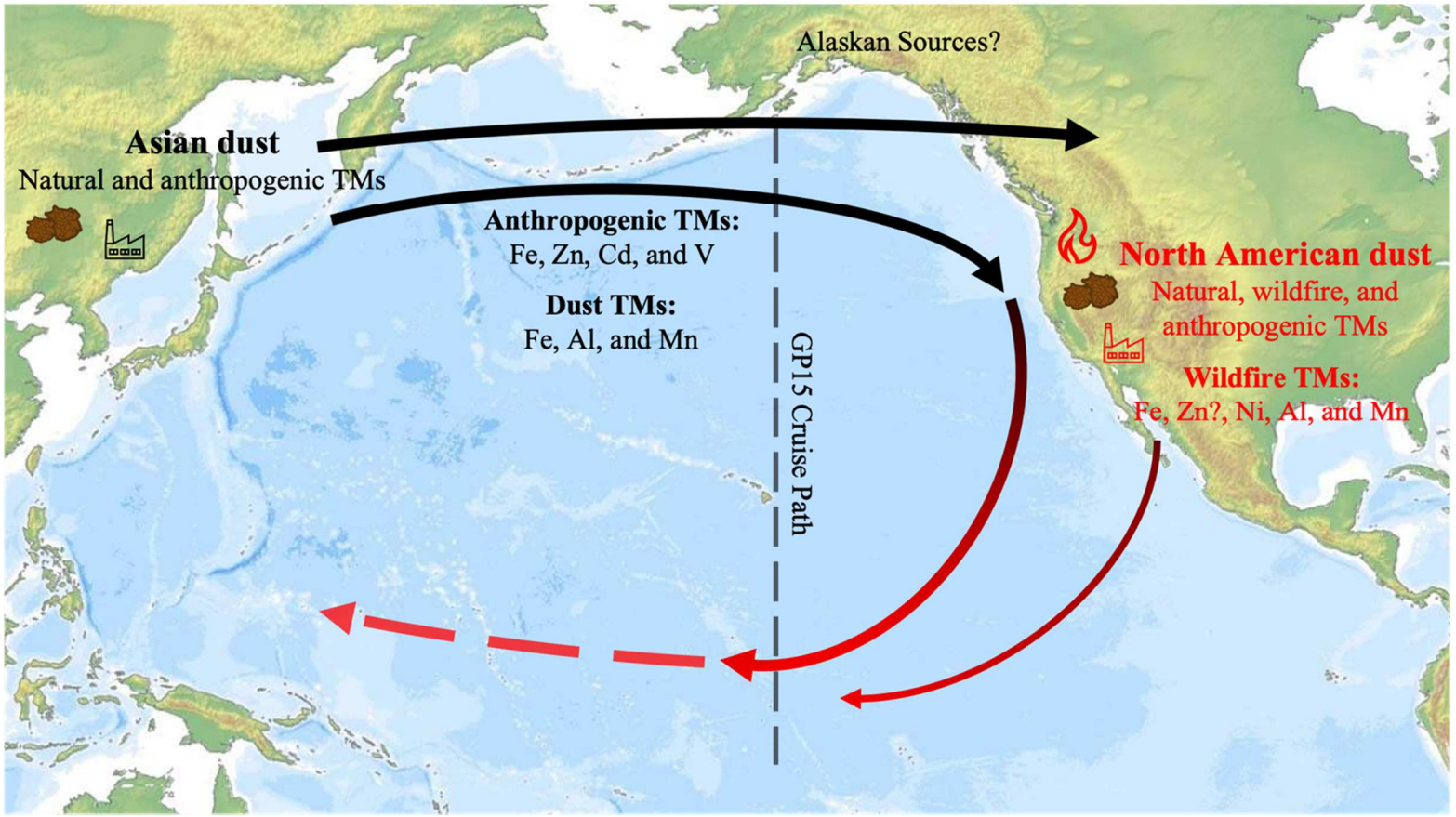

Figure 26. Idealized Schematic of North Pacific Low-dust Season Aerosol Sources based on GP15. (map modified from https://www.freeworldmaps.net/ocean/pacific/, and general circulation derived from Martin *et al*., 2002).

REFERENCES

Abouchami, W., Galer, S., de Baar, H., Middag, R., Vance, D., Zhao, Y., Klunder, M., Mezger, K., Feldmann, H., Andreae, M. (2014). Biogeochemical cycling of cadmium isotopes in the Southern Ocean along the Zero Meridian. *Geochimica et Cosmochimica Acta 127*, 348-367.

Abouchami, W., Galer, S., Horner, T., Rehkamper, M., Wombacher, F., Xue, Z., Lambelet, M., Gault-Ringold, M., Stirling, C., Schonbachler, M., Shiel, A., Weiz, D., Holdship, P. (2013). A common reference material for cadmium isotope studies–NIST SRM 3108. *Geostandards and Geoanalytical Research 37.1*, 5-17.

Achterberg, E., Holland, T., Bowie, A., Fauzi, R., Mantoura, C., Worsfold, P. (2001). Determination of iron in seawater. *Analytica Chimica Acta 442.1*, 1-14.

Akerman, A., Poitrasson, F., Oliva, P., Audry, S., Prunier, J., and Braun, J. J. (2014). The isotopic fingerprint of Fe cycling in an equatorial soil–plant–water system: the Nsimi watershed, South Cameroon. *Chemical Geology*, *385*, 104-116.

Al-Farawati, R., and van den Berg, C. (1999). Metal–sulfide complexation in seawater. *Marine Chemistry 63.3*, 331-352.

Andersen, M., Vance, D., Archer, C., Anderson, R., Ellwood, M., Allen, C., (2014). The Zn abundance and isotopic composition of diatom frustules, a proxy for Zn availability in ocean surface seawater. *Earth and Planetary Science Letters 301.1-2*, 137-145.

Anderson, R., Mawji, E., Cutter, G., Measures, C., Jeandel, C. (2014). GEOTRACES: changing the way we explore ocean chemistry. *Oceanography 27.1*, 50-61.

Andresen, E., Peiter, E., and Küpper, H. (2018). Trace metal metabolism in plants. *Journal of Experimental Botany*, *69*(5), 909-954.

Archer, C., and Vance, D. (2004). Mass discrimination correction in multiple-collector plasma source mass spectrometry: an example using Cu and Zn isotopes. *Journal of Analytical Atomic Spectrometry 19.5*, 656-665.

Archer, C., Andersen, M., Cloquet, C., Conway, T., Dong, S., Ellwood, M., Moore, R., Nelson, J., Rehkamper, M., Rouxel, O., Samanta, M., Shin. K., Sohrin, Y., Takano, S., Wasylenki, L. (2017). Inter-calibration of a proposed new primary reference standard AA-ETH Zn for zinc isotopic analysis. *Journal of Analytical Atomic Spectrometry 32.2*, 415-419.

Arrigo, Kevin R. (2005). Marine microorganisms and global nutrient cycles. *Nature 437.7057*, 349-355.

Baker, A., and Croot, P. (2010). Atmospheric and marine controls on aerosol iron solubility in seawater. *Marine Chemistry 120.1-4*, 4-13.

Baker, A., and Jickells, T. (2006). Mineral particle size as a control on aerosol iron solubility. *Geophysical Research Letters 33.17*.

Beard, B.,Johnson, C., Von Damm, K., Poulson, R. (2003). Iron isotope constraints on Fe cycling and mass balance in oxygenated Earth oceans. *Geology 31.7*, 629-632.

Bennett, S. Rouxel, O., Schmidt, K., Garbe-Shonberg, D., Statham, P., German, C. (2009). Iron isotope fractionation in a buoyant hydrothermal plume, 5 S Mid-Atlantic Ridge. *Geochimica et Cosmochimica Acta 73.19*, 5619-5634.

Bennett, S., Achterberg, E., Connelly, D., Statham, P., Fones, G., German, C. (2008). The distribution and stabilisation of dissolved Fe in deep-sea hydrothermal plumes. *Earth and Planetary Science Letters 270.3-4*, 157-167.

Bergquist, B. A., and Boyle. E. (2006). Iron isotopes in the Amazon River system: Weathering and transport signatures. *Earth and Planetary Science Letters 248.1-2*, 54-68.

Bermin, J., Vance D., Archer D., Statham P.J. (2006). The determination of the isotopic composition of Cu and Zn in seawater. *Chemical Geol*ogy *226*, 280-297.

Bodek, I., Lyman, W. J., Reehl, W. F., and D.H. Rosenblatt. (1988). Environmental Inorganic Chemistry: Properties, Processes, and Estimation Methods. *SETAC Special Publication Series, Pergamon Press. New York*.

Boyd, P., Jickells, T., Law. C., Blain, S., Boyle, E., Buesseler, K., Coale, K., Cullen, J., de Baar, H., Follows, M., Harvey, M., Lancelot, C., Levasseur, M., Owens, N., Pollard, R., Rivkin, R., Sarmiento, J., Schoemann, V., Smetacek, V., Takeda, S., Tsunda, A., Turner, A., Watson, A. (2007). Mesoscale iron enrichment experiments 1993-2005: synthesis and future directions. *Science 315.5812,* 612-617.

Boyd, Philip W., and Michael J. Ellwood. (2010). The biogeochemical cycle of iron in the ocean. *Nature Geoscience 3.10*, 675-682.

Boyle, E., and Edmond, J. (1977). Determination of copper, nickel, and cadmium in sea water by APDC chelate coprecipitation and flameless atomic absorption spectrometry. *Analytica Chimica Acta 91.2*, 189-197.

Boyle, E., John, S., Abouchami, W., Adkins, J., Echegoyen-Sanz, Y., Ellwood, M., Flegal, A, Fornace, K., Gallon, C., Galer, S., Gault-Ringold, M., Lacan, F., Radic, A., Rehkamper, M., Rouxel, O., Sohrin, Y., Stirling, C., Thompson, C., Vance, D., Xue, Z., Zhao, Y., (2012). GEOTRACES IC1 (BATS) contamination□prone trace element isotopes Cd, Fe, Pb, Zn, Cu, and Mo intercalibration. *Limnology and Oceanography: methods* 10.9 (2012): 653-665.

Boyle, E., Sclater, F., and Edmond, J. (1976). On the marine geochemistry of cadmium *Nature 263.5572*, 42-44.

Brand, L., Sunda, W., and Guillard, R. (1986). Reduction of marine phytoplankton reproduction rates by copper and cadmium. *Journal of experimental marine biology and ecology 96.3*, 225-250.

Breitbarth, E., Achterberg, E., Ardelan, M., Baker, A., Bucciarelli, E., Chever, F., Croot, P., Buggen, S., Gledhill, M., Hassellov, M., Hassler, C., Hoffmann, L., Hunter, K., Hutchins, D., Ingri, J., Jickells, T., Lohan, M., Nielsdottir, M., Sarthou, G., Schoemann, V., Trapp, J., Turner, D., Ye, Y. (2010). Iron biogeochemistry across marine systems–progress from the past decade. *Biogeosciences 7.3*, 1075-1097.

Bridgestock, L., Rehkamper, M., van de Flierdt, T., Murphy, K., Khondoker, R., Baker, A., Chance, R. (2017). Strekopytov, S., Humphreys-Williams, E., Achterberg, E., The Cd isotope composition of atmospheric aerosols from the Tropical Atlantic Ocean. *Geophysical Research Letters 44.6*, 2932-2940.

Brown, P. H., Welch, R. M., and Cary, E. E. (1987). Nickel: A micronutrient essential for higher plants. *Plant physiology*, *85(3)*, 801-803.

Bruland, K. (1980). Oceanographic distributions of cadmium, zinc, nickel, and copper in the North Pacific. *Earth and Planetary Science Letters 47.2*, 176-198.

Bruland, K., and Franks, R. (1983). Mn, Ni, Cu, Zn and Cd in the western North Atlantic. *Trace Metals in Sea water*, 395-414.

Bruland, K., Franks, R., Knauer, G., Martin, J. (1979). Sampling and analytical methods for the determination of copper, cadmium, zinc, and nickel at the nanogram per liter level in sea water. *Analytica Cosmochimica Acta 105*, 233-245.

Bruland, K., Knauer, G., and Martin, J. (1978). Zinc in north-east Pacific water. *Nature 271.5647*, 741-743.

Bruland, K., Knauer, G., and Martin, J. (1978). Cadmium in northeast Pacific waters 1. *Limnology and Oceanography 23.4*, 618-625.

Buck, C., Aguilar-Islas, A., Marsay, C., Kadko, D., Landing, W. (2019). Trace element concentrations, elemental ratios, and enrichment factors observed in aerosol samples collected during the US GEOTRACES eastern Pacific Ocean transect (GP16). *Chemical Geology 511*, 212-224.

Buck, C., Landing, W., and Resing, J. (2010). Particle size and aerosol iron solubility: A high-resolution analysis of Atlantic aerosols. *Marine Chemistry 120.1-4*, 14-24.

Buck, C., Landing, W., and Resing, J. (2013). Pacific Ocean aerosols: Deposition and solubility of iron, aluminum, and other trace elements. *Marine Chemistry 157*, 117-130.

Buck, C., Landing, W., Resing, J., Lebon, G. (2006). Aerosol iron and aluminum solubility in the northwest Pacific Ocean: Results from the 2002 IOC cruise. *Geochemistry, Geophysics, Geosystems 7.4*.

Byrne, R. H., and Kester, D. R. (1976). Solubility of hydrous ferric oxide and iron speciation in seawater. *Marine Chemistry*, *4*(3), 255-274.

Caldelas, C., and Weiss, D. J. (2017). Zinc homeostasis and isotopic fractionation in plants: a review. *Plant and Soil*, *411*(1), 17-46.

Cempel, M., & Nikel, G. J. P. J. S. (2006). Nickel: A review of its sources and environmental toxicology. *Polish Journal of Environmental Studies*, *15*(3).

Chapman, J., Mason, T., Weiss, D., Coles, B., Wilkinson, J. (2006). Chemical separation and isotopic variations of Cu and Zn from five geological reference materials. *Geostandards and Geoanalytical Research 30.1*, 5-16.

Cheng, K., Tian, H., Zhao, D., Lu, L., Wang, Y., Chen, J., Liu, X., Jia, W, Huang, Z. (2014). Atmospheric emission inventory of cadmium from anthropogenic sources. *International Journal of Environmental Science and Technology 11.3*, 605-616.

Chester, R., Murphy, K., Berry, L., Bradshaw, G., Corcoran, P. (1993) Factors controlling the solubilities of trace metals from non-remote aerosols deposited to the sea surface by the 'dry' deposition mode. *Marine Chemistry 42.2*. 107-126.

Chever, F., Rouxel, O., Croot, P., Panzevera, E., Wuttig, K., Auro, M. (2015). Total dissolvable and dissolved iron isotopes in the water column of the Peru upwelling regime. *Geochimica et Cosmochimica Acta 162*, 66-82.

Chuang, P., Duvall, R., Shafer, M., Schauer, J. (2005). The origin of water-soluble particulate iron in the Asian atmospheric outflow. *Geophysical Research Letters 32.7*.

Conway, T., and John, S. (2014). Quantification of dissolved iron sources to the North Atlantic Ocean. *Nature 511.7508*, 212-215.

Conway, T., and John, S. (2014). The biogeochemical cycling of zinc and zinc isotopes in the North Atlantic Ocean. *Global Biogeochemical Cycles 28.10*, 1111-1128.

Conway, T., and John, S. (2015) The cycling of iron, zinc and cadmium in the North East Pacific Ocean–Insights from stable isotopes. *Geochimica et Cosmochimica Acta 164*, 262-283.

Conway, T., and John, S. (2015). Biogeochemical cycling of cadmium isotopes along a high-resolution section through the North Atlantic Ocean. *Geochimica et Cosmochimica Acta 148*, 269-283.

Conway, T., Hamilton, D., Shelley, R., Aguilar-Islas, A., Landing, W., Mahowald, N., John, S. (2019). Tracing and constraining anthropogenic aerosol iron fluxes to the North Atlantic Ocean using iron isotopes. *Nature Communications 10.1*, 1-10.

Conway, T., Rosenberg, A., Adkins, J., John, S. (2013). A new method for precise determination of iron, zinc and cadmium stable isotope ratios in seawater by double-spike mass spectrometry. *Analytica Cosmochimica Acta 793*, 44-52.

Conway, T., Wolff, E., Rothlisberger, R., Mulvaney, R., Elderfield, H. (2015). Constraints on soluble aerosol iron flux to the Southern Ocean at the Last Glacial Maximum. *Nature Communications 6.1*, 1-9.

Crusius, J., Schroth, A., Gasso, S., Moy, C., Levy, R., Gatica, M. (2011). Glacial flour dust storms in the Gulf of Alaska: Hydrologic and meteorological controls and their importance as a source of bioavailable iron. *Geophysical Research Letters 38.6*.

Cullen, J. (2006). On the nonlinear relationship between dissolved cadmium and phosphate in the modern global ocean: could chronic iron limitation of phytoplankton growth cause the kink? *Limnology and oceanography 51.3*, 1369-1380.

de Baar, H., Boyd, P., Coale, K., Landry, M., Tsuda, A., Assmy, P., Bakker, D., Bozec, M., Barber, R., Brzezinski, M., Buesseler, K., Boye, M., Croot, P., Gervais, F., Gorbunov, M., Harrison, P., Hiscock, W., Laan, P., Lancelot, C., Law, C., Levasseur, M., Marchetti, A., Millero, F., Nishioka, J., Nojiri, Y., van Oijen, T., Riebessel, U., Rijkenberg, M., Saito, H., Takeda, S., Timmermans, K., Veldhuis, M., Waite, A., Wong, C. (2005). Synthesis of iron fertilization experiments: from the iron age in the age of enlightenment. *Journal of Geophysical Research: Oceans 110.C9*.

de Baar, H., de Jong, J., Bakker, D., Loscher, B., Smetacek, V. (1995). Importance of iron for plankton blooms and carbon dioxide drawdown in the Southern Ocean. *Nature 373.6513*, 412-415.

de Baar, H., Saager, P., Nolting, R., van der Meer, J. (1994). Cadmium versus phosphate in the world ocean. *Marine Chemistry 46.3*, 261-281.

Ding, Z. L., Yang, S. L., Sun, J. M., and Liu, T. S. (2001). Iron geochemistry of loess and red clay deposits in the Chinese Loess Plateau and implications for long-term Asian monsoon evolution in the last 7.0 Ma. *Earth and Planetary Science Letters*, *185*(1-2), 99-109.

Draxler, R., and Rolph, G. (2003). HYSPLIT (HYbrid Single-Particle Lagrangian Integrated Trajectory) model access via NOAA ARL READY website (http://www.arl.noaa.gov/ready/hysplit4. html). NOAA Air Resources Laboratory, Silver Spring. (2003).

Duce, R., and Tindale, N. (1991). Atmospheric transport of iron and its deposition in the ocean. *Limnology and Oceanography 36.8*. 1715-1726.

Duce, R., Liss, P., Merrill, J., Atlas, E., Buat-Menard, P., Hicks, B., Miller, J., Prospero, J., Arimoto, R., Church, T., Ellis, W., Galloway, J. (1991). The atmospheric input of trace species to the world ocean. *Global Biogeochemical Cycles 5.3*, 193-259.

Ellwood, M., Hutchins, D., Lohan, M., Milne, A., Nasemann, Nodder, S., Sander, S., Strzepek, R., Wilhelm, S., Boyd, P. (2015). Iron stable isotopes track pelagic iron cycling during a subtropical phytoplankton bloom. *Proceedings of the National Academy of Sciences 112.1*, E15-E20.

Ellwood, M., Strzepek, R., Strutton, P., Trull, T., Fourquez, M., Boyd, P. (2020). Distinct iron cycling in a Southern Ocean eddy. *Nature Communications 11.1*, 1-8.

Elrod, V., Berelson, W., Coale, K., Johnson, K. (2004). The flux of iron from continental shelf sediments: A missing source for global budgets. *Geophysical Research Letters 31.12*.

Emmanuel, S., Erel, Y., Matthews, A., & Teutsch, N. (2005). A preliminary mixing model for Fe isotopes in soils. *Chemical geology*, *222*(1-2), 23-34.

Fan, S., Moxim, W., and Levy H. (2006). Aeolian input of bioavailable iron to the ocean. *Geophysical Research Letters 33.7*.

Fantle, M. S., and DePaolo, D. J. (2004). Iron isotopic fractionation during continental weathering. *Earth and Planetary Science Letters*, *228*(3-4), 547-562.

Field, M., and Sherrell, R. (2000). Dissolved and particulate Fe in a hydrothermal plume at 9 45′ N, East Pacific Rise: Slow Fe (II) oxidation kinetics in Pacific plumes. *Geochimica et Cosmochimica Acta 64.4*, 619-628.

Fischer, E., Hsu, N., Jaffe, D., Jeong, M., Gong, S. (2009). A decade of dust: Asian dust and springtime aerosol load in the US Pacific Northwest. *Geophysical Research Letters 36.3*.

Fitzsimmons, J., Boyle, E., and Jenkins W. (2014). Distal transport of dissolved hydrothermal iron in the deep South Pacific Ocean. *Proceedings of the National Academy of Sciences 111.47*, 16654-16661.

Fitzsimmons, J., Conway, T., Lee, J., Kayser, R., Thyng, K., John, S., Boyle, E. (2016). Dissolved iron and iron isotopes in the southeastern Pacific Ocean. *Global Biogeochemical Cycles 30.10*, 1372-1395.

Fitzsimmons, J., John, S., Marsay, C., Hoffman, C., Nicholas, S., Toner, B., Germna, C., Sherrell, R. (2017). Iron persistence in a distal hydrothermal plume supported by dissolved–particulate exchange. *Nature Geoscience 10.3*, (195-201.

Froelich, P., Klinkhammer, G., Bender, M., Luedtke, N., Heath, G., Cullen, D., Dauphin, P., Hammond, D., Hartman, B., Maynard, V. (1979). Early oxidation of organic matter in pelagic sediments of the eastern equatorial Atlantic: suboxic diagenesis. *Geochimica et Cosmochimica Acta 43.7*, 1075-1090.

Fung, I., Meyn, S., Tegen, I., Doney, S., John, J., Bishop, J. (2000). Iron supply and demand in the upper ocean. *Global Biogeochemical Cycles 14.1*, 281-295.

Furutani, H., Meguro, A., Iguchi, H., and Uematsu, M. (2010). Geographical distribution and sources of phosphorus in atmospheric aerosol over the North Pacific Ocean. *Geophysical Research Letters 37*(3).

Geider, R., and Roche, J. (1994). The role of iron in phytoplankton photosynthesis, and the potential for iron-limitation of primary productivity in the sea. *Photosynthesis Research 39.3*, 275-301.

George, E., Stirling, C. H., Gault-Ringold, M., Ellwood, M. J., and Middag, R. (2019). Marine biogeochemical cycling of cadmium and cadmium isotopes in the extreme nutrient-depleted subtropical gyre of the South West Pacific Ocean. *Earth and Planetary Science Letters 514*, 84-95.

George, E., Stirling, C., Gault-Ringold, M., Ellwood, M., Middag, R. (2019). Marine biogeochemical cycling of cadmium and cadmium isotopes in the extreme nutrient-depleted subtropical gyre of the South West Pacific Ocean. *Earth and Planetary Science Letters 514*, 84-95.

German, C., Campbell, A., and Edmond, J. (1991). Hydrothermal scavenging at the Mid-Atlantic Ridge: modification of trace element dissolved fluxes. *Earth and Planetary Science Letters 107.1*, 101-114.

Ginoux, P., Chin, M., Teegen, I., Prospero, J., Holben, B., Dubovik, O., Lin, S. (2001). Sources and distributions of dust aerosols simulated with the GOCART model. *Journal of Geophysical Research: Atmospheres 106.D17*, 20255-20273.

Ginoux, P., Prospero, J. M., Gill, T. E., Hsu, N. C., and Zhao, M. (2012). Global□scale attribution of anthropogenic and natural dust sources and their emission rates based on MODIS Deep Blue aerosol products. *Reviews of Geophysics*, *50* (3).

Gioia, S., Weiss, D., Coles, B., Arnold, T., Babinski, M. (2008). Accurate and precise zinc isotope ratio measurements in urban aerosols. *Analytical Chemistry 80.24*, 9776-9780.

Glaccum, R., and Prospero, J. (1980). Saharan aerosols over the tropical North Atlantic—Mineralogy. *Marine Geology 37.3-4*, (295-321.

Gledhill, M., and van den Berg, C. (1994). Determination of complexation of iron (III) with natural organic complexing ligands in seawater using cathodic stripping voltammetry. *Marine Chemistry 47.1*, 41-54.

Gong Y, Xia Y, Huang F, Yu H. (2016) Average iron isotopic compositions of the upper continental crust: constrained by loess from the Chinese Loess Plateau. *Acta Geochimica,* 36(2), 125–131.

Graziano, L., Geider, R., Li, W., Olaizola, M. (1996). Nitrogen limitation of North Atlantic phytoplankton: Analysis of physiological condition in nutrient enrichment experiments. *Aquatic Microbiology Ecology 11*, 53–64.

Grousset, F. E., Quetel, C. R., Thomas, B., Donard, O. F. X., Lambert, C. E., Guillard, F., and Monaco, A. (1995). Anthropogenic vs. lithogenic origins of trace elements (As, Cd, Pb, Rb, Sb, Sc, Sn, Zn) in water column particles: northwestern Mediterranean Sea. *Marine Chemistry*, *48*(3-4), 291-310.

Guieu, C., Bonnet, S., Wagener, T., Loye-Pilot, M. (2005). Biomass burning as a source of dissolved iron to the open ocean?. *Geophysical Research Letters 32.19*.

Gurganus, Sarah C., Andrew S. Wozniak, and Patrick G. Hatcher. (2015). Molecular characteristics of the water soluble organic matter in size-fractionated aerosols collected over the North Atlantic Ocean. *Marine Chemistry 170*, 37-48.

Hamilton, D. S., Moore, J. K., Arneth, A., Bond, T. C., Carslaw, K. S., Hantson, S., Ito, A., Kaplan, J., Lindsay, K., Nieradzik, L., Rathod, S., Scanza, R., and Mahowald, N. M. (2020). Impact of changes to the atmospheric soluble iron deposition flux on ocean biogeochemical cycles in the Anthropocene. *Global Biogeochemical Cycles*, *34*(3).

Hamilton, D. S., Perron, M. M., Bond, T. C., Bowie, A. R., Buchholz, R. R., Guieu, C., Ito, A., Maenhaut, W., Myriokefalitakis, S., Olgun, N., Rathod, S., Schepanski, K., Tagliabue, A., Wagner, R., and Mahowald, N. M. (2022). Earth, wind, fire, and pollution: Aerosol nutrient sources and impacts on ocean biogeochemistry. *Annual Review of Marine Science*, *14*, 303-330.

Hamilton, D. S., Scanza, R. A., Rathod, S. D., Bond, T. C., Kok, J. F., Li, L., Matsui, H., and Mahowald, N. M. (2020). Recent (1980 to 2015) trends and variability in daily□to□interannual soluble iron deposition from dust, fire, and anthropogenic sources. *Geophysical Research Letters*, *47*(17).

Hamilton, D., Scanza, R., Feng, Y., Guinness, J., Kok, J., Li, L., Liu, X., Rathod, S., Wan, J., Wu, M., Mahowald, N. (2019). Improved methodologies for Earth system modelling of atmospheric soluble iron and observation comparisons using the Mechanism of Intermediate complexity for Modelling Iron (MIMI v1. 0). *Geoscientific Model Development 12.9*.

Hand, J., Mahowald, N., Chen, Y., Siefert, R., Luo, C., Subramaniam, A., Fung, I. (2004). Estimates of atmospheric□processed soluble iron from observations and a global mineral aerosol model: Biogeochemical implications. *Journal of Geophysical Research: Atmospheres 109.D17*.

Henkel, S., Kasten, S., Hartmann, J., Silva-Busso, A., Staubwasser, M. (2018). Iron cycling and stable Fe isotope fractionation in Antarctic shelf sediments, King George Island. *Geochimica et Cosmochimica Acta 237*, 320-338.

Homoky, W., John, S., Conway, T., Mills, R. (2013). Distinct iron isotopic signatures and supply from marine sediment dissolution. *Nature Communications 4.1*, 1-10.

Homoky, W., Severmann, S., Mills, R., Statham, P., Fones, G. (2009). Pore-fluid Fe isotopes reflect the extent of benthic Fe redox recycling: evidence from continental shelf and deep-sea sediments. *Geology 37.8*, 751-754.

Horner, T., Lee, R., Henderson, G., Rickaby, R. (2013). Nonspecific uptake and homeostasis drive the oceanic cadmium cycle. *Proceedings of the National Academy of Sciences 110.7*, 2500-2505.

Hsu, S. C., Lin, F. J., and Jeng, W. L. (2005). Seawater solubility of natural and anthropogenic metals within ambient aerosols collected from Taiwan coastal sites. *Atmospheric Environment*, *39*(22), 3989-4001.

Huang, K., Zhuang, G., Li, J., Wang, Q., Sun, Y., Lin, Y., and Fu, J. S. (2010). Mixing of Asian dust with pollution aerosol and the transformation of aerosol components during the dust storm over China in spring 2007. *Journal of Geophysical Research: Atmospheres*, *115*(D7).

Hudson, R., Covault, D., and Morel, F. (1992). Investigations of iron coordination and redox reactions in seawater using 59Fe radiometry and ion-pair solvent extraction of amphiphilic iron complexes. *Marine Chemistry 38.3-4*, 209-235.

Ito, A. (2013). Global modeling study of potentially bioavailable iron input from shipboard aerosol sources to the ocean. *Global Biogeochemical Cycles 27.1*, 1-10.

Ito, A., and Shi. Z. (2016). Delivery of anthropogenic bioavailable iron from mineral dust and combustion aerosols to the ocean. *Atmospheric Chemistry and Physics 16.1*, 85-99.

Ito, A., Myriokefalitakis, S., Kanakidou, M., Mahowald, N., Scanza, R., Hamilton, D., Baker, A., Jickells, T., Sarin, M., Bikkina, S., Gao, Y., Shelley, R., Buck, C., Landing, W., Bowie, A., Perron, M., Guieu, C., Meskhidze, N., Johnson, M., Feng, Y, Kok, J., Nenes, A., Duce, R. (2019). Pyrogenic iron: The missing link to high iron solubility in aerosols. *Science Advances 5.5*.

Janssen, D., Conway, T., John., S., Christian, J., Kramer, D., Pederson, T., Cullen, J. (2014). Undocumented water column sink for cadmium in open ocean oxygen-deficient zones. *Proceedings of the National Academy of Sciences 111.19*, 6888-6893.

Jeandel, C., Anderson, R., Henderson, G., Francois, R., Frank, M. (2006). GEOTRACES: An international program to study the global marine biogeochemistry of trace elements and isotopes. *No. IAEA-CSP--26/P*.

Jeandel, C., Peucker-Ehrenbribnk, B., Jones, M., Pearce, C., Oelkers, E., Godderis, Y., Lacan, F., Aumont, O., Arsouzie, T. (2011). Ocean margins: The missing term in oceanic element budgets? *Eos, Transactions American Geophysical Union 92.26*, 217-218.

Jickells, T. D., and Spokes, L. J. (2001) Atmospheric iron inputs to the oceans. *The Biogeochemistry of Iron in Seawater*, 85-121.

Jickells, T., An, Z., Andersen, K., Baker, A., Bergametti, G., Brooks, N., Cao, J., Boyd, P., Duce, R., Hunter, K., Kawahata, H., Kubilay, N., LaRoche, J., Liss, P., Mahowald, N., Prospero, J., Ridgwell, A., Tegen, I., Torres, R. (2005), Global iron connections between desert dust, ocean biogeochemistry, and climate. *Science 308.5718*, 67-71.

Jickells, T., Baker, A., and Chance, R., (2016). Atmospheric transport of trace elements and nutrients to the oceans. *Philosophical Transactions of the Royal Society A: Mathematical, Physical and Engineering Sciences 374.2081*, 20150286.

John, S. (2007). The marine biogeochemistry of zinc isotopes. *Woods Hole Oceanographic Institution, MA*.

John, S., Helgoe, J., and Townsend, E. (2018), Biogeochemical cycling of Zn and Cd and their stable isotopes in the Eastern Tropical South Pacific. *Marine Chemistry 201*, 256-262.

John, S., Mendez, J., Moffett, J., Adkins, J. (2012). The flux of iron and iron isotopes from San Pedro Basin sediments. *Geochimica et Cosmochimica Acta 93*, 14-29.

Johnson, C., Beard, B., and Weyer, S. (2020). Iron geochemistry: an isotopic perspective. *Springer*.

Journet, E., Desboeufs, K., Caquineuau, S., Colin, J. (2008). Mineralogy as a critical factor of dust iron solubility. *Geophysical Research Letters 35.7*.

Jouvin, D., Weiss, D. J., Mason, T. F. M., Bravin, M. N., Louvat, P., Zhao, F., Ferec, F., Hinsinger, P., and Benedetti, M. F. (2012). Stable isotopes of Cu and Zn in higher plants: evidence for Cu reduction at the root surface and two conceptual models for isotopic fractionation processes. *Environmental science and technology*, *46*(5), 2652-2660.

Kandler, K., and Scheuvens, D. (2019). Asian and Saharan dust from a chemical/mineralogical point of view: differences and similarities from bulk and single particle measurements. *E3S Web of Conferences*, *99*, 03001. EDP Sciences.

Klar, J., Homoky, W., Statham, P., Birchill, A., Harris, E., Woodward, E., Silburn, B., Cooper, M., James, R., Connelly, D., Chever, F., Lichtschlag, A., Graves, C. (2017). Stability of dissolved and soluble Fe (II) in shelf sediment pore waters and release to an oxic water column. *Biogeochemistry 135.1-2*, 49-67.

Klar, J., Schlosser, C., Milton, J., Woodward, E., Lacan, F., Parkinson, I., Achterberg, E., James, R. (2018). Sources of dissolved iron to oxygen minimum zone waters on the Senegalese continental margin in the tropical North Atlantic Ocean: Insights from iron isotopes. *Geochimica et Cosmochimica Acta 236*, 60-78.

Klunder, M., Laan, P., Middag, R., de Baar, H., Bakker, K. (2012). Dissolved iron in the Arctic Ocean: Important role of hydrothermal sources, shelf input and scavenging removal. *Journal of Geophysical Research: Oceans 117.C4*.

König, D., Conway, T. M., Ellwood, M. J., Homoky, W. B., and Tagliabue, A. (2021). Constraints on the cycling of iron isotopes from a global ocean model. *Global Biogeochemical Cycles*, *35*(9).

König, D., Conway, T., Hamilton, D., and Tagliabue, A. (2022). Surface ocean biogeochemistry regulates the impact of anthropogenic aerosol Fe deposition on iron and iron isotopes in the North Pacific. *Copernicus Meetings.*

Krishnamurthy, A., Moore, J., Mahowald, N., Luo, C., Doney, S., Lindsay, K., Zender, C. (2009). Impacts of increasing anthropogenic soluble iron and nitrogen deposition on ocean biogeochemistry. *Global Biogeochemical Cycles 23.3*.

Kubier, A., Wilkin, R. T., and Pichler, T. (2019). Cadmium in soils and groundwater: a review. *Applied Geochemistry*, *108*, 104388.

Kurisu, M., and Takahashi, Y., Testing iron stable isotope ratios as a signature of biomass burning. *Atmosphere* 10.2 (2019): 76.

Kurisu, M., Adachi, K., Sakata, K., and Takahashi, Y (2019). Stable isotope ratios of combustion iron produced by evaporation in a steel plant. *ACS Earth and Space Chemistry*, *3*, 588-598.

Kurisu, M., Sakata, K., Myamoto, C., Takaku, Y., Iizuke, T., Takahashi, Y. (2016). Variation of iron isotope ratios in anthropogenic materials emitted through combustion processes. *Chemistry Letters 45.8*, 970-972.

Kurisu, M., Sakata, K., Uematsu, M., Ito, A., and Takahashi, Y. (2021). Contribution of combustion Fe in marine aerosols over the northwestern Pacific estimated by Fe stable isotope ratios. *Atmospheric Chemistry and Physics*, *21*, 16027-16050.

Kurisu, M., Takahashi, Y., Iizuka, T., Uematsu, M. (2016). Very low isotope ratio of iron in fine aerosols related to its contribution to the surface ocean. *Journal of Geophysical Research: Atmospheres 121.18*, 11-119.

Labatut, M., Lacan, F., Pradoux, C., Chmeleff, J., Radic, A., Murray, J., Poitrasson, F., Johansen, A., Thil, F. (2014). Iron sources and dissolved□particulate interactions in the seawater of the Western Equatorial Pacific, iron isotope perspectives. *Global Biogeochemical Cycles 28.10*, 1044-1065.

Lacan, F., Francois, R., Yongcheng, J., Sherrell, R. (2006). Cadmium isotopic composition in the ocean. *Geochimica et Cosmochimica Acta 70.20*, 5104-5118.

Landing, W., and Bruland, K. (1987). The contrasting biogeochemistry of iron and manganese in the Pacific Ocean. *Geochimica et Cosmochimica Acta 51.1*, 29-43.

Lane, T., and Morel, F. (2000). A biological function for cadmium in marine diatoms. *Proceedings of the National Academy of Sciences 97.9*, 4627-4631.

Lemaitre, N., de Souza, G., Archer, C., Wang, R., Planquette, H., Sarthou, G., Vance, D. (2020). Pervasive sources of isotopically light zinc in the North Atlantic Ocean. *Earth and Planetary Science Letters 539*, 116216.

Liao, W. H., Takano, S., Tian, H. A., Chen, H. Y., Sohrin, Y., and Ho, T. Y. (2021). Zn elemental and isotopic features in sinking particles of the South China Sea: Implications for its sources and sinks. *Geochimica et Cosmochimica Acta*, *314*: 68-84.

Lindsay, W. L. (1972). Zinc in soils and plant nutrition. *Advances in agronomy 24*, 147-186.

Little, S., Vance, D., Walker-Brown, C., Landing, W. (2014). The oceanic mass balance of copper and zinc isotopes, investigated by analysis of their inputs, and outputs to ferromanganese oxide sediments. *Geochimica et Cosmochimica Acta 125*, 673-693.

Longnecker, N. E., and Robson, A. D. (1993). Distribution and transport of zinc in plants. *Zinc in Soils and Plants,* 79-91. *Springer, Dordrecht*.

Luo, C., Mahowald, N., Bond, T., Chuang, P., Artaxom P., Siefert, R., Chen, Y., Schauer, J. (2008). Combustion iron distribution and deposition. *Global Biogeochemical Cycles 22.1*.

Luo, C., Mahowald, N., Meskhidze, N., Chen, T., Siefert, R., Baker, A., Johansen, A. (2005). Estimation of iron solubility from observations and a global aerosol model. *Journal of Geophysical Research: Atmospheres 110.D23*.

Mahowald, N., Baker, A., Bergametti, G., Brook, N., Duce, R., Jickells, T., Kubilay, N., Prospero, J., Tegen, I. (2005). Atmospheric global dust cycle and iron inputs to the ocean. *Global biogeochemical cycles 19.4*.

Mahowald, N., Engelstaedter, S., Luo, C., Sealy, A., Artaxo, P., Benitez-Nelson, C., Bonnet, S., Chen, Y., Chuang, P., Cohen, D., Dulac, F., Herut, B., Johansen, A., Kubilay, N., Losno, R., Maenhaut, W., Paytan, A., Prospero, J., Shank, L., Siefert, R. (2008). Atmospheric iron deposition: global distribution, variability, and human perturbations. *Annual Review of Marine Science 1*, 245-278.

Maréchal, C., Nicolas, E., Douchet, C., Albarede, F. (2000). Abundance of zinc isotopes as a marine biogeochemical tracer. *Geochemistry, Geophysics, Geosystems 1.5*.

Marsay, C. M., Kadko, D., Landing, W. M., and Buck, C. S. (2022). Bulk aerosol trace element concentrations and deposition fluxes during the U.S. GEOTRACES GP15 Pacific Meridional Transect. *Global Biogeochemical Cycles 36*.

Marschner, H., and Römheld, V. (1994). Strategies of plants for acquisition of iron. *Plant and soil*, *165*(2), 261-274.

Martin, B. D., Fuelberg, H. E., Blake, N. J., Crawford, J. H., Logan, J. A., Blake, D. R., and Sachse, G. W. (2002). Long□range transport of Asian outflow to the equatorial Pacific. *Journal of Geophysical Research: Atmospheres*, *107*(D2), PEM-5.

Martin, J., and Fitzwater, S. (1988). Iron deficiency limits phytoplankton growth in the north-east Pacific subarctic. *Nature 331.6154*, 341-343.

Martin, J., Gordon, R., Fitzwater, S., Broenkow, W. (1989). VERTEX: phytoplankton/iron studies in the Gulf of Alaska. *Deep Sea Research Part A. Oceanographic Research Papers 36.5*, 649-680

Martin, J.., Fitzwater, S., and Gordon, R. (1990). Iron deficiency limits phytoplankton growth in Antarctic waters. *Global Biogeochemical Cycles 4.1*, 5-12.

Matsui, H., Mahowald, N., Moteki, N., Hamilton, D., Ohata, S., Yoshida, A., Loike, M., Scanza, R., Flanner, M. (2018). Anthropogenic combustion iron as a complex climate forcer. *Nature Communications 9.1*, 1-10.

Mawji, E., Schlitzer, R., Dodas, E.M., Abadie, C., Abouchami, W., Anderson, R.F., Baars, O., Bakker, K., Baskaran, M., Bates, N.R. and Bluhm, K. (2015). The GEOTRACES intermediate data product 2014. *Marine Chemistry*, (1-8).

Mead, C., Herckes, P., Majestic, B. (2013). Anbar, A., Source apportionment of aerosol iron in the marine environment using iron isotope analysis. *Geophysical Research Letters 40.21*, 5722-5727.

Middag, R., van Heuven, S. M., Bruland, K. W., and de Baar, H. J. (2018). The relationship between cadmium and phosphate in the Atlantic Ocean unravelled. *Earth and Planetary Science Letters 492*, 79-88.

Middag, R., van Heuven, S., Bruland, K., de Baar, H. (2018). The relationship between cadmium and phosphate in the Atlantic Ocean unravelled. *Earth and Planetary Science Letters 492*, 79-88.

Millero, F., Yao, W., and Aicher, J. (1995). The speciation of Fe (II) and Fe (III) in natural waters. *Marine Chemistry 50.1-4*, 21-39.

Moore, C., Mills, M., Arrigo, K., Berman-Frank, I., Bopp, L., Boyd, P., Galbraith, E., Geider, R., Guieu, C., Jaccard, S., Jickells, J., La Roche, J., Lenton, T., Mahowald, N., Maranon, E., Marinov, I., Moore, J., Nakatsuka, T., Oschlies, A., Saito, M., Thingstad, T., Tsunda, A., Ulloa, O. (2013). Processes and patterns of oceanic nutrient limitation. *Nature Geoscience 6.9*, 701-710.

Moore, J., and Braucher, O. (2008). Sedimentary and mineral dust sources of dissolved iron to the world ocean. *Biogeosciences 5(3)*, 631-656.

Moore, J., and Doney, S. (2007). Iron availability limits the ocean nitrogen inventory stabilizing feedbacks between marine denitrification and nitrogen fixation. *Global Biogeochemical Cycles 21.2*.

Moore, J., Doney, S., and Lindsay, K., Upper ocean ecosystem dynamics and iron cycling in a global three dimensional model. *Global Biogeochemical Cycles* 18.4 (2004).

Moore, J., Doney, S., Glover, D., Fung, I. (2001). Iron cycling and nutrient-limitation patterns in surface waters of the World Ocean. *Deep. Res. Part Ii-Topical Study Oceanography*. *49*, 463–507.

Morel, F., and Malcolm, E. (2004). The biogeochemistry of cadmium. *Metal Ions in Biological Systems: Volume 42: Metal Complexes in Tumor Diagnosis and as Anticancer Agents 184*.

Morel, F., and Price, N. (2004). The biogeochemical cycles of trace metals in the oceans. *Science 300.5621*, 944-947.

Morel, F., and Saito, M. (2014). Marine Bioinorganic Chemistry: The Role of Trace Metals in the Oceanic Cycles of Major Nutrients. *Treatise on Geochemistry*, *2*, 123-150.

Morel, F., Reinfelder, J., Roberts, S. (1994). Chamberlain, C., Lee, J., Yee, D., Zinc and carbon co-limitation of marine phytoplankton. *Nature 269.6483*, 740-742.

Morton, P., Landing, W., Hsu, S., Milne, A., Aguilar-Islas, A., Baker, A., Bowie, A., Buck, C., Gao, Y., Gichuki, S., Hastings, M., Hatta, M., Johansen, A., Losno, R., Mead, C., Patey, M., Swarr, G., Vandermark, A., Zamora, L. (2013). Methods for the sampling and analysis of marine aerosols: results from the 2008 GEOTRACES aerosol intercalibration experiment. *Limnology and Oceanography: Methods 11.2*, 62-78.

Nasemann, P., Gault-Ringold, M., Stirling, C., Koschinsky, A., Sander, S. (2018). Processes affecting the isotopic composition of dissolved iron in hydrothermal plumes: A case study from the Vanuatu back-arc. *Chemical Geology 476*, 70-84.

Nriagu, J., and Pacyna, J. (1988) Quantitative assessment of worldwide contamination of air, water and soils by trace metals. *Nature 333.6169*, 134-139.

Okin, G., Baker, A., Tegen, I., Mahowald, N., Dentener, F., Duce, R., Galloway, J., Hunter, K., Kanakidou, M., Kubilay, N., Prospero, J., Sarin, M., Surapipith, V., Uematsu, M., Zhu T. (2011). Impacts of atmospheric nutrient deposition on marine productivity: Roles of nitrogen, phosphorus, and iron. *Global Biogeochemical Cycles 25.2*.

Pacyna J, and Pacyna E. (2001). An assessment of global and regional emissions of trace metals to the atmosphere from anthropogenic sources worldwide Environmental Reviews, 9 (2001), pp. 269-298

Pacyna, J., Pacyna, E., and Aas, W. (2009). Changes of emissions and atmospheric deposition of mercury, lead, and cadmium. *Atmospheric environment 43.1*, 117-127.

Parekh, P., Follows, M., and Boyle, E. (2004). Modeling the global ocean iron cycle. *Global Biogeochemical Cycles 18.1*.

Paris, R., Desboeufs, K. V., Formenti, P., Nava, S., & Chou, C. (2010). Chemical characterisation of iron in dust and biomass burning aerosols during AMMA-SOP0/DABEX: implication for iron solubility. *Atmospheric Chemistry and Physics*, *10*(9), 4273-4282.

Patterson, T. L., and Duce, R. A. (1991). The cycle of atmospheric cadmium over the North Pacific Ocean. *Tellus B*, *43(1)*, 12-29.

Peers, G., and Price, N. (2006). Copper-containing plastocyanin used for electron transport by an oceanic diatom. *Nature 441.7091*, 341-344.

Perron, M. M., Meyerink, S., Corkill, M., Strzelec, M., Proemse, B. C., Gault-Ringold, M., Sanz-Rodriguez, E., Chase, Z., and Bowie, A. R. (2022). Trace elements and nutrients in wildfire plumes to the southeast of Australia. *Atmospheric Research*, *270*, 106084.

Pinedo-González, P., Hawco, N. J., Bundy, R. M., Armbrust, E. V., Follows, M. J., Cael, B. B., ... and John, S. G. (2020). Anthropogenic Asian aerosols provide Fe to the north Pacific Ocean. *Proceedings of the National Academy of Sciences*, *117*(45), 27862-27868.

Pinedo-González, P., Hawco, N., Bundy, R., Armbrust, E., Follows, M., Cael, B., White, A., Ferron, S., Karl, D., John, S. (2020). Anthropogenic Asian aerosols provide Fe to the North Pacific Ocean. *Proceedings of the National Academy of Sciences 117.45* 27862-27868.

Poitrasson, F. (2006) On the iron isotope homogeneity level of the continental crust. *Chemical Geology 235.1-2*, 195-200.

Poonkothai, M. V. B. S., & Vijayavathi, B. S. (2012). Nickel as an essential element and a toxicant. *International Journal of Environmental Sciences*, *1*(4), 285-288.

Price, N., and Morel, F. (1990). Cadmium and cobalt substitution for zinc in a marine diatom. *Nature 344.6267*, 658-660.

Radic, A., Lacan, F., and Murray, J. (2011). Iron isotopes in the seawater of the equatorial Pacific Ocean: New constraints for the oceanic iron cycle. *Earth and Planetary Science Letters 306.1-2*, 1-10.

Rathod, S., Hamilton, D., Mahowald, N., Klimont, Z., Corbett, J, Bond, T. (2020). A Mineralogy□Based Anthropogenic Combustion□Iron Emission Inventory. *Journal of Geophysical Research: Atmospheres 125.17*.

Redfield, A. (1934). On the proportions of organic derivatives in sea water and their relation to the composition of plankton. *Liverpool: University Press of Liverpool*.

Resing, J., Sedwick, P., German, C., Jenkins, W., Moffet, J., Sohst, B., Tagliabue, A. (2015). Basin-scale transport of hydrothermal dissolved metals across the South Pacific Ocean. *Nature 523.7559*, 200-203.

Ripperger, S., and Rehkämper, M. (2007). Precise determination of cadmium isotope fractionation in seawater by double spike MC-ICPMS. *Geochimica et Cosmochimica Acta 71.3* 631-642.

Ripperger, S., Rehkamper, M., Porcelli, D., Halliday, A. (2007). Cadmium isotope fractionation in seawater—A signature of biological activity. *Earth and Planetary Science Letters 261.3-4*, 670-684.

Rolph, G. (2003) Real-time Environmental Applications and Display System (READY), NOAA Air Resource Laboratory, Silver Spring, Md.

Rosenthal, Y., Lam, P., Boyle, E., Thomson, J. (1995). Authigenic cadmium enrichments in suboxic sediments: Precipitation and post depositional mobility. *Earth and Planetary Science Letters 132.1-4*, 99-111.

Rouxel, O., Shanks, W., Bach, W., Edwards, K. (2008). Integrated Fe-and S-isotope study of seafloor hydrothermal vents at East Pacific Rise 9–10 N. *Chemical Geology 252.3-4*, 214-227.

Rouxel, O., Toner, B., Germain, Y., Glazer, B. (2018). Geochemical and iron isotopic insights into hydrothermal iron oxyhydroxide deposit formation at Loihi Seamount. *Geochimica et Cosmochimica Acta 220*, 449-482.

Rouxel, O., Toner, B., Manganini, S., German, C. (2016). Geochemistry and iron isotope systematics of hydrothermal plume fall-out at East Pacific Rise 9 50′ N. *Chemical Geology 441*, 212-234.

Rue, E., and Bruland, K. (1995). Complexation of iron (III) by natural organic ligands in the Central North Pacific as determined by a new competitive ligand equilibration/adsorptive cathodic stripping voltammetric method. *Marine Chemistry 50.1-4*, 117-138.

Saito, M., Goepfert T., and Ritt, J. (2008). Some thoughts on the concept of colimitation: three definitions and the importance of bioavailability. *Limnology and Oceanography* 53.1, 276-290.

Saito, M., Noble, A., Tagliabue, A., Geopfert, T., Lamborg, C., Jenkins, W. (2013). Slow-spreading submarine ridges in the South Atlantic as a significant oceanic iron source. *Nature Geoscience 6.9*, 775-779.

Samanta, M., Ellwood, M., and Strzepek, R., Zinc isotope fractionation by Emiliania huxleyi cultured across a range of free zinc ion concentrations. *Limnology and Oceanography* 63.2 (2018): 660-671.

Samanta, M., Ellwood, M., Sinoir, M., Hassler, C. (2017). Dissolved zinc isotope cycling in the Tasman Sea, SW Pacific Ocean. *Marine Chemistry 192*, 1-12.

Sander, S., and Koschinsky, A. (2011). Metal flux from hydrothermal vents increased by organic complexation. *Nature Geoscience 4.3*, 145-150.

Scanza, R., Hamilton, D., Perez Garcia-Pando, C., Buck, C., Baker, A., Mahowald, N. (2018). Atmospheric processing of iron in mineral and combustion aerosols: Development of an intermediate-complexity mechanism suitable for Earth system models. *Atmospheric Chemistry and Physics 18.19*, 14175-14196.

Schlitzer, R., Anderson, R.F., Dodas, E.M., Lohan, M., Geibert, W., Tagliabue, A., Bowie, A., Jeandel, C., Maldonado, M.T., Landing, W.M. and Cockwell, D. (2018). The GEOTRACES intermediate data product 2017. *Chemical Geology 493*, 210-223.

Schmitt, A. D., Galer, S. J., and Abouchami, W. (2009). High-precision cadmium stable isotope measurements by double spike thermal ionisation mass spectrometry. *Journal of Analytical Atomic Spectrometry*, *24*(8), 1079-1088.

Schmitt, A., Galer, S., and Abouchami, W. (2009). Mass-dependent cadmium isotopic variations in nature with emphasis on the marine environment. *Earth and Planetary Science Letters 277.1-2*, 262-272.

Schroth, A., Crusius, J., Sholkovitz, E., Bostick, B. (2009). Iron solubility driven by speciation in dust sources to the ocean. *Nature Geoscience 2.5*, 337-340.

Sedwick, P., Church, T., Bowie, A., Marsay, C., Ussher, S., Achilles, K., Lethaby, P., Johnson, R., Sarin, M., McGillicuddy, J. (2005). Iron in the Sargasso Sea (Bermuda Atlantic Time□series Study region) during summer: Eolian imprint, spatiotemporal variability, and ecological implications. *Global Biogeochemical Cycles 19.4*.

Sedwick, P., Edwards., P., Mackey, D., Griffiths, F., Parslow, J. (1997). Iron and manganese in surface waters of the Australian subantarctic region. *Deep Sea Research Part I: Oceanographic Research Papers 44.7*, 1239-1253.

Sedwick, P., Sholkovitz, E., and Church, T. (2007). Impact of anthropogenic combustion emissions on the fractional solubility of aerosol iron: Evidence from the Sargasso Sea. *Geochemistry, Geophysics, Geosystems 8.10*.

Severmann, S., Johnson, C., Beard, B., McManus, J. (2004). The effect of plume processes on the Fe isotope composition of hydrothermally derived Fe in the deep ocean as inferred from the Rainbow vent site, Mid-Atlantic Ridge, 36 14′ N. *Earth and Planetary Science Letters 225.1-2*, 63-76.

Severmann, S., Johnson, C., Beard, B., McManus, J. (2006) The effect of early diagenesis on the Fe isotope compositions of porewaters and authigenic minerals in continental margin sediments. *Geochimica et Cosmochimica Acta 70.8*.

Severmann, S., McManus, J., Berelson, W., Hammond, D. (2010). The continental shelf benthic iron flux and its isotope composition. *Geochimica et Cosmochimica Acta 74.14*, 3984-4004.

Sharma, M., Polizzotto, M., and Anbar, A. (2001). Iron isotopes in hot springs along the Juan de Fuca Ridge. *Earth and Planetary Science Letters 194.1-2*, 39-51.

Shelley, R., Morton, P., and Landing, W., Elemental ratios and enrichment factors in aerosols from the US-GEOTRACES North Atlantic transects. *Deep Sea Research Part II: Topical Studies in Oceanography* 116 (2015): 262-272.

Sholkovitz, E., Sedwick, P., and Church, T. (2009). Influence of anthropogenic combustion emissions on the deposition of soluble aerosol iron to the ocean: Empirical estimates for island sites in the North Atlantic. *Geochimica et Cosmochimica Acta 73.14*, 3981-4003.

Sholkovitz, E., Sedwick, P., Church, T., Baker, A., Powell, C. (2012). Fractional solubility of aerosol iron: Synthesis of a global-scale data set. *Geochimica et Cosmochimica Acta 89*, 173-189.

Sieber, M. (2019). The role of the Southern Ocean in the global biogeochemical cycling of cadmium and zinc and their isotopes. *Diss. ETH Zurich*.

Sieber, M., Conway, T., de Souza, G., Hassler, C., Ellwood, M., Vance, D. (2020). Cycling of zinc and its isotopes across multiple zones of the Southern Ocean: Insights from the Antarctic Circumnavigation Expedition. *Geochimica et Cosmochimica Acta 268*, 310-324.

Sieber, M., Conway, T. M., de Souza, G. F., Hassler, C. S., Ellwood, M. J., & Vance, D. (2021). Isotopic fingerprinting of biogeochemical processes and iron sources in the iron-limited surface Southern Ocean. *Earth and Planetary Science Letters*, *567*, 116967.

Sieber, M., Conway, T., de Souza, G., Obata, H., Takano, S., Sohrin, Y., Vance, D. (2019). Physical and biogeochemical controls on the distribution of dissolved cadmium and its isotopes in the Southwest Pacific Ocean. *Chemical Geology 511*, 494-509.

Siebert, C., Nägler, T., and Kramers, J. (2001). Determination of molybdenum isotope fractionation by double□spike multicollector inductively coupled plasma mass spectrometry. *Geochemistry, Geophysics, Geosystems 2.7*.

Smolders, E., Versieren, L., Shuofei, D., Mattielli, N., Weiss, D., Petrov, I., and Degryse, F. (2013). Isotopic fractionation of Zn in tomato plants suggests the role of root exudates on Zn uptake. *Plant and soil*, *370*(1), 605-613.

Staubwasser, M., Schoenberg, R., von Blankenburg, F., Kruger, S., Pohl, C. (2013). Isotope fractionation between dissolved and suspended particulate Fe in the oxic and anoxic water column of the Baltic Sea. *Biogeosciences 10.1*, 233-245.

Stein, A., Draxler, R., Rolph, G., Stunder, B., Cohen, M., Ngan, F. (2015). NOAA's HYSPLIT atmospheric transport and dispersion modeling system. *Bulletin of the American Meteorological Society 96.12*, 2059-2077.

Summers, B. A. (2020). Investigating the isotope signatures of dissolved iron in the Southern Atlantic Ocean *University of South Florida.*

Sunda, W., and Huntsman, S. (1996). Antagonisms between cadmium and zinc toxicity and manganese limitation in a coastal diatom. *Limnology and Oceanography 41.3*, 373-387.

Tagliabue, A., Bopp, L., and Aumont, O. (2009). Evaluating the importance of atmospheric and sedimentary iron sources to Southern Ocean biogeochemistry. *Geophysical Research Letters 36.13*.

Tagliabue, A., Bowie, A., Boyd, P., Buck, K., Johnson, K., Saito, M. (2017). The integral role of iron in ocean biogeochemistry. *Nature 543.7643*, 51-59.

Thompson, A., Ruiz, J., Chadwick, O. A., Titus, M., & Chorover, J. (2007). Rayleigh fractionation of iron isotopes during pedogenesis along a climate sequence of Hawaiian basalt. *Chemical Geology*, *238*(1-2), 72-83.

Timperley, M. H., Brooks, R. R., & Peterson, P. J. (1973). The distribution of nickel, copper, zinc, and iron in tree leaves. *Journal of experimental botany*, *24*(5), 889-895.Toner, B., Fakra, S., Manganini, S., Santelli, C., Marcus, M., Moffet, J., Rouxel, O., German, C., Edwards, K. (2009). Preservation of iron (II) by carbon-rich matrices in a hydrothermal plume. *Nature Geoscience 2.3*, 197-201.

Trapp, J, Millero F., and Prospero, J. (2010) Trends in the solubility of iron in dust□dominated aerosols in the equatorial Atlantic trade winds: Importance of iron speciation and sources. *Geochemistry, Geophysics, Geosystems 11.3*.

Ussher, S., Achterberg, E., and Worsfold, P., (2004). Marine biogeochemistry of iron. *Environmental Chemistry 1.2*, 67-80.

van den Berg, C. (1995). Evidence for organic complexation of iron in seawater. *Marine Chemistry 50.1-4*, 139-157.

van Geen, A., McCorkle, D., and Klinkhammer, P. (1995) Sensitivity of the phosphate□cadmium□carbon isotope relation in the ocean to cadmium removal by suboxic sediments. *Paleoceanography 10.2*, 159-169.

Vance, D., de Souza, G., Zhao, Y., Cullen, J., Lohan, M. (2019). The relationship between zinc, its isotopes, and the major nutrients in the North-East Pacific. *Earth and Planetary Science Letters 525*, 115748.

Vance, D., Little, S., Archer, C., Cameron, V., Andersen, M., Rijkenberg, M., Lyons, T. (2016). The oceanic budgets of nickel and zinc isotopes: the importance of sulfidic environments as illustrated by the Black Sea. *Philosophical Transactions of the Royal Society A: Mathematical, Physical and Engineering Sciences* 374.2081.

Vance, D., Little, S., de Souza, G., Khatiwala, S., Lohan, M., Middag, R. (2017). Silicon and zinc biogeochemical cycles coupled through the Southern Ocean. *Nature Geoscience 10.3*, 202-206.

Von Damm, K., Edmond, J., Grant, B., Measures, C., Walden, B., Weiss, R. (1985) Chemistry of submarine hydrothermal solutions at 21° N, East Pacific Rise. *Geochimica et Cosmochimica Acta 49.11*. 2197-2220.

Waeles, M., Baker, A., Jickells, T., Hoogewerff, J. (2007). Global dust teleconnections: aerosol iron solubility and stable isotope composition. *Environmental Chemistry 4.4*, 233-237.

Wang, R., Archer, C., Bowie, A., Vance, D. (2019). Zinc and nickel isotopes in seawater from the Indian Sector of the Southern Ocean: the impact of natural iron fertilization versus Southern Ocean hydrography and biogeochemistry. *Chemical Geology 511*, 452-464.

Wang, Z., Mu, J., Yang, M., and Yu, X. (2020). Reexamining the Mechanisms of East Asian Summer Monsoon Changes in Response to Non–East Asian Anthropogenic Aerosol Forcing. *Journal of Climate*, *33*(8), 2929-2944.

Weber, T., John, S., Tagliabue, A., DeVries, T. (2018). Biological uptake and reversible scavenging of zinc in the global ocean. *Science 361.6397*, 72-76.

Weiss, D. J., Rausch, N., Mason, T. F., Coles, B. J., Wilkinson, J. J., Ukonmaanaho, L., Arnold, T., and Nieminen, T. M. (2007). Atmospheric deposition and isotope biogeochemistry of zinc in ombrotrophic peat. *Geochimica et Cosmochimica Acta*, *71*(14), 3498-3517.

Wiederhold, J. G., Teutsch, N., Kraemer, S. M., Halliday, A. N., & Kretzschmar, R. (2007). Iron isotope fractionation in oxic soils by mineral weathering and podzolization. *Geochimica et Cosmochimica Acta*, *71*(23), 5821-5833.

Winton, V. H. L. (2016). Impact of biomass burning emissions and dust on soluble iron deposition to Australian waters, the Southern Ocean and Antarctica (Doctoral dissertation, Curtin University).

Wombacher, F., Rehkämper, M., Mezger, K., Bischoff, A., and Münker, C. (2008). Cadmium stable isotope cosmochemistry. *Geochimica et Cosmochimica Acta*, *72*(2), 646-667.

Wu, J., and Luther III, G. (1995). Complexation of Fe (III) by natural organic ligands in the Northwest Atlantic Ocean by a competitive ligand equilibration method and a kinetic approach. *Marine Chemistry 50.1-4*, 159-177.

Wu, J., Boyle, E., Sunda, W., Wen, L. (2013). Soluble and colloidal iron in the oligotrophic North Atlantic and North Pacific. *Science 293.5531*, 847-849.

Xue, Z., Rehkamper, M., Horner, T., Abouchami, W., Middag, R., van de Flierd, T., de Baar, H. (2013). Cadmium isotope variations in the Southern Ocean. *Earth and Planetary Science Letters 382*, 161-172.

Yang, S., Lee, D., Ho, T, Wen, L., Yang, H. (2014). The isotopic composition of dissolved cadmium in the water column of the West Philippine Sea. *Frontiers in Marine Science 1*, 61.

Yücel, M., Gartman, A., Chan, C., Luther III, G. (2011). Hydrothermal vents as a kinetically stable source of iron-sulphide-bearing nanoparticles to the ocean. *Nature Geoscience 4.6* 367-371.

Zender, C., Bian, H., and Newman, D. (2003). Mineral Dust Entrainment and Deposition (DEAD) model: Description and 1990s dust climatology. *Journal of Geophysical Research: Atmospheres 108.D14*.

Zhao, Y., Vance, D., Abouchami, W., de Baar, H. (2014). Biogeochemical cycling of zinc and its isotopes in the Southern Ocean. *Geochimica et Cosmochimica Acta 125*, 653-672.

APPENDIX A: SUPPLEMENTAL FIGURES AND TABLES

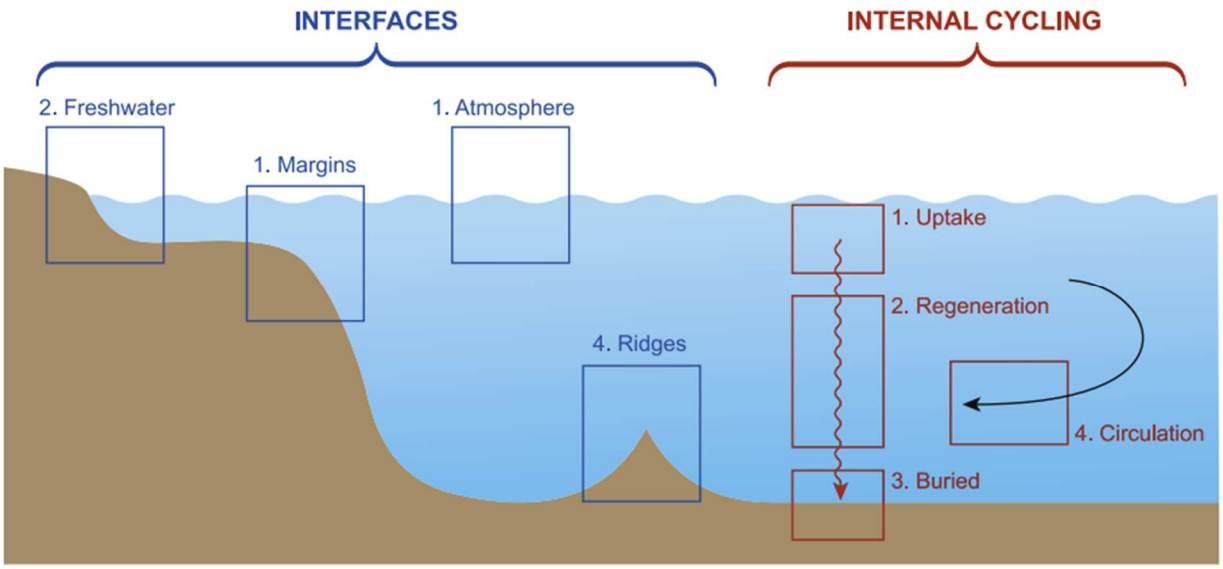

Figure A1. GEOTRACES Interfaces and Internal Cycling. GEOTRACES investigates the internal cycling of trace elements and their isotopes (TEIs) in the ocean (red boxes) and how TEIs are exchanged across various interfaces (blue boxes) (from Anderson *et al.*, 2014).

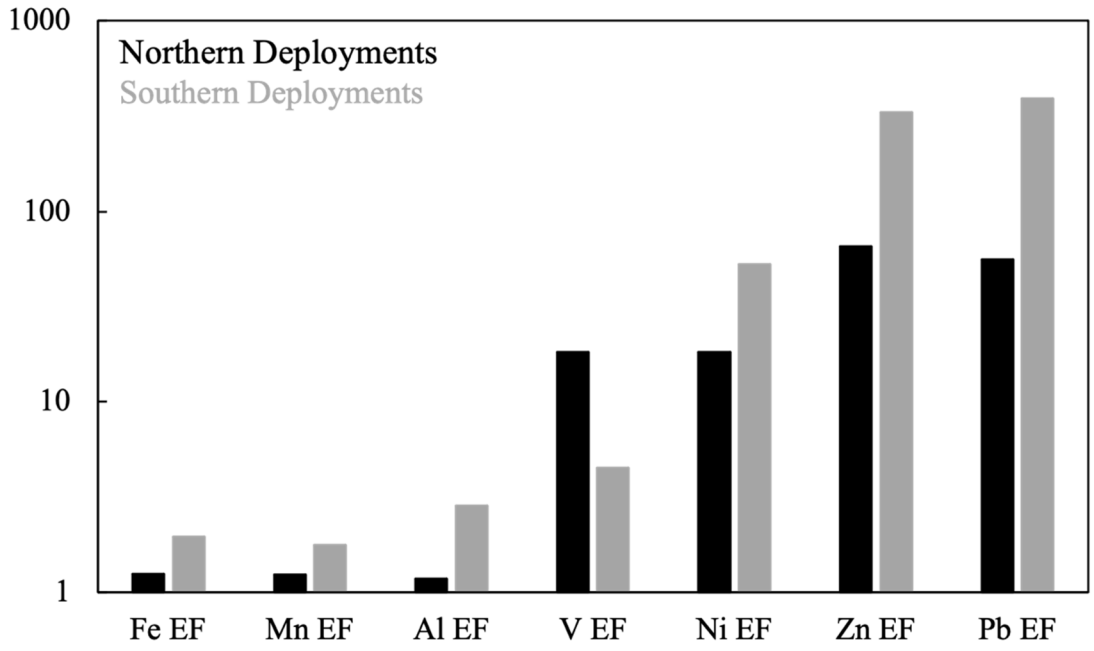

Figure A2. Average northern and southern Enrichment Factors. Northern deployments are black bars and southern deployments are gray. EFs are from Marsay *et al.* 2022.

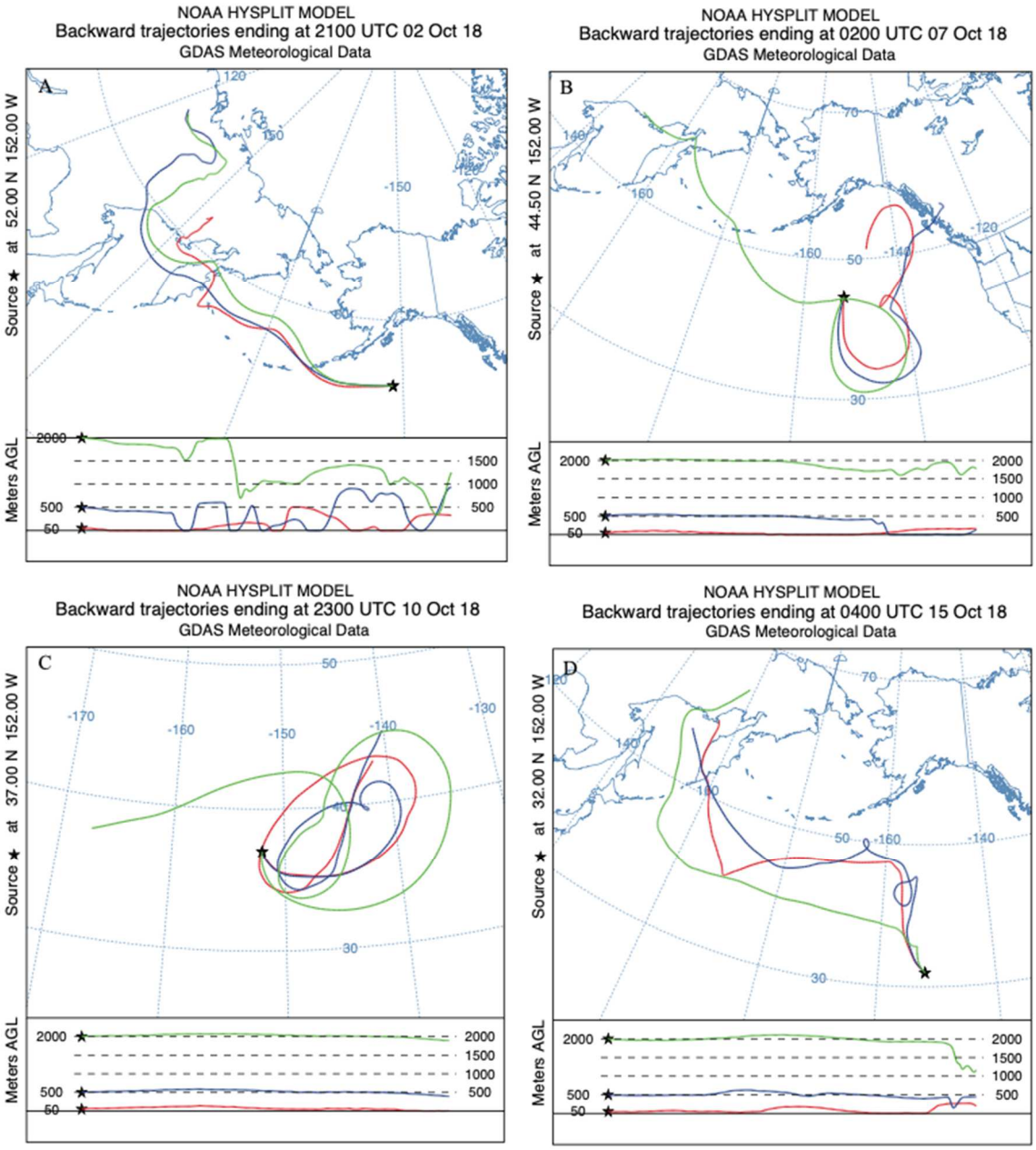

Figure A3. Northern Deployment HYSPLITs. Northern deployments are influenced by air masses that have either come from west or had been spinning over the open ocean. **A)** Deployment 5 **B)** Deployment 7 **C)** Deployment 9 and **D)** Deployment 11.

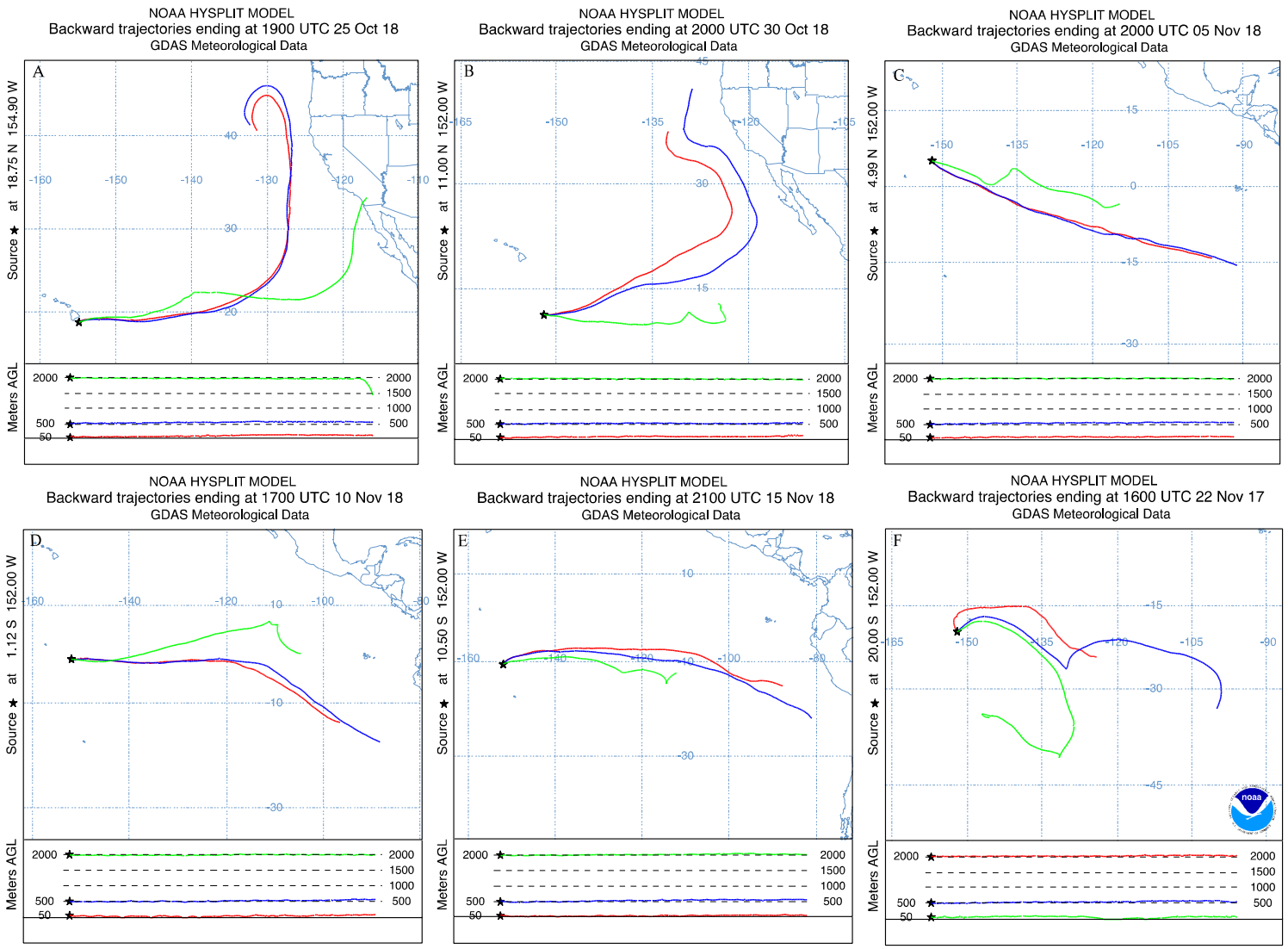

Figure A4. Southern Deployment HYSPLITs. Southern deployments are influenced by airmasses that have passed followed the North American coast or have come from the east. **A)** Deployment 13 **B)** Deployment 15 **C)** Deployment 17 and **D)** Deployment 19 **E)** Deployment 21 **F)** Deployment 23.

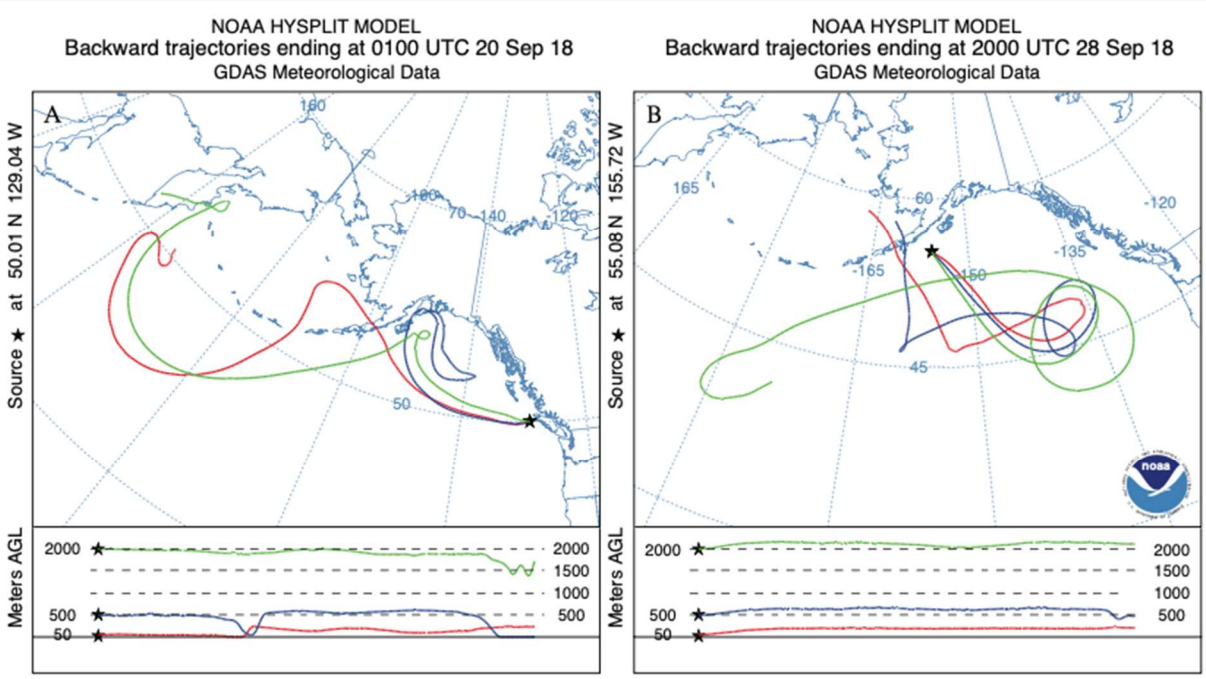

Figure A5. Margin Deployment HYSPLITs. Margin deployments are characterized by airmasses that had come from the west from the direction of Alaska. **A)** Deployment 1 **B)** Deployment 3.

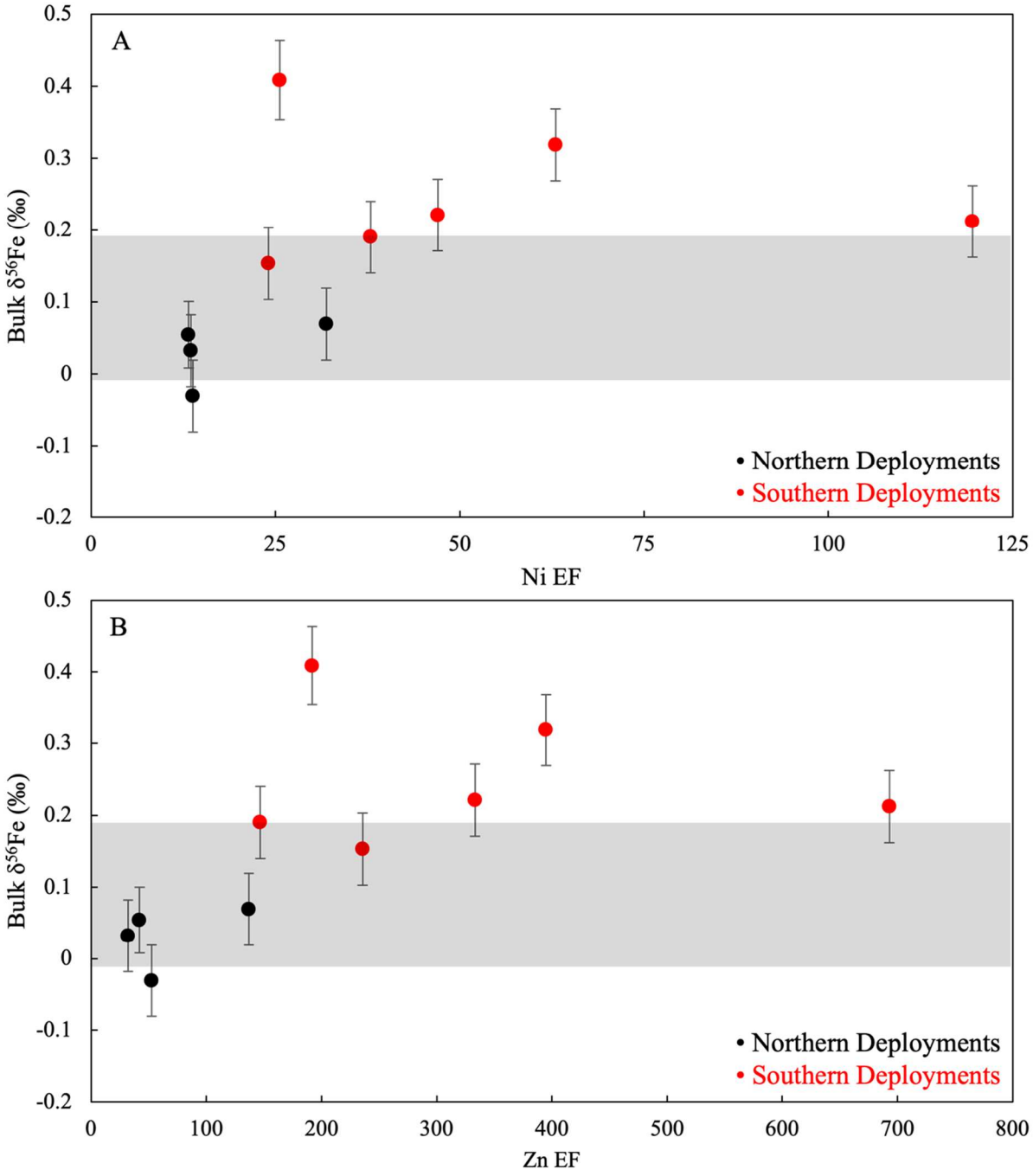

Figure A6. Bulk δ^{56}Fe Comparison with Zn and Ni Enrichment Factors. Northern (black circles) and southern (red circles) GP15 bulk δ^{56}Fe (‰) compared to **A)** Ni, **B)** Zn EFs. EFs are calculated using Eq. 2.

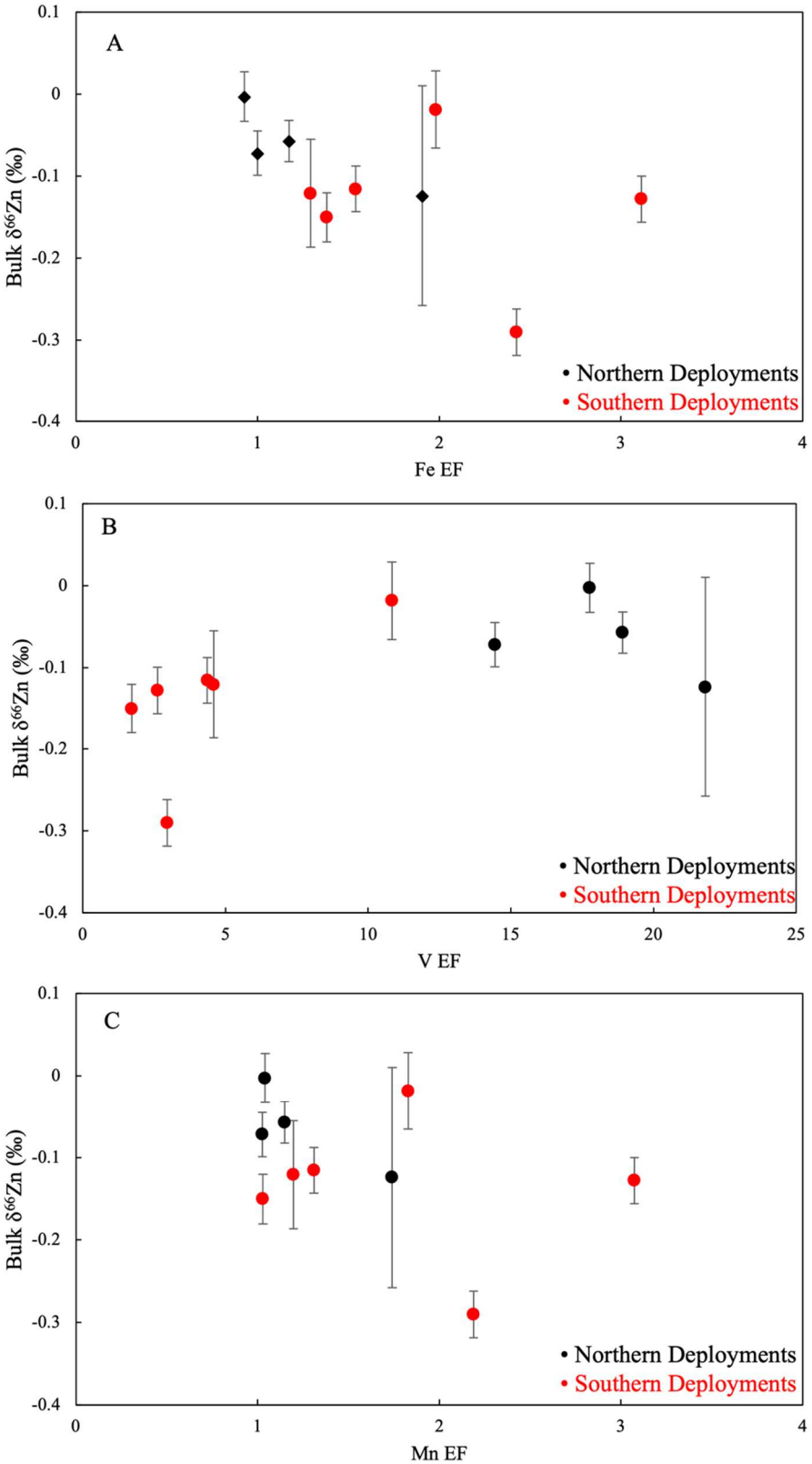

Figure A7. Bulk δ^{66}Zn Comparison with Fe, V, and Mn EFs. Northern (black circles) and southern (red circles) deployment's **A)** Fe EFs **B)** V EFs and **C)** Mn EFs compared to δ^{66}Zn. The range of crustal δ^{66}Zn is +0.27 to +0.34‰ (Little *et al.*, 2014). EFs are calculated using Eq. 2.

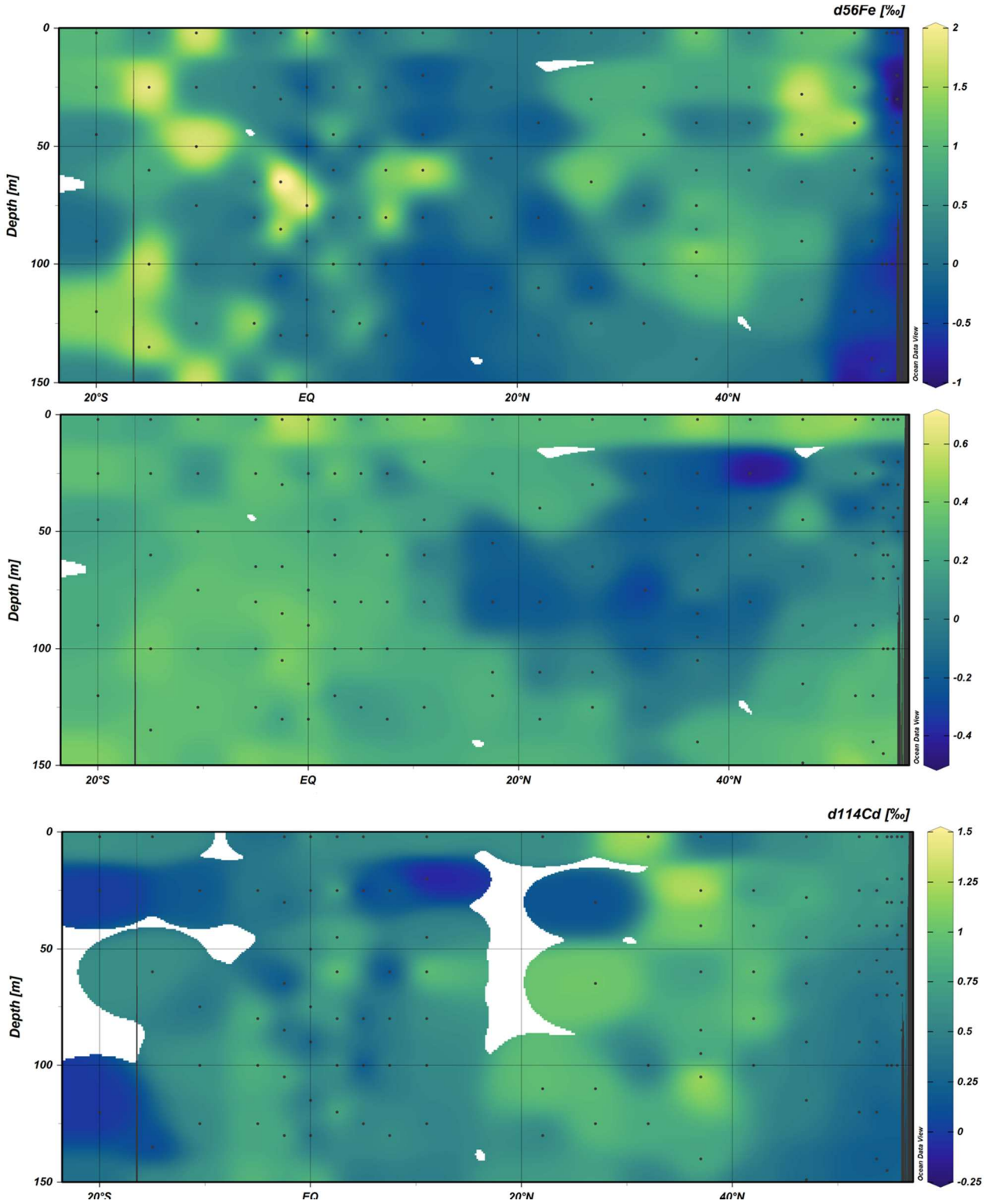

Figure A8. GP15 surface water (top 150 m. A) δ^{56}Fe **B)** δ^{66}Zn **C)** δ^{114}Cd. Reproduced from Sieber (pers. comm) and Sieber *et al*., (in review).

Table A1. Faraday Cup Configuration for Fe, Zn, and Cd using Thermo Neptune MC-ICPMS. Abundances are shown in brackets. Isobaric interferences shown below element/isotope. Major polyatomic interferences for Fe: ArO^+, ArN, $ArOH^+$; Zn: Ba^{2+}, ArN_2, $ArSi^+$; and Cd: MoO^+.

Cones and intro system	Faraday cup	**L4**	**L3**	**L2**	**L1**	**C**	**H1**	**H2**	**H3**	**H4**
Fe (HR) *Jet and X Apex Omega*	*Isotope*		^{52}Cr (83.8%)		^{54}Fe (5.85%)	^{56}Fe (91.8%)	^{57}Fe (2.12%)	^{58}Fe (0.28%)		^{60}Ni (26.2%)
	Isobaric Int.				^{54}Cr (2.37%)			^{58}Ni (68.1%)		
Zn (LR) *H and H Apex Omega*	*Isotope*			^{62}Ni (3.63%)	^{63}Cu (69.2%)	^{64}Zn (49.1%)	^{65}Cu (30.1%)	^{66}Zn (27.7%)	^{67}Zn (4.0%)	^{68}Zn (18.5%)
	Isobaric Int.					^{64}Ni (0.93%)				
Cd (LR) *Jet and H Apex Q*	*Isotope*		^{111}Cd (12.8%)	^{112}Cd (24.1%)	^{113}Cd (12.2%)	^{114}Cd (28.7%)	^{115}In (95.7%)	^{116}Cd (7.49%)	^{117}Sn (7.68%)	^{118}Sn (24.2%)
	Isobaric Int.			^{112}Sn (0.97%)	^{113}In (4.29%)	^{114}Sn (0.66%)	^{115}Sn (0.34%)	^{116}Sn (14.5%)		

Table A2. GP15 Aerosol Deployment Locations.

Deployment Type	Aerosol Deployment	Start Date	Latitude (°N)	Longitude (°W)	End Date	Latitude (°N)	Longitude (°W)	Air Volume (m^3)
Margin	1	9/21/18	50.01	129.04	9/21/18	52.10	125.29	120.9
	3	9/28/18	55.08	155.72	9/30/18	54.66	155.17	170.1
Northern	5	10/2/18	52.00	152.00	10/4/18	47.00	152.00	280.8
	7	10/7/18	44.50	152.00	10/9/18	42.00	152.00	189.0
	9	10/10/18	37.00	152.00	10/12/18	34.50	152.00	229.1
	11	10/15/18	32.00	152.00	10/17/18	37.00	152.00	256.9
Southern	13	10/25/18	18.75	154.90	10/28/18	17.50	152.00	178.0
	15	10/30/18	11.00	152.00	11/3/18	6.59	152.00	244.4
	17	11/5/18	4.99	152.00	11/8/18	1.91	152.00	270.4
	19	11/10/18	-1.12	152.00	11/13/18	-5.00	152.00	238.1
	21	11/15/18	-10.50	152.00	11/19/18	-15.00	152.00	264.4
	23	11/22/18	-20.00	152.00	11/23/18	-19.20	151.24	153.1

APPENDIX B: PERMISSIONS

This Agreement between University of South Florida -- Zach Bunnell ("You") and John Wiley and Sons ("John Wiley and Sons") consists of your license details and the terms and conditions provided by John Wiley and Sons and Copyright Clearance Center.

License Number	5312661361451
License date	May 19, 2022
Licensed Content Publisher	John Wiley and Sons
Licensed Content Publication	Journal of Geophysical Research: Atmospheres
Licensed Content Title	Long□range transport of Asian outflow to the equatorial Pacific
Licensed Content Author	Glen W. Sachse, Donald R. Blake, Jennifer A. Logan, et al
Licensed Content Date	Dec 5, 2002
Licensed Content Volume	107
Licensed Content Issue	D2
Licensed Content Pages	18
Type of use	Dissertation/Thesis
Requestor type	University/Academic
Format	Electronic
Portion	Figure/table
Number of figures/tables	1
Will you be translating?	No
Title	Tracing Anthropogenic Iron, Zinc, and Cadmium Aerosols Delivered to the Surface of the North Pacific Ocean
Institution name	University of South Florida
Expected presentation date	Jun 2022

Copyright information for Figure 4 modified from "Long-range transport of Asian outflow to the equatorial Pacific" by Martin *et al.* (2002). Journal of Geophysical Research: Atmospheres, 107(D2), PEM-5.

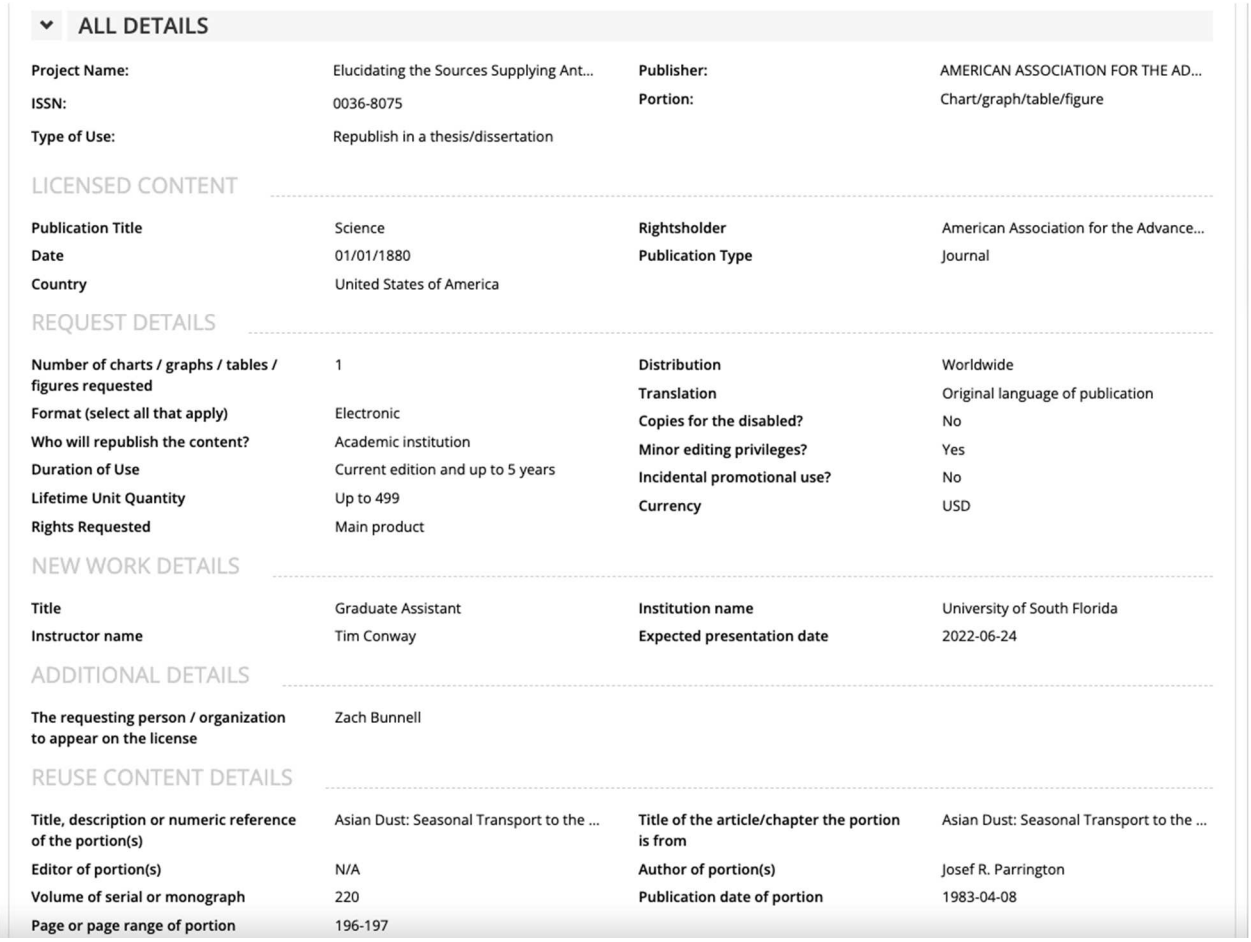

ALL DETAILS

Project Name:	Elucidating the Sources Supplying Ant...	**Publisher:**	AMERICAN ASSOCIATION FOR THE AD...
ISSN:	0036-8075	**Portion:**	Chart/graph/table/figure
Type of Use:	Republish in a thesis/dissertation		

LICENSED CONTENT

Publication Title	Science	**Rightsholder**	American Association for the Advance...
Date	01/01/1880	**Publication Type**	Journal
Country	United States of America		

REQUEST DETAILS

Number of charts / graphs / tables / figures requested	1	**Distribution**	Worldwide
		Translation	Original language of publication
Format (select all that apply)	Electronic	**Copies for the disabled?**	No
Who will republish the content?	Academic institution	**Minor editing privileges?**	Yes
Duration of Use	Current edition and up to 5 years	**Incidental promotional use?**	No
Lifetime Unit Quantity	Up to 499	**Currency**	USD
Rights Requested	Main product		

NEW WORK DETAILS

Title	Graduate Assistant	**Institution name**	University of South Florida
Instructor name	Tim Conway	**Expected presentation date**	2022-06-24

ADDITIONAL DETAILS

The requesting person / organization to appear on the license	Zach Bunnell

REUSE CONTENT DETAILS

Title, description or numeric reference of the portion(s)	Asian Dust: Seasonal Transport to the ...	**Title of the article/chapter the portion is from**	Asian Dust: Seasonal Transport to the ...
Editor of portion(s)	N/A	**Author of portion(s)**	Josef R. Parrington
Volume of serial or monograph	220	**Publication date of portion**	1983-04-08
Page or page range of portion	196-197		

Copyright information for Figure 5 modified from "Asian Dust: Seasonal Transport to the Hawaiian Islands" by Parrington *et al.* (1983). Science, 220 (4593): 195-197.

Rights and permissions

Copyright information for Figure 6 modified from "Conway, Tim M., et al. "Tracing and constraining anthropogenic aerosol iron fluxes to the North Atlantic Ocean using iron isotopes." by Conway *et al.* (2019). Nature Communications, 10(1), 1-10.

This Agreement between University of South Florida -- Zach Bunnell ("You") and John Wiley and Sons ("John Wiley and Sons") consists of your license details and the terms and conditions provided by John Wiley and Sons and Copyright Clearance Center.

License Number	5312660954994
License date	May 19, 2022
Licensed Content Publisher	John Wiley and Sons
Licensed Content Publication	Global Biogeochemical Cycles
Licensed Content Title	Bulk Aerosol Trace Element Concentrations and Deposition Fluxes During the U.S. GEOTRACES GP15 Pacific Meridional Transect
Licensed Content Author	Chris M. Marsay, David Kadko, William M. Landing, et al
Licensed Content Date	Feb 1, 2022
Licensed Content Volume	36
Licensed Content Issue	2
Licensed Content Pages	21
Type of use	Dissertation/Thesis
Requestor type	University/Academic
Format	Electronic
Portion	Figure/table
Number of figures/tables	2
Will you be translating?	No
Title	Tracing Anthropogenic Iron, Zinc, and Cadmium Aerosols Delivered to the Surface of the North Pacific Ocean
Institution name	University of South Florida
Expected presentation date	Jun 2022

Copyright information for Figure 7 modified from "Bulk Aerosol Trace Element Concentrations and Deposition Fluxes During the U.S. GEOTRACES GP15 Pacific Meridional Transect." by Marsay et al. (2022). Global Biogeochemical Cycles, 36(2).

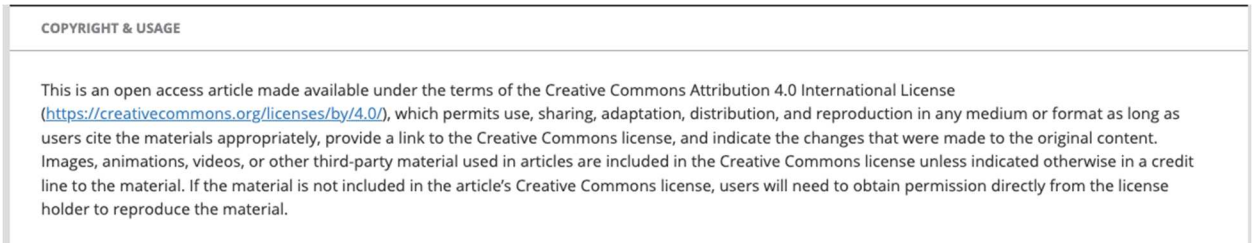

COPYRIGHT & USAGE

This is an open access article made available under the terms of the Creative Commons Attribution 4.0 International License (https://creativecommons.org/licenses/by/4.0/), which permits use, sharing, adaptation, distribution, and reproduction in any medium or format as long as users cite the materials appropriately, provide a link to the Creative Commons license, and indicate the changes that were made to the original content. Images, animations, videos, or other third-party material used in articles are included in the Creative Commons license unless indicated otherwise in a credit line to the material. If the material is not included in the article's Creative Commons license, users will need to obtain permission directly from the license holder to reproduce the material.

Copyright information for Figure A1 modified from "GEOTRACES: changing the way we explore ocean chemistry." by Andersen *et al.* (2014). Oceanography 27.1, 50-61.